DEPOSITION OF Cu-Zn-Sn-Se (CZTSe) THIN FILMS AND INVESTIGATION OF THEIR DEVICE PROPERTIES

A THESIS SUBMITTED TO
THE GRADUATE SCHOOL OF NATURAL AND APPLIED SCIENCES
OF
MIDDLE EAST TECHNICAL UNIVERSITY

BY

ÖZGE BAYRAKLI

IN PARTIAL FULFILLMENT OF THE REQUIREMENTS
FOR
THE DEGREE OF DOCTOR OF PHILOSOPHY
IN
PHYSICS

FEBRUARY 2018

Approval of the thesis:

DEPOSITION OF Cu-Zn-Sn-Se (CZTSe) THIN FILMS AND INVESTIGATION OF THEIR DEVICE PROPERTIES

submitted by **ÖZGE BAYRAKLI** in partial fulfillment of the requirements for the degree of **Doctor of Philosophy in Physics Department, Middle East Technical University** by,

Prof. Dr. Gülbin Dural Ünver
Dean, Graduate School of **Natural and Applied Sciences** _____

Prof. Dr. Altuğ Özpineci
Head of Department, **Physics** _____

Prof. Dr. Mehmet Parlak
Supervisor, **Physics Dept., METU** _____

Examining Committee Members:

Prof. Dr. Çiğdem Erçelebi
Physics Dept., METU _____

Prof. Dr. Mehmet Parlak
Physics Dept., METU _____

Prof. Dr. Raşit Turan
Physics Dept., METU _____

Prof. Dr. Bahtiyar Salamov
Physics Dept., Gazi University _____

Assoc. Prof. Dr. Nurdan Demirci Sankır
Materials Science and Nanotechnology Dept., TOBB ETÜ _____

Date 01.02.2018

I hereby declare that all information in this document has been obtained and presented in accordance with academic rules and ethical conduct. I also declare that, as required by these rules and conduct, I have fully cited and referenced all material and results that are not original to this work.

Name, Last Name : Özge Bayraklı

Signature :

ABSTRACT

DEPOSITION OF Cu-Zn-Sn-Se (CZTSe) THIN FILMS AND INVESTIGATION OF THEIR DEVICE PROPERTIES

Bayraklı, Özge
Ph.D., Department of Physics
Supervisor: Prof. Dr. Mehmet PARLAK

January 2018, 117 pages

Thin Film Solar Cell has received a considerable attention in the photovoltaic industry. While the efficiency of thin film amorphous silicon is about %14, the efficiency of $Cu(In,Ga)Se_2$ (CIGS) thin film based solar cells which are very popular in recent years, reached the value of %20. But CIGS based solar cells have some constraints such as their extensive and large scale production in terms of availability of its constituent elements. On the other hand, Kesterite based solar cells such as $Cu_2ZnSnSe_4$ (CZTSe) have been more popular due to their constituent elements, such as Zn and Sn which are more abundant and less expensive than In and Ga. These thin film materials are direct band gap semiconductors. Their absorption coefficient values are over 10^4 cm^{-1} and the band gap values of them are in the range of 1.45-1.6 eV. These values are close to the values for the ideal solar cell. In this study, Cu-Zn-S-Se compounds belonging to Kesterite family have been deposited as a thin film. Thermal evaporation has been used as deposition method. Then electrical, optical and structural characterizations of CZTSe thin films have been carried out and the device application of the thin film has been studied to get efficient solar cell production.

Keywords: Kesterite, CZTSe, thin film, characterization, heterojunction

ÖZ

Cu-Zn-Sn-Se (CZTSe) İNCE FİLMLERİNİN ÜRETİLMESİ VE AYGIT ÖZELLİKLERİNİN BELİRLENMESİ

Bayraklı, Özge
Doktora, Fizik Bölümü
Tez Yöneticisi : Prof. Dr. Mehmet PARLAK

Ocak 2018, 117 sayfa

İnce film güneş pilleri fotovoltavik endüstrisinde hatırı sayılır ölçüde önem kazanmıştır. İnce film amorf silisyum güneş pilllerinde verim %14'ler civarında iken son günlerde popüler olan Cu(In,Ga)Se2 (CIGS) ince film bazlı güneş pillerinde maksimum verim %20'lere ulaşmıştır. Fakat CIGS'e dayalı güneş pillerinin maliyetleri, büyük ölçekli üretiminin zorluğu ve kendisini meydana getiren elementlerin bulunabilirliği bu yapılara bazı kısıtlamalar getirmektedir. Öte yandan, Cu2ZnSnSe4 (CZTSe) gibi Kesterit tabanlı güneş hücreleri Zn ve Sn gibi kendisini meydana getiren elementlerin In ve Ga elementlerine oranla daha ucuz ve doğada daha bol miktarda bulunmaları sebebiyle daha popüler olmaya başlamıştır. Bu yeni ince film yapıları, direk bant aralıklı yarıiletkenler olup, soğurma katsayısı 10^4 cm^{-1}'in üzerinde, yasak band aralığı ise 1.45-1.6 eV civarındadır. Bu değerler ideal güneş pili için gereken değerlere çok yakındır. Bu çalışmada öncelikle kesterit ailesine ait Cu-Zn-Sn-Se bileşiği ince film olarak büyütülmüştür. Büyütme ısısal buharlaştırma tekniğinde yararlanılarak gerçekleştirilmiştir Sonrasında verimli bir güneş hücresi üretimi için bu ince filmlerin elektriksel, optiksel ve yapısal analizleri gerçekleştirilmiş ve bu ince filmlerin aygıt uygulamalarındaki davranışları çalışılmıştır.

Anahtar kelimeler: Kesterit, CZTSe, ince film, karakterizasyon, hetero-eklem

To my family and my life-mate

ACKNOWLEDGMENTS

I would like to express my deepest gratitude for my supervisor Prof. Mehmet Parlak for the continuous support of my Ph. D study and research, for his patience, motivation, and immense knowledge. His guidance helped me in all the time of research and writing of this thesis. Thank you for giving me the opportunity to grow in this field of research.

Besides my advisor, I would like to thank my thesis progress committee: Prof. Raşit Turan and Prof. Bahtiyar Salamov for their insightful comments and encouragement, but also for the hard question which incented me to widen my research from various perspectives. I would like to thank Assoc. Prof. Nurdan Demirci Sankır for her comments during my defense. Also, I would like to thank Prof. Çiğdem Erçelebi for helping me with her knowledge and experience to broaden my horizon in this field.

I would like to thank Dr. Hasan Hüseyin Güllü for sharing his knowledge and experience during my study. I would like to thank Makbule Terlemezoğlu (my ahiretlik) for pushing me all day and night, for the sleepless nights before deadlines and for all the fun we have had in the lab. My sincere thanks also goes to Dr. Tahir Çolakoğlu, Dr. İdris Candan, Dr. Emre Coşkun, Assoc. Prof. Dr. Dilber Esra Yıldız, Çiğdem Doğru, Cansu Emir and Merve Demir for their valuable help while my research. Also, I would like to thank Ergi Dönerçark, Kurtuluş Abak, and all GUNAM members. I would also like to thank Yücel Eke, Nevzat Görmez, Tayfun Yıldız for their help to handle any technical problems in the lab. In particular, I am grateful to Gülşen Özdemir Parlak, and Zeynep Eke for their behavior in a friendly manner whenever I go to fourth floor of the Physics Department.

I would like to thank my friends Özlem Fatma Yıldırım, Kübra Erkan Türkmen, Kübra Eren, Ebru Oral, Dr. Funda Özdemir Değirmenci, who helped me through all the stressful periods in my Ph. D. education. I would also like to thank Ayşenur Gencer (my sister) who always there when I need encouragement.

Nobody has been more important to me in the pursuit of this thesis than my life-mate: Dr. Gökhan Sürücü. He always helps me while my research with his patience and encouragement.

Last but not least, I would like to thank my family for their continuous support and belief in me - they allowed me to spend most of the time on this thesis.

I would like to thank TÜBİTAK, Turkish Scientific and Technical Research Council, for awarding scholarship (2211/A) during my doctorate programe. With this scholarship, I was eager to my research.

TABLE OF CONTENTS

LIST OF FIGURES

LIST OF TABLES

CHAPTER 1

INTRODUCTION

The crucial challenge of the 21st century is the rapid growth of energy demand. The limited resources of fossil fuels and the global climate change due to the usage of these fuels are pointed out the renewable energy resources. Within all the renewable energy resources, solar energy has the greatest potential to meet the need of the world energy demand owing to properties such as; environment friendly, longevity and cost-effective. Photovoltaic (PV) technologies are by far the most developed technologies that can directly convert sunlight to electricity. Total global capacity overtook 150 gigawatts (GW) in early 2014. It is visualized that, PV generation would contribute 17% of all clean electricity, and 20% of all renewable electricity [1].

Silicon is by far the most studied and commercially used as PV absorber when compared to other technologies, as seen from Figure 1 [2].

The first Si PV module was fabricated by Bell Laboratories in 1955 and this technology was chased for powering spacecraft by NASA. Then for the next 20 years, space applications became the dominant area for the usage of Si PV modules. The terrestrial usage of Si PV started to become popular in the mid-1970s and this popularity has been hold overwhelmingly since then [3]. However, some drawbacks such as having the indirect band gap and the week absorption coefficient, which requires a thick absorber layer (>100μm) to absorb the all of the incident light, make Si to be far from an ideal material for PV applications.

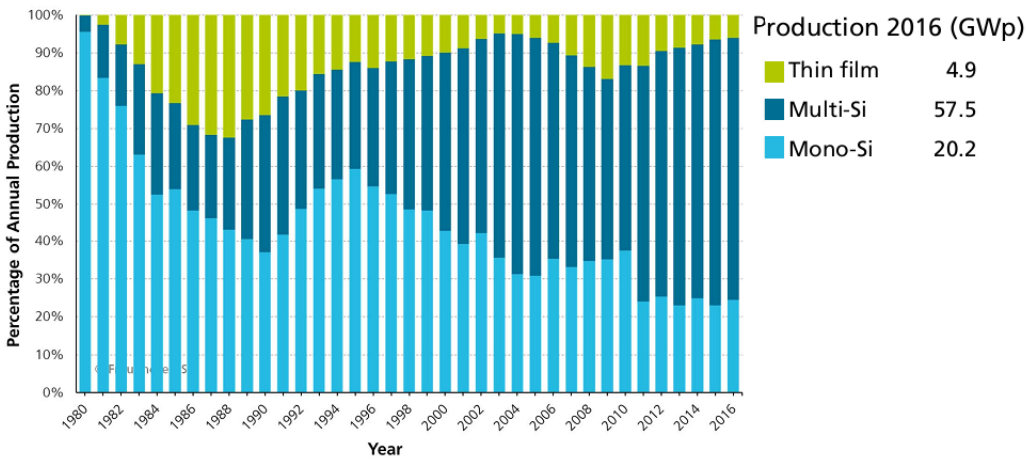

Figure 1. 1 Plots for the distribution of PV technologies from 1980 to 2016 (Adopted from Ref.[2])

The perfect single crystal substrates are needed to be used for getting high efficiency solar cell due to necessity of grain boundaries which are active recombination centers; hence raising the cost. These issues countermine to reduce the cost of Si solar cells [4]. Therefore, the developments for suitable band gap materials in the solar cell application have been crucial.

Thin film solar cells are the powerful candidate to Si solar cells. Direct band gap materials such as CdTe, $CuInS_2$ (CIS), and $CuInGa(S,Se)_2$ (CIGS) have high absorption coefficient of 10^4-10^5 cm^{-1}. Therefore, with having the thickness value of 1-2μm reduces the necessities for crystal quality [5]. These widely used thin film absorber layers currently demonstrate record cell efficiency of 21.7% and 21.5% for CIGS and CdTe, respectively [6], [7] . Although CIGS and CdTe based thin film solar cells have achieved impressive power conversion efficiencies in the laboratory scale, the materials commonly used for their production are either toxic (e.g., cadmium) or rare in the earth's crust (e.g., indium, gallium, tellurium). Therefore, one major demand for thin-film photovoltaic technology is to develop materials composed of earth-abundant and nontoxic elements.

The family of kesterite compounds (eg. Cu_2ZnSnS_4 (CZTS), $Cu_2ZnSnSe_4$ (CZTSe), and $Cu_2ZnSn(S_xSe_{1-x})_4$ (CZTSSe)) are made of copper, zinc, tin, and sulfur or selenium which are very abundant in the earth's crust and inexpensive. They have been an emerging solar cell absorbers, which are structurally similar to chalcopyrite semiconductors, such as CIS, and CIGS, but contains only earth-abundant, nontoxic elements and has a near optimal direct band-gap energy that can be tuned between 1.0 and 1.5 eV changing the compositions of the constituent elements with high optical absorption coefficients [8]–[10]. The fact of kesterite compounds being isoelectronic to chalcopyrite means that a number of its material properties (e.g., the crystal structure and tensor properties) are very similar to chalcopyrite semiconductors. This suggests that the same production methods can be used and photovoltaic devices have been successfully prepared using the same device design, and processing as chalcopyrite solar cells.

The distribution of efficiency obtained by different base material is shown in Figure 1.2. As seen from the figure, the recent cell efficiency of CZTSSe-based thin film solar cell is high enough though it is a very new technology[11].

Many research and experiments have been carried out related to this topic recently and efficient solar cell devices have been improved. The deposition techniques to fabricate CZTSSe thin films can be classified as vacuum and non-vacuum based methods. Vacuum based techniques such as sputtering and evaporation are more suitable for mass production to obtain highly uniform thin film. In the literature, the works related to vacuum based techniques can be found as one-step and two-step processes. One-step vacuum depositions originate in simultaneously combining all the elements. The most influential ones among these techniques to deposit high-quality CZTSSe thin films for good PV performance are co-sputtering and co-evaporation. Another vacuum based deposition technique is two-step process. In this process, the precursors are first combined during an ambient temperature process like evaporation or sputtering, then it is followed by an annealing step. The annealing step could be a selenization or sulphurization process due to the desired structure [12]–[17].

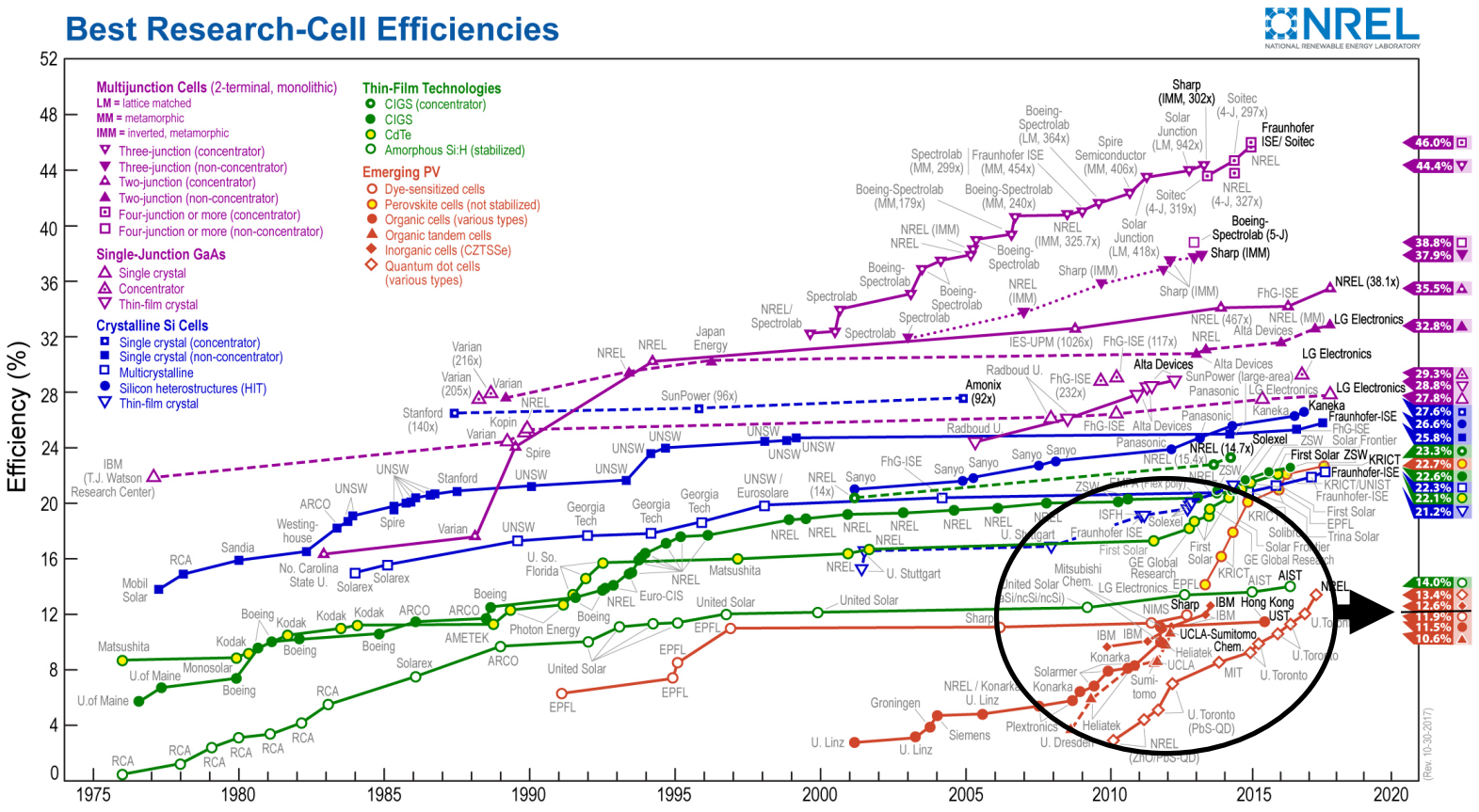

Figure 1. 2 Plots for the record Power Conversion Efficiency distribution of PV technologies from 1980 to 2017[11]

Non-vacuum methods such as spray pyrolysis deposition, electrodeposition and sol-gel deposition technique can supply some advantages such as low cost and very simple process. The world record efficiency for CZTSSe solar cell (12.6 %) has been achieved by one of these methods which includes the simultaneous use of spin-coating solution and particles of constituents [18]. There are also other methods such as electroplating to achieve good device performance for CZTSSe [19]. On the other hand, there are some weak points of non-vacuum techniques such as the usage of toxic and dangerously instable solvents which are hard of recycling as hydrazine.

The plots of the conversion efficiencies that has been reported so far versus years for CZTS-based thin film solar cells are also given in Figure 1.3. As can be seen from the figure, the efficiency of the CZTS-based thin films have been increased almost %10.

The first reported research including device efficiency was done by Katagiri et al. Cu/Sn/Zn stacked layers on soda lime glass (SLG) was deposited by using electron beam evaporation. Then, followed process was sulphurisation with the configuration of SLG/Mo/CZTS/CdS /ZnO/Al, they obtained the efficiency of device as 0.66% in 1997 (V_{oc}=400mV, J_{sc}=6.0 mA cm^{-2}, FF=0.277) [20]. Friedlmeier et al was reported on the conversion efficiency of 2.3% with the same device configuration of Katagiri et al's in 1997. In 1999, Katagiri et al reached the conversion efficiency of 2.62 % for CZTS thin film solar cell with the two-step method in which sulphurization process was carried out following the electrodeposited Cu/Sn/Zn precursors. (V_{oc}=522mV, J_{sc}=14.1 mA cm^{-2}, FF=0.335) [21].

Then with the optimization of the sulphurization process, the new record conversion efficiency was obtained as 5.4%. Moreover, with the etching of absorber layer after the annealing process, the conversion efficiency reached to 6.7 % [21].

Using co-evaporation technique, Wang et al. reported the efficiency of CZTS device as 6.8% in 2010. CZTS films exposed to NaCN etching before the CdS deposition in this work. They deduced that high series resistance affected performance of device negatively[22].

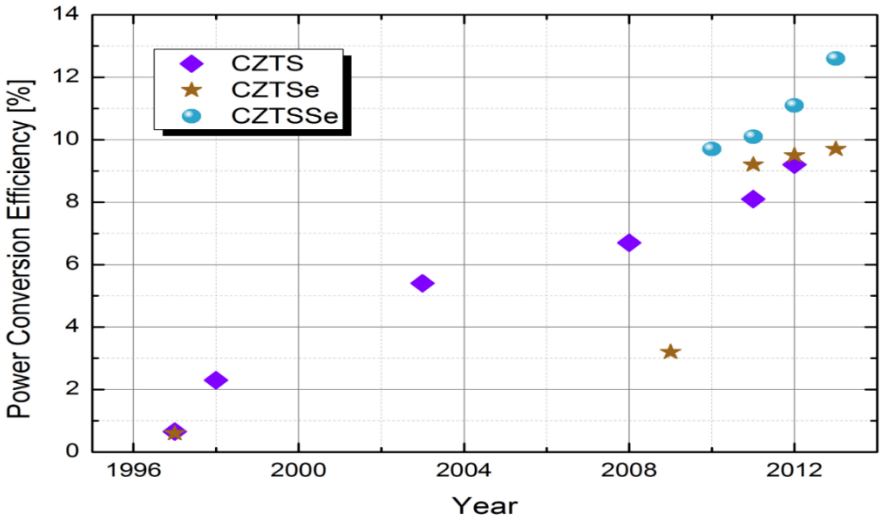

Figure 1. 3 Plots for the record Power Conversion Efficiency distribution of CZTSSe solar cells as a function of years[23]

In 2011, the highest record efficiency for pure sulfide Cu_2ZnSnS_4, was reported Shin et all. Where the research was based on thermal evaporation of Cu, Zn and Sn. Also, the device structure was composed of interfacial layer (MoS_x) having thickness 110nm, absorber layer (600nm), CdS (100nm), ZnO (80nm), Al doped ZnO (450nm), Ni-Al fingers and MgF_2(100nm). They obtained the efficiency of solar cell as 8.4% [12]. In 2013, the new records for pure sulfide CZTS was achieved as 9.2% with using co-sputtering by Kato et al. and Brammertz et al. [24].

Besides, Friedlmeier et al. reported on the conversion efficiency of 0.6% for kesterite including selenidee, which is also called as CZTSe, based devices by using vacuum-based method in 1997[25]. Then the efficiency of CZTSe based devices reached to 3.2% in 2009[26]. In 2012, the conversion efficiency of 9.5% was achieved with coevaporated CZTSe by Repins et al. [27].

Furthermore, the world record efficiency for the chalcogens intermixing, which is introduced in the alloying forming CZTSSe, based thin film solar cell, was announced by solar frontier that they achieved the efficiency of solar cell as 12.6% by using

hydrazine pure solution in 2014 [18]. Considering the highly toxic and explosive nature of hydrazine, this method is not suitable for the mass production. Due to its suitability for large scale production, vacuum based (Physical Vapor Deposition) PVD techniques such as sputtering and thermal evaporation are the most widely used techniques.

The main goal of this study is to achieve deposition of CZTSe thin films by using physical vapor deposition and investigation of the device applications of CZTSe thin films. The novelty of the work is the variation from the literature with the single step deposition method which covers elemental sources and in-situ selenization procedure. In chapter 2, the theoretical considerations are presented in order to highlight the physics behind of this study. The experimental setups and instrumentations which are used during the work, are explained in chapter 3. Chapter 4 is composed of the results and discussions for the deposition and characterization of CZTSe thin films. Following chapter 4, device applications of CZTSe thin films are detailed and discussed in chapter 5. Finally, the thesis concludes with a summary of the study in chapter 6.

CHAPTER 2

THEORETICAL CONSIDERATIONS

2.1 Introduction

This chapter introduces the details about the material properties and device physics which were necessary for PV studies. Firstly, the material properties of kesterite compounds were detailed. In this concern, structural properties (which covers crystal structure, composition and phase diagram), electronic band structure and defects and defect complexes of these compounds were expressed. Then, the physics of solar cell operation is explained.

2.2 Material Properties

2.2.1 Structural Properties

In order to obtain the semiconductor compounds with new physical and chemical properties, Grimm–Sommerfeld method could be used. This method is the prediction of the compositions of chemical compounds with the tetrahedral and octahedral (rock salt-type) coordination of atoms in their crystal lattice [28]. It can be expressed in the form of the equation system as follows [29] ;

$$\sum_{i=1}^{A} B_i x_i = 4$$

$$\sum_{i=1}^{n} B_i\, x_i = \sum_{i=n+1}^{A} (8 - B_i) x_i \qquad (2.1)$$

$$\sum_{i=1}^{A} x_i = 1$$

where A is the number of the components and n is the cation numbers. B_i is the number of the group of the periodic table to which the ith component of the compound belongs and x_i is the concentration of B_i in the compound.

The first expression of equation 2.1 indicates that the condition for the average number of valance electrons per atom that is equal to four and corresponds to tetrahedral rule. The condition that the number of valance electrons which cations give to anions is equal to the number of electrons, the anions need in the compound to form octet is stated in the second term of the equation. Due to these conditions, all possible types of tetrahedral semiconductors could be obtained by considering the location of the components in one or another group of the periodic table [30]. The multinary semiconductor system of Cu_2-II-IV-VI_4 obeys the Grimm-Sommerfeld rule. For this system Cu, group II, and group IV atoms are the cations ($i = 1\ to\ 3$) and group VI atoms are the anions ($i = 4$),

2.2.1.1 Crystal Structure

The Cu_2-II-IV-VI_4 semiconductors normally crystallize in the tetragonal or orthorhombic structure. The tetragonal structures of Cu_2-II-IV-VI_4 semiconductors crystallize in the kesterite or stannite structure. Figure 2.1 illustrates these two structures. These structures are very similar but they belong to different space groups as $I\overline{4} = S_4^2$ and $I\overline{4}2m = D_{2d}^{11}$ for kesterite and stannite, respectively. This difference originates from the different distributions of the cations of Cu and group II. As seen

from Figure 2.1, each VI group atom (anion) is surrounded by two Cu, one II and IV group atoms for both structures. However, it is not easy to determine whether the crystal structure belongs to kesterite or stannite.

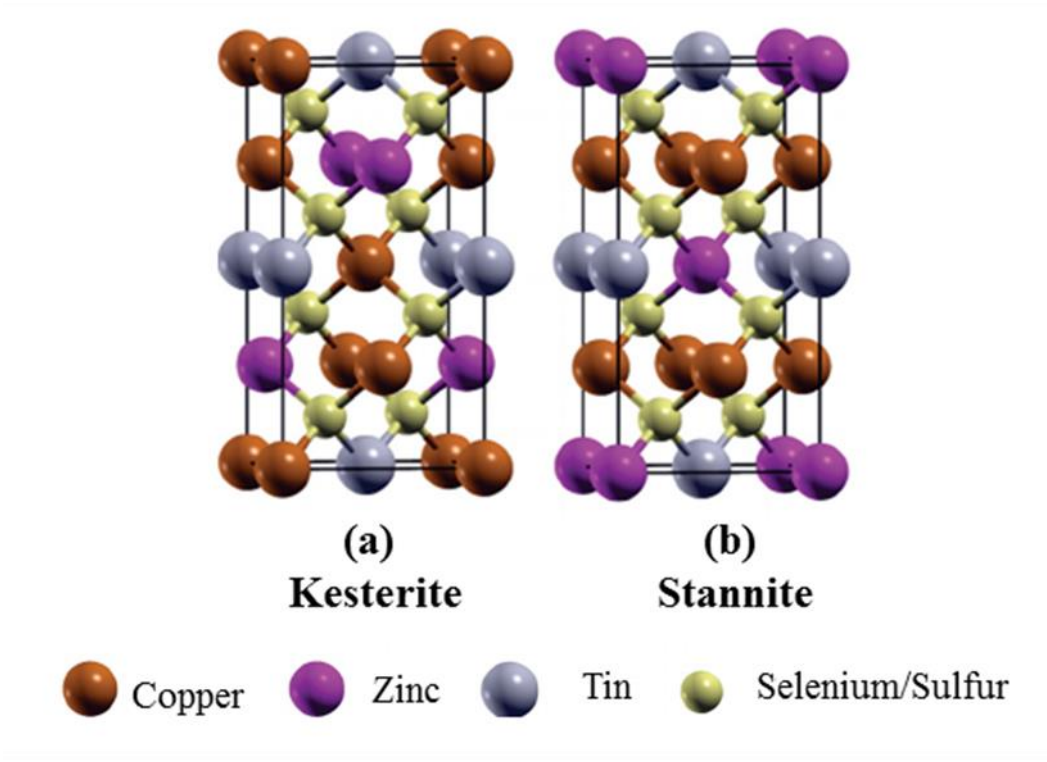

Figure 2. 1 (a) Kesterite and (b) Stannite structures for CZTSSe

Quaternary Cu_2-II-IV-VI_4 semiconductors are derived from binary Zinc Blende (ZB) and Wurtize structures. While the WZ-stannite structure is WZ- derived structures, the kesterite and stannite structures are ZB- derived. Figure 2.2 shows WZ-kesterite and WZ-stannite structures. These structures are also not easily distinguishable. The space group of WZ-kesterite structure is $Pc = C_s^2$ and the WZ-stannite one is $Pmn2_1 = C_{2v}^7$. They are both noncentrosymmetric with the crystal symmetry of monoclinic and orthorhombic for WZ-kesterite and WZ-stannite, respectively.

The first-principle calculations for Cu_2-II-IV-VI_4 compounds in the literature pointed out that the kesterite structure is energetically more stable than the stannite structure [31][32][33].

Experimental XRD patterns are not sufficient to identify the structure whether it is kesterite or stannite. Because of the delicate differences in the degree of tetragonal distortion which is defined by c/2a display a very weak modulation in the peak splitting of higher-order phases such as (220)/(204) and (116)/(312) [31], [34]–[36].

2.2.1.2 Composition and Phase Diagram

Getting pure single-phase kesterite structure is a very challenging issue. In order to determine the composition of the cations in the structure, the ratios of atomic percentages [Cu]/([Zn]+[Sn]) and [Zn]/[Sn] are generally used. For the stoichiometric material, these ratios must be equal to one. On the other hand, the anions (S,Se) are independent variables. The most useful way to summarize compositions in the Cu-Zn-Sn system is a ternary phase diagram of the Cu_2Se-ZnSe-$SnSe_2$ or (Cu_2S-ZnS-SnS_2). Figure 2.2 illustrates Cu_2Se-ZnSe-$SnSe_2$ pseudo-ternary systems at 670 K [37] where a very limited region of stability for single phase CZTSe kesterite structure is shown. When compared to chalcopyrite structure, kesterite structure is highly sensitive to composition [31], [38], [39]. For instance, the stability region of $Cu_2ZnSnS_4$for Cu-rich condition in the chemical potential μ_{Sn}–μ_{Zn} diagram is about 0.1 eV wide stability region compared to the 0.5 eV wide stability region for $CuInSe_2$ [31], [40]. The studies based on ab initio calculations and experimental results also concluded that single-phase kesterite is far more difficult to prepare as compared to chalcopyrite.

As yet, Cu-poor and Zn-rich compositions are generally dominant in high-efficiency CZTS(Se)-based solar cells. Composition ratios for the best solar cells were found be around 0.8-0.9 and 1.1-1.2 for Cu/ (Zn + Sn) and Zn/Sn, respectively. Moreover, the stoichiometric CZTS(Se) devices were limited to only ~5% efficiency range, suggesting that Zn-rich composition is favorable [31].

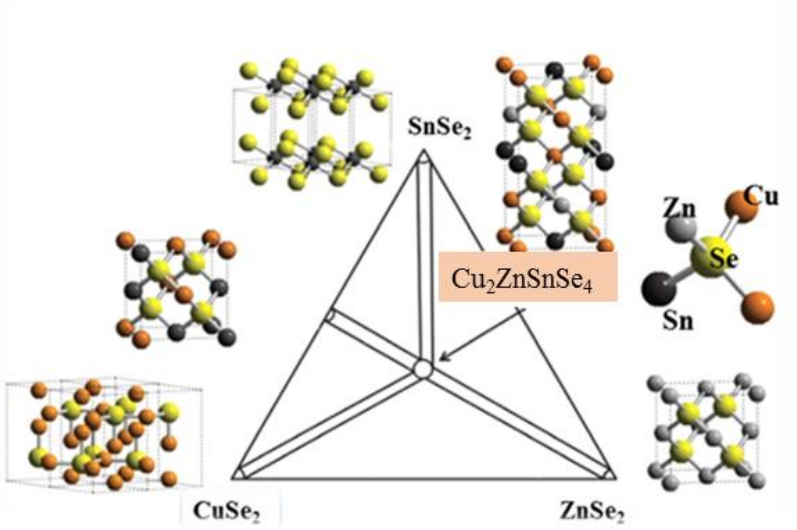

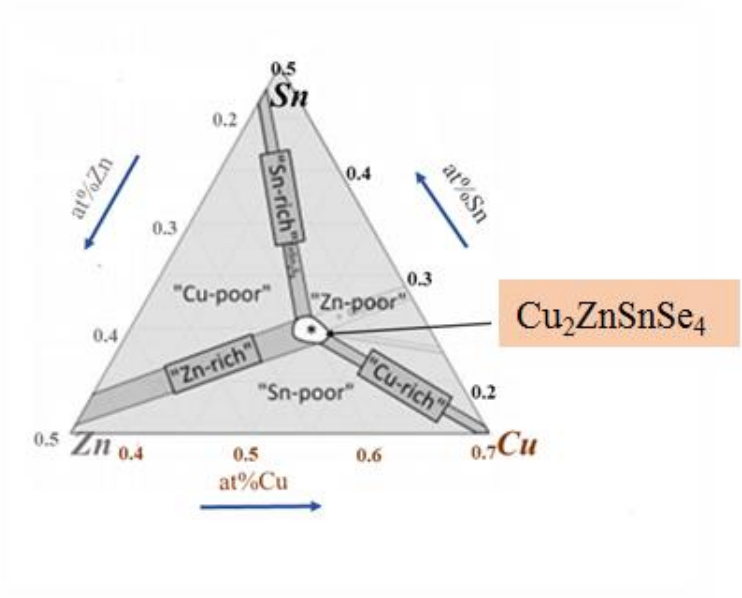

Figure 2. 2 Phase diagrams for CZTSe structure

Secondary phases such as ZnS(Se) and $Cu_2SnS(Se)_3$ in the Zn-rich regime could be formed during the absorber layer fabrication process. Additionally, ZnS has been found to be the predominant secondary phase for the Cu-poor and Zn-rich condition

by Nagoya et al. [38]and Maeda et al. [41]. On the other hand, experimental studies also confirmed the existence of the ZnSe secondary phase in $Cu_2ZnSnSe_4$ films [42], [43]. ZnS or ZnSe (ZnS(Se)) secondary phases have higher band gap and their conductivities are lower compared to CZTSSe, so these secondary phases are not responsible for reduced shunt resistance or open-circuit voltage except for high series resistance[4], [42]. But then, other secondary phases such as SnS_x, $SnSe_x$ or $CuS(Se)_x$ are regarded as more detrimental due to their lower bandgap and higher conductivity. These situations could affect photovoltaic performance of the device with reducing the open-circuit voltage and the shunt resistance [44].

2.2.2 Electronic band structure

The chalgogens (S,Se) concentration in CZTSSe compounds offer the opportunity to get different material properties for a desired application.

Density functional theory (DFT) calculations in the literature showed that, $Cu_2ZnSn(S_xSe_{1-x})_4$ compounds have direct band gap at the Γ-point. Calculated band gap values decrease 1.5 eV to 1.0 eV by changing "x" value 1 to 0 with a very small bowing parameter due to the Equation (2.2),

$$E_g(x) = (1-x)E_g(CZTSe) + xE_g(CZTS) - bx(1-x) \qquad (2.2)$$

Here, b is a bowing parameter and it is about 0.1. S and Se atoms are belonging to same group of the periodic table therefore they have similar chemical properties. So, these properties make the bowing parameter very small. Due to having very small b value, E_g could be approximate as linearly dependent on "x" value [45].

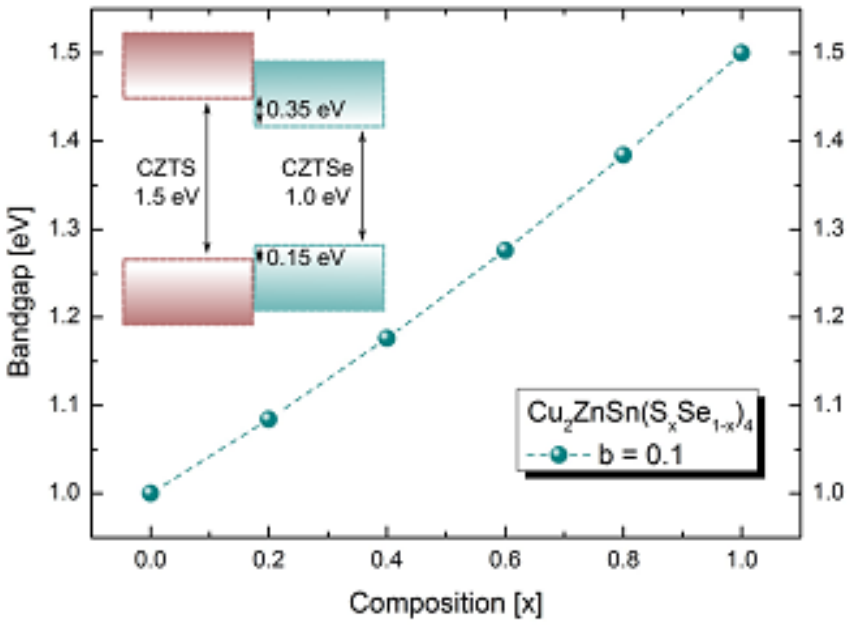

Figure 2. 3 Variation of the band gap values depending on the composition for CZTSSe structures

The bang gap value of matter decreases from pure S to pure Se kesterite structure shown in Figure 2.3. In order to show how this trend occurs such as contribution from valance and conduction bands, the band offset was calculated in the literature [45]. Figure 2.4 illustrates the band alignment between CZTS and CZTSe structures. It can be seen from the figure that the valance band is lower and the conduction band is higher at the CZTS side when compared to the CZTSe side. This band alignment between CZTS and CZTSe is called as type I. Once an interface formed between these two materials, both hole and electron states are localized on CZTSe.

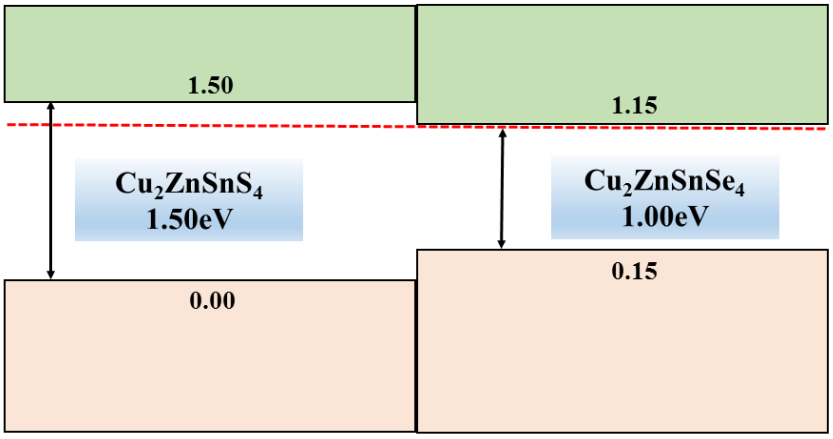

Figure 2. 4 The band alignment between CZTS and CZTSe structures

This band alignment could be explained due to the nature of valance band maximum (VBM) and conduction band maximum (CBM) states as given below;

(i) The VBM is an antibonding state of the anion *p* and Cu *d* orbitals for quaternary and ternary chalcogenides such as Cu_2ZnSnS_4, $Cu_2ZnSnSe_4$, $CuInSe_2$ etc. Having the lower *p* level of S atoms makes the VBM of sulfides lower than that of the selenides. This difference is caused by *p-d* hybridization in Cu based chalgonides. The hybridization in the Cu-S bond is stronger so it pushes the antibonding VBM level of the sulfide compounds up relative to that of selenide ones. Therefore, there is about 0.15 eV difference in the valance band offset in between CZTSe and CZTS as illustrated in Figure 2.7

(ii) The antibonding state of the anion *s* and Sn *s* orbitals makes the CBM of CZTS and CZTSe. The *s* level of Se is 0.2 eV higher in energy than S. On the other hand, the shorter bond length of Sn-S constructs this level repulsion stronger in CZTS and moves its CBM up relative to CZTSe.

The differences in the conduction band offset (0.35 eV) is larger than the valance band offset (0.15) shown in Figure 2.7, therefore S/Se ratio plays an important role in the band gap value [45]–[48]

2.2.3 Defects and defect-complexes

CZTSSe compounds have a wide range of possible defects owing to having many number of constituent atoms. These defects could be caused by growth conditions and variation from stoichiometry. They can be categorized as vacancies, antisites, interstitial and defect-complexes and these defects could be located deep or shallow in the bandgap and the concentration of them generally depends on their formation energy [23], [45], [49]. The defects in shallow level may affect the concentration of minority and majority carriers in this manner conductivity, though the defects in the deep level can act as recombination centres for photo generated electron-hole pairs [50].

Among the vacancies (V_x and x= Cu,Sn,Zn,S,Se), V_{cu} lead to a shallow acceptor level about 0.02 eV above the VBM and enhance the p-type nature of the CZTSSe absorber layer. Therefore, this situation is beneficial device efficiency. On the other hand, all vacancies except the copper ones are not favorable [51]–[53]. For instance; X=S, Se create mid gap states and X= Sn,Zn form both deep levels and mid gap states as multiple states [54], [55]. Having the similar valances and radii of elements like zinc and copper leads to form antisite defects in CZTSSe. These type of defects may form either donor or acceptor level in CZTSSe due to their transition levels and defect formation energies. Cu_{zn} which is the copper on the zinc antisite acts as a shallow acceptor while Zn_{cu} acts as a shallow donor level. Tin on the copper antisite (Sn_{Zn}) forms both shallow level and the mid-gap states. Likewise, Sn_{Zn} forms two mid-gap states. On the other hand, copper on tin antisite (Cu_{Sn}) leads to formation of three transition levels [51], [55]. Cu_i and Zn_i are the most commonly detected interstitial defects for stoichiometric CZTSSe or Cu-poor conditions. These type of defects are undesirable because Cu_i forms the shallow donor and Zn_i forms the mid-gap states. Hence, Cu-poor and Zn-rich stoichiometry can be accepted for the higher solar cell efficiency [56]. In addition to defects mentioned above, defect-complexes are the another dominating defects seen in CZTSSe structure. The defect-complexes can be categorized as stoichiometric-conserving and non- stoichiometric-conserving defect complexes. (Cu_{Zn}+Zn_{Cu}), (Cu_{Sn}+Sn_{Cu}) and (Zn_{Sn}+Sn_{Zn}) are the stoichiometric-

conserving defect complexes. They can be represented as (X_Y+X_Y) and formed when element X replaces Y in one antisite and element Y replaces X in another antisite. (V_{Cu}+Zn_{Cu}), (V_{Zn}+Sn_{Zn}), (Zn_{Sn}+2Zn_{Cu}), (2Cu_{Zn}+Sn_{Sn}) are the non- stoichiometric-conserving defect complexes. While the stoichiometric-conserving defect complexes do not have any effect on variation of the stoichiometry, non-stoichiometric one causes local variation in the stoichiometry of CZTSSe.

2.2 Device Properties

2.2.1 P-N Junction

Semiconductors are categorized as intrinsic and extrinsic semiconductors. By doping an intrinsic semiconductor, n-type semiconductor is formed. Hence, electron concentration is larger than hole concentration in n-type semiconductors. The dopant atoms provide extra electrons to the intrinsic material. Electrons are the majority carriers and holes are the minority carriers in n-type semiconductors. Fermi level for n-type semiconductor stays closer to the conduction band than the valance band.

There is larger hole concentration than electron concentration in p-type semiconductors so holes are the majority carriers in this type of semiconductors. This type of semiconductors are formed by doping acceptor impurities into intrinsic semiconductors. Also, the Fermi level stays closer to valance band than conduction band so it is below the intrinsic Fermi level[57].

P-N junctions are two terminal devices which are formed once p- and n-type materials are joined together and they allow exchange of carriers until the equilibrium reached. The differently doped (p- and n-type) same semiconductor forms homojunctions while two different materials with different doping types are joined together to form heterojunction.

When p and n-type semiconductors are brought into contact, electrons from the n-side (just near the contact interface) diffuse to p-side because of the concentration differences of carriers in both sides and similarly, holes diffuse from p-side to n-side.

Hence, diffusion currents are formed in the junction. The diffusion of electrons from n-side into the p-side leaves behind ionized donor levels (called as N_d) , and the diffusion of holes from p-side to n-side leaves behind also ionized acceptor levels (called as N_a). The mobile carriers diffuse in the region near the p-n junction and they leave behind fixed charges. This area is called space charge or depletion region because it is depleted of charges. Figure 2.5 shows the p–n junction in thermal equilibrium with zero-bias voltage applied and bottom, plots in the figure are showed the charge density, the electric field, and the voltage are given[58].

As seen in the figure, a negative charged area forms around the p-side, and a positive charged area forms near the n-side. So an electrical field is formed and the built-in electric field is in the opposite direction to the diffusion current. So in a p-n junction, without an external applied voltage bias, it reaches an equilibrium condition. Then a potential difference is formed across the junction region, this potential difference is called as “built-in” potential *Vb* [59].

The depletion region width (*W*), the transition width extending in p-side ($x_{p)}$ and in n-side (x_n) are obtained from the solution of Poisson’s equation by using the depletion approximation and given as [60];

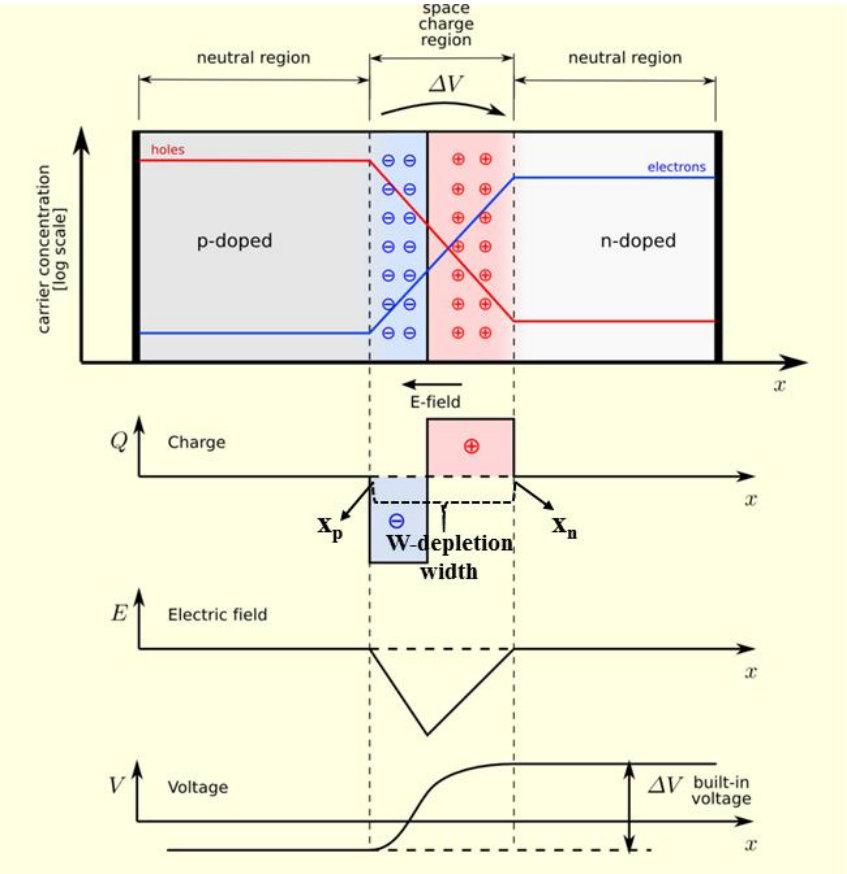

Figure 2. 5 The p–n junction in thermal equilibrium with zero-bias voltage applied and under the junction, plots for the charge density, the electric field, and the voltage are given (adopted from ref [60].

$$W = \left(\frac{2\varepsilon_r \varepsilon_0 V_b}{q}\frac{N_a + N_d}{N_a N_d}\right)^{1/2} \tag{2.3}$$

$$x_p = \left(\frac{2N_a\,\varepsilon_r \varepsilon_0 V_b}{qN_d(N_a + N_d}\right)^{1/2} \tag{2.4}$$

$$x_n = \left(\frac{2N_d \varepsilon_r \varepsilon_0 V_b}{qN_a(N_a + N_d}\right)^{1/2} \tag{2.5}$$

where ε_r ε_0 are the dielectric constants.

Finally, we can write the expression as;

$$N_a X_p = N_d X_n \tag{2.6}$$

The relation given in Equaiton 2.6 indicates that higher doped material has narrower depletion region and lower doped one has wider depletion region at the junction.

The built-in potential is expressed as;

$$V_b = \frac{k_B T}{q} \ln\left(\frac{N_a N_d}{{n_i}^2}\right) \tag{2.7}$$

where k_B, T, q, and n_i representing Boltzmann constant, temperature, charge of the carrier, and intrinsic carrier concentration of the semiconductor, respectively.

The ideal diode equation can be derived by using the built-in potential, depletion width, majority and minority carrier concentrations and other physical properties of the materials. The total current is composed of electrons and holes flowing across the junction in the device with respect to drift and diffusion. The electron current density at the edge between the depletion region and the neutral p-type region is given by

$$J_n = -\frac{q D_n n_{p0}}{L_n}\left(exp\left[\frac{qV}{k_B T}\right] - 1\right) \tag{2.8}$$

where D_n is the diffusion coefficient for electron, n_{p0} is the electron concentration at the equilibrium in the p-side and L_n is the diffusion length for electron. The minus sign

in the relation means the current in the opposite direction to the p-side. Similarly, the hole current density is given as;

$$J_p = -\frac{qD_p p_{n0}}{L_p}\left(exp\left[\frac{qV}{k_B T}\right] - 1\right) \tag{2.9}$$

where D_p is the diffusion coefficient for hole, n_{p0} is the hole concentration at the equilibrium in the n-side and L_p is the diffusion length for hole. Then the total current density across the junction is given as;

$$J_{total} = J_n + J_p = q\left(\frac{D_n n_{p0}}{L_n} + \frac{D_p p_{n0}}{L_p}\right)\left(exp\left[\frac{qV}{k_B T}\right] - 1\right) \tag{2.10}$$
$$= J_0\left(exp\left[\frac{qV}{k_B T}\right] - 1\right)$$

where J_0 is the reverse saturation current density.

2.2.2 Heterojunction

Heterojunctions can be categorized as graded or abrupt heterojunctions due to the transition distances from one side to the other which is completed at the interface. When the transition distance is about few atomic region, the heterojunction is known as abrupt, in other situation, graded. In 1974, heterostructure in terms of semiconductor technology was, with today's criterion, not be developed. Shockley had incorporated a heterojunction emitter as demanded in the bipolar transistor patent. In addition, Herb Kroemer had offered a number of heterojunction device concepts in the late 1950's and early 1960's. R. L. Anderson had introduced a model for the band alignment, which is based upon the experimentally measured electron affinities of the participating semiconductors, by 1962 [61]. The model developed by Anderson is a keystone and makes a good approximation for the observed behaviour of an ideal p-n junction.

Figure 2.6 illustrates the typical energy-band diagram of two semiconductors having distinct band gaps and types of conductivity. They are at equilibrium and vacuum levels are the common for them. As shown in Figure 2.7, the n-type semiconductor has the larger band gap compared to p-type ($E_{gn}>E_{gn}$). And the work functions (Φ_n , Φ_p), electron affinities (χ_n, χ_p) dielectric constans (ε_n, ε_p) are assumed to be different.

The figure also shows that the built in potential ($V_b=\Phi p-\Phi_n$) is equal to difference of the work functions. The relative band bendings are denoted as V_{Dp} and V_{Dn} for p- and n-side, respectively and sum of them are also equal to the built in potential.

The difference in electron affinities is equal to the difference in the conduction band edges of the two semiconductors. Hence , the band offset ΔE_c can be obtained as;

$$\Delta E_c = \chi_p - \chi_n \tag{2.11}$$

The band offset ΔE_v in the valance band is also found as ;

$$\Delta E_v = E_{gn} - E_{gp} - \Delta E_c \tag{2.12}$$

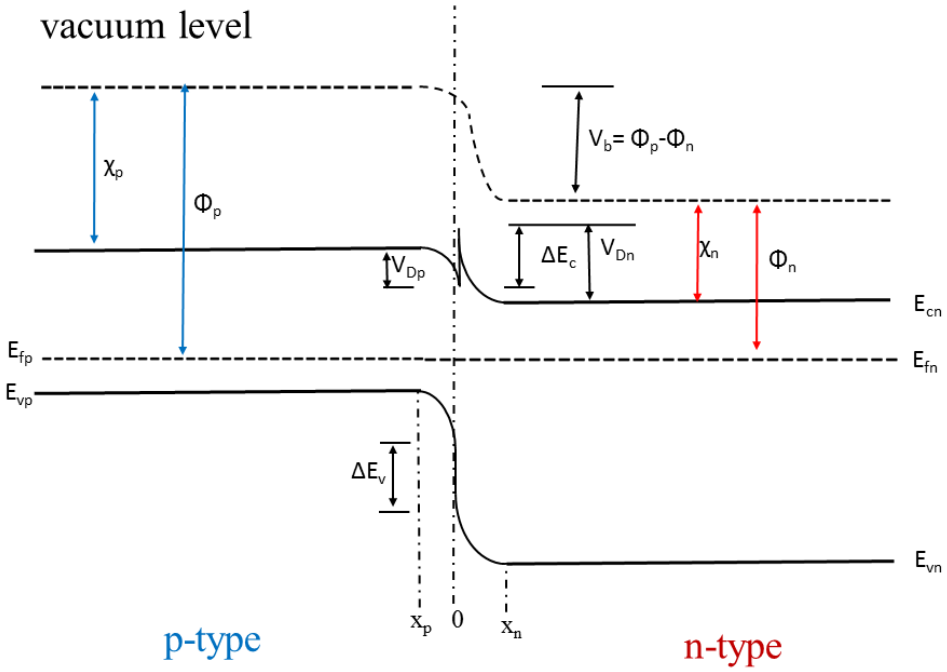

Figure 2. 6 Energy-band diagrams of p- and n-type semiconductors

The sum of the both discontinuities is equal to band gap difference in between the semiconductors;

$$\Delta E_v + \Delta E_c = E_{gn} - E_{gp} \tag{2.13}$$

These band offsets lead to extra barrier and it gives an increment on the recombination of generated carriers in the junction. So, the band gaps and electron affinities must be chosen closer to minimize the band offsets and eliminate the effect of band offset on current flow.

If there is no applied voltage at the junction, the barrier for electrons flow from the n- to p-side is just "qV_{Dn}". On the other hand, for the electrons flow from the p- to n-side is " ΔE_c-qV_{Dp}" as seen in clearly in Figure 2.8. The detailed information about the physics of heterojunctions can be found in the Ref [62].

2.2.3 Solar cells

A solar cell is a p-n junction which converts a photon current into an electron current. This conversion process is achieved by a process called the photovoltaic effect where a voltage is generated within a semiconductor upon exposure to light. Incident photons are absorbed to generate electron-hole pair charge carriers that can pass through an external load to create electrical work [61].

2.2.3.1 Solar radiation

The nuclear reaction inside the sun is the source of the solar radiation energy. This energy is emitted as an electromagnetic radiation. The intensity of this radiation at the average distance from the sun to the earth is about 1.4 kW/m^2 [61] and it is rarefied by the atmosphere when it gets through to the earth. The degree of the incident radiation angle to the atmosphere influence the energy received from the solar radiation at the surface of the earth. The secant of the angle between the sun and the zenith is determined by the air mass (AM). The AM is the path length which light travels through the atmosphere normalized to the shortest possible path length. The AM measures the reduction in the power of light when it passes through the atmosphere and is absorbed by air and dust. Figure 2.7 and Figure 2.8 illustrate the radiation angles of sunlight and solar spectrum belong to various AM conditions, respectively. As seen in Figure 2.7, AM0 corresponds to the solar spectrum belongs to outside the atmosphere of the earth. AM1 corresponds to the sunlight which is at the surface of the earth when the sun is at zenith.

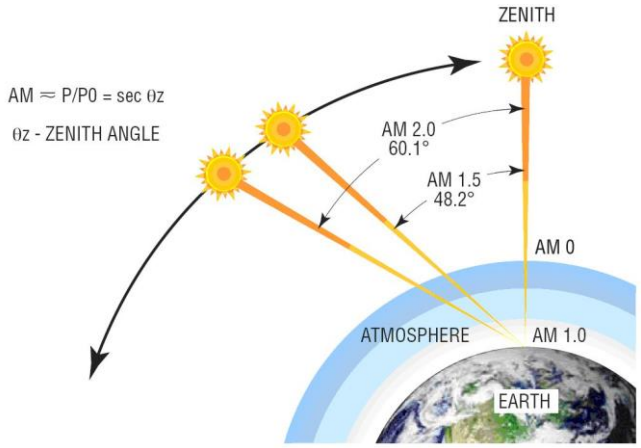

Figure 2. 7 The radiation angles of sunlight (adopted from Ref [65])

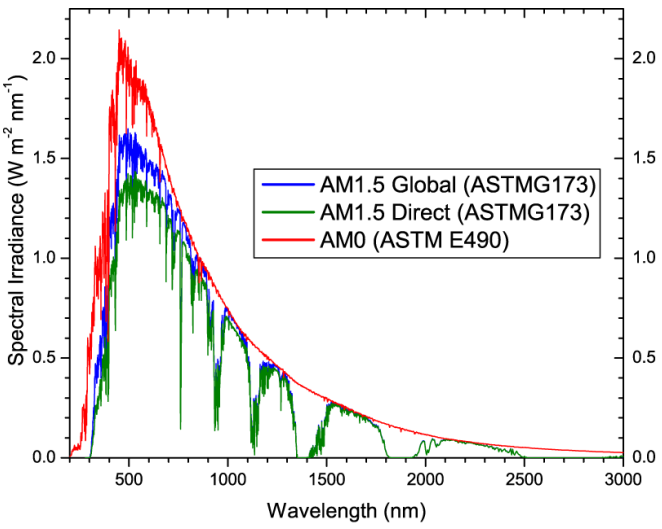

Figure 2. 8 The solar spectrum belong to various AM conditions (adopted from Ref [66])

The power of the sunlight belongs to AM1 is about 925 W/m^2. On the other hand, AM1.5 corresponds to the condition which satisfies energy-weighted average for terrestrial applications. The total power of the incident light is 844 W/m^2 for the AM 1.5 condition. The solar power could be transformed to the photon flux and each photon generates an electron-hole pairs [61].

2.2.3.1 Solar cell operation

The basic operation principle of a solar cell is illustrated in Figure 2.9. When a photon of energy $E_{ph}=h\nu_{ph}$ (where h is the Planck's constant and υ is the frequency of the ligh) is absorbed in a semiconductor with a band gap energy $E_g \leq E_{ph}$, electron-hole pair carriers are generated and can diffuse through the material. Forming a contact junction consisting of a semiconductor with p-type conductivity and a semiconductor with n-type conductivity forms a built in potential difference at the junction. Electron-hole pairs that do not recombine before reaching the junction can be separated by the electric field provided by the built in potential.

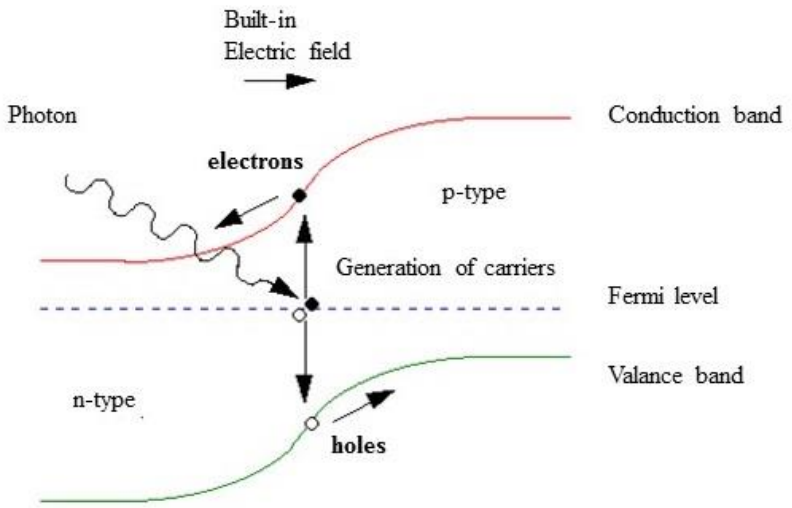

Figure 2. 9 Basic operating principle for solar cell

Solar cells can be considered with an ideal diode I-V characteristics. Figure 2.10 illustrates the equivalent circuit for a solar cell. J_{ph} is the photocurrent density produced by the excitation of the excess carriers by illumination and R_L is the load resistance.

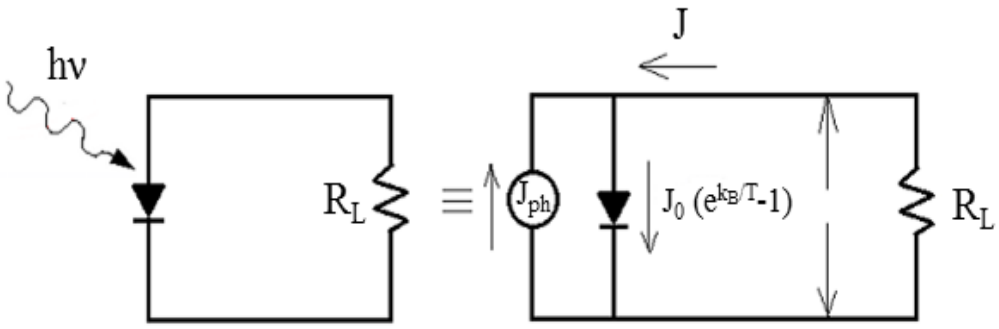

Figure 2. 10 The idealized equivalent circuit for a solar cell

The total current density of a solar cell device under illumination is given by;

$$J = J_0 \exp\left(\frac{qV}{k_B T} - 1\right) - J_{ph} \tag{2.14}$$

The open-circuit voltage, is symbolized as V_{oc}, corresponds to the maximum voltage across a solar cell when the current is zero. The bias originating from the light generating current on the solar cell equals to the open-circuit voltage [63]When the total current density of the device is zero, the open circuit voltage can be expressed as;

$$V_{OC} = \frac{k_B T}{q} \ln\left(\frac{J_{ph}}{J_0} + 1\right) \tag{2.15}$$

The current through the device is called as the short-circuit current density (J_{sc}) when the total voltage across the device is zero.

The source of the short-circuit current is the generation and collection of light-generated carriers. At minimum loss mechanisms, the short-circuit current and the

light-generated current are identical in an ideal solar cell. Hence, the largest current that could be drawn in the cell is the short-circuit current.

The maximum output power obtained from the solar cell is represented by the fill factor (*FF*) and *FF* is in conjunction with J_{sc} and V_{oc}. The parameters V_{oc}, J_{sc} and *FF* are shown in Figure 2.11.

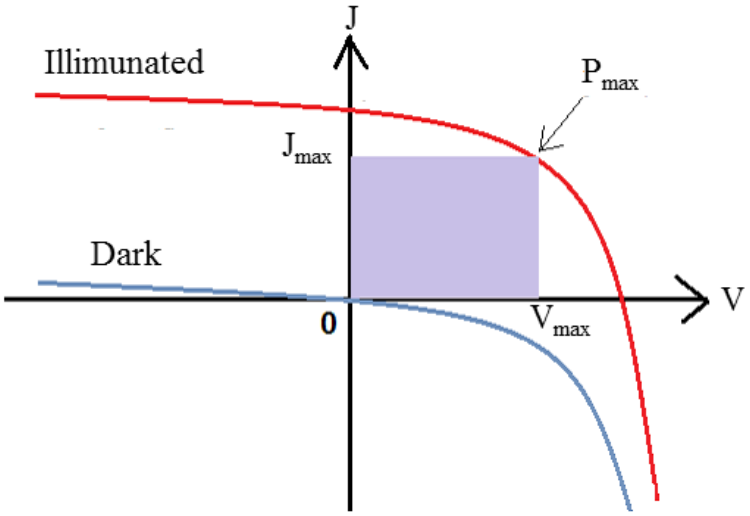

Figure 2. 11 J-V characteristics of a solar cell under dark and illumination conditions

The *FF* is stated as the ratio of the maximum power obtained from the device to the product of J_{sc} and V_{oc}. As seen in Figure 2.11, the *FF* is the area of the largest rectangle that fits the *J-V* curve and is given as [61];

$$FF = \frac{V_{max}J_{max}}{V_{oc}J_{sc}} \tag{2.16}$$

The efficiency of the solar cell is explained as the ratio of energy output from a solar cell to input energy from the solar radiation. The spectrum and intensity of the incident light, the solar cell performance and the temperature are the key factors for the solar cell efficiency. The input power is taken as 100 mW/cm^2 belonging the condition that considers AM 1.5 at room temperature of 25 ^{0}C to measure terrestrial solar cell efficiency[63]. Then the efficiency (η) relation is given as;

$$\eta = FF\frac{J_{sc}V_{oc}}{P_{in}} \tag{2.17}$$

Series resistance (R_s) is created by the current through the base and emitter of the device, resistance in between absorber layer and metal back contact, and the resistance in between top collector and front metal contacts. The series resistance decreases the fill factor and higher series resistance value could also decrease the short-circuit current value. On the other hand, there is no effect on the open-circuit voltage.

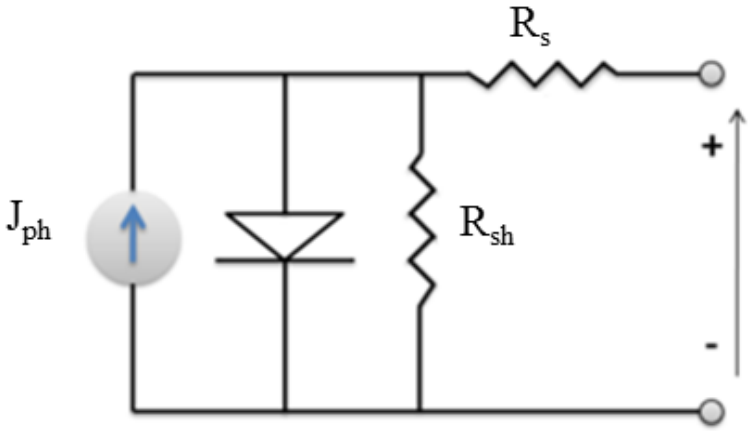

Figure 2. 12 The schematic diagram of a solar cell with R_s and R_{sh}

Figure 2.12 illustrates the schematic diagram of a solar cell with series resistance and shunt resistance (R_{sh}). As seen from the figure, low shunt resistance leads to occurring an alternative path for the light-generated current and this situation causes the losses of power in solar cell. Hence, the current loss due to shunt resistance also affects the performance of the device. In addition, for an effective solar cell, R_s value must be low and R_{sh} value high enough.

CHAPTER 3

EXPERIMENTAL TECHNIQUES

3.1 Introduction

This part mainly aims to supply the information about the techniques and methods which were used during both deposition and characterization steps. Firstly, the physical vapour deposition (PVD) techniques are introduced. The multi-source thermal evaporation system which is used during the deposition of CZTSe thin films is detailed. Then the structural, optical and the electrical characterization techniques of CZTSe thin films and the systems that are used for this concern are introduced. Finally, the techniques and the systems for the device analysis are explained.

3.2 Physical Vapour Deposition Techniques

Physical vapor deposition (PVD) is a deposition that involves evaporation and condensation of a material. Atoms or molecules of a material are vaporized from a solid source then transported in the form of a vapor through a vacuum or low-pressure gaseous environment, and condense on a substrate. This technique is generally used for high melting point and low vapor pressure materials. And, very large number of inorganic materials, metals, alloys, compounds, and some organic materials could be deposited with this technique. There are several PVD techniques such as; magnetron sputtering, cathode arc deposition, ion implanting, electron-beam evaporation, pulsed laser deposition and thermal evaporation methods. Also, they are an environmental process that can reduce the amount of toxic substances that must be disposed of with more conventional types of coating that involve fluid precursors and chemical reactions.

3.2.1 Thermal Evaporation Method

Thermal evaporation method can be considered as a resistive heating method which is performed at high temperature and low vacuum. The low vacuum enables to decrease the contaminations. The deposition sources are kept in boats. Vaksis Midas Coating System which is the multi-source thermal evaporation system was used during the deposition CZTSe thin films. The vacuum could reach around 10^{-7} *Torr* and the system can be controlled with a special control program during the deposition. The schematic illustrations of the system and the chamber are given in Figure 3.1 where the system is composed of chamber, control unit, mechanical and turbo pumps.

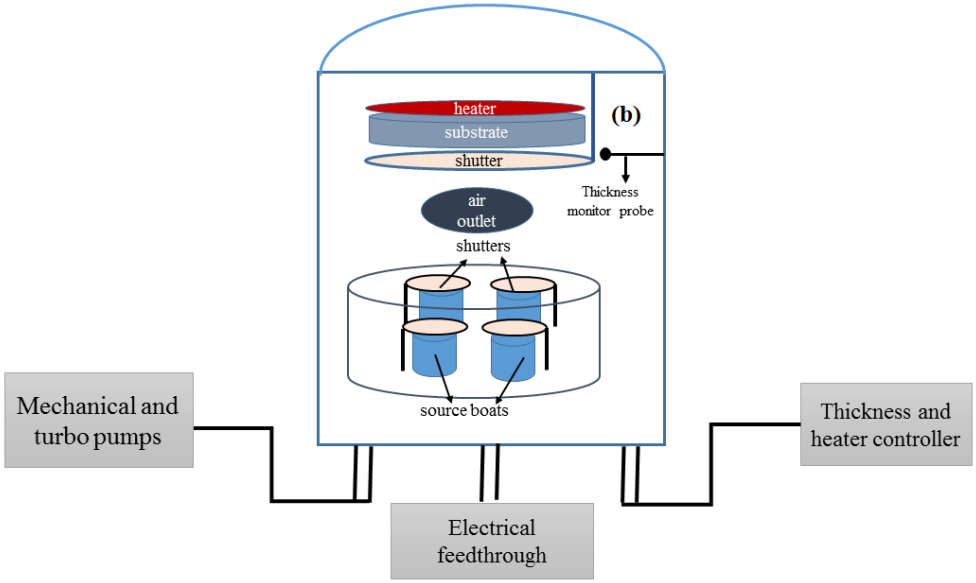

Figure 3.1 The schematic illustration of multi-source thermal evaporation system(a) and the chamber of the system(b)

There are four source and a substrate unit in the chamber, and each source is controllable separately. Hence, the deposition process could be controlled more precisely. Source units have Radak furnaces and they are composed of quartz and alumina crucibles covered with tantalum and molybdenum wires. The sources are heated with the help of these wires by the source power unit system. The thickness of the film is controlled by the thickness monitor.

During the deposition, substrates can be heated up to 800 ^{0}C with the heater unit just above the substrate unit. Moreover, the substrate unit is also able to be rotated during the deposition.

3.3 Structural Characterization

3.3.1 X-ray Diffraction (XRD)

X-ray diffraction (XRD) measurement is a non-destructive technique for identification and quantitative determination of the crystal structure. It also gives an information about the orientations and average grain sizes with the help of the Scherrer Formula [64]. Therefore, XRD measurements and analysis play a key role for the characterization of the structural properties of the materials. XRD characterization technique is based on the unique characteristic patterns that belong to each solid material in the crystalline structure. So these patterns are used to identify the structural properties of the materials. For the application of XRD technique, X-ray spectra is generally chosen to be close to order of the magnitude of the shortest interatomic distance which is about 0.5 and 2.5 Å [65]. The corresponding energy of these region is nearly 100 eV to 10Mev.

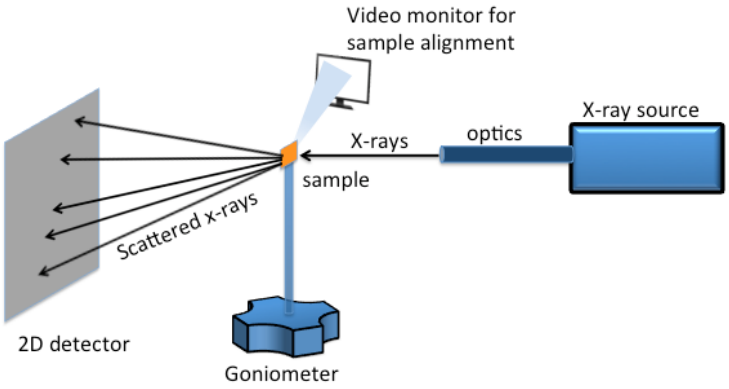

Figure 3.2 Schematic illustration of basic XRD system setup (adopted from ref[66])

The schematic illustration of the XRD system is given in Figure 3.2. In the system, there is an X-ray tube is a simple electrical device which is typically containing two

principle elements: an anode and cathode. Once the electrical current flows through the tube from cathode to anode, the electrons undergo an energy loss, which leads to the generation of X-radiation. In fact, this radiation could not be acquired in a specific direction and a unique wavelength. It generally has different wavelengths having different intensities. The wavelengths depend on both the voltage of tubes and the type of the anode such as Mo, W or Cr. Among them $K\alpha$ lines are generally used in the XRD systems due to having almost monochromatic radiation.

The monochromatic X-ray beams direct to the surface of the material then the reflected beams are analyzed. By the incident on the material of X-ray beams, they hit the atoms and the electrons around the atoms start to oscillate with the same frequency as incoming beams. The interaction of the incident rays with the material could produce constructive and destructive interferences. This interaction is shown schematically in Figure 3.3. When the material is in crystal structure, the constructive interface is occurred. This means that atoms are arranged in an ordinary pattern in the material. This condition satisfies Bragg 'Law that is expressed as;

$$n\lambda = 2dsin(\Theta) \tag{3.1}$$

Where, n is the integer that belongs to order of reflection.

This law associates with the wavelength of electromagnetic radiation to the diffraction angle and the lattice spacing in a sample. These diffracted X-rays from the sample are detected. Conversion of the diffraction peaks to *d*-spacings allows identification of the material. Typically, this is obtained by comparison of *d*-spacings with standard reference patterns [67].

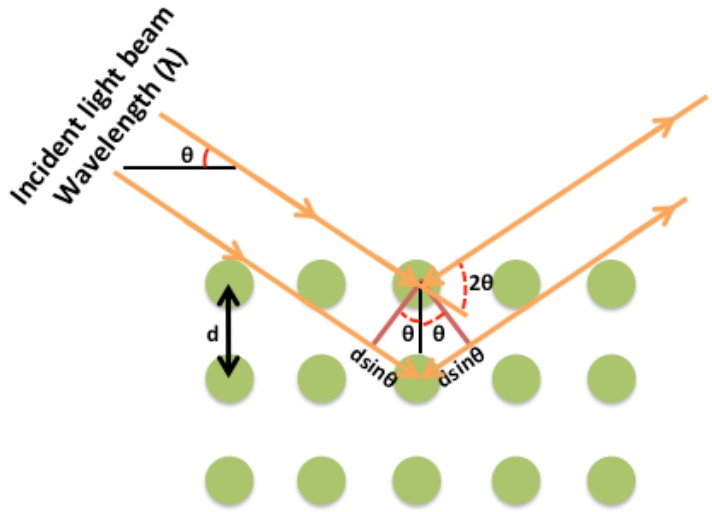

Figure 3.3 Schematic description of Bragg's Diffraction Law (adopted from Ref[66])

During this study, "Rigaku Miniflex XRD system equipped with CuKα X-ray source (λ=1.504 Å)" was used to analyze the structural properties of CZTSe thin films. The detailed information about the system is could be found in Ref [68]. The obtained data were analyzed with the software program by Rigaku. The obtained XRD patterns were compared with the literature and the International Centre for Diffraction Data (ICDD) to identify the structural properties of CZTSe tin films.

3.3.2 Raman Spectroscopy

Raman spectroscopy is a non-destructive vibrational spectroscopic technique that is used to provide information on molecular vibrations and crystal structures. In this technique, a laser light is used as a light source for the irradiation a sample, and generates an infinitesimal amount of Raman scattered light, which is detected as a Raman spectrum using a cooled charge-coupled device (CCD) camera as illustrated in Figure 3.4. Raman effect originates from the interaction of rotational and/or vibrational motions of molecules in the material due to the electromagnetic radiation [69] and it depends on a change in the frequency of incident photons after inelastic interaction with material. The inelastic interaction of incident photons with longitudinal and/or transverse modes of phonon is used to analyze the structure of the local atomic bonding

in this technique. Hence, Raman spectroscopy is a powerful technique to identify the material and to qualify the phase [67].

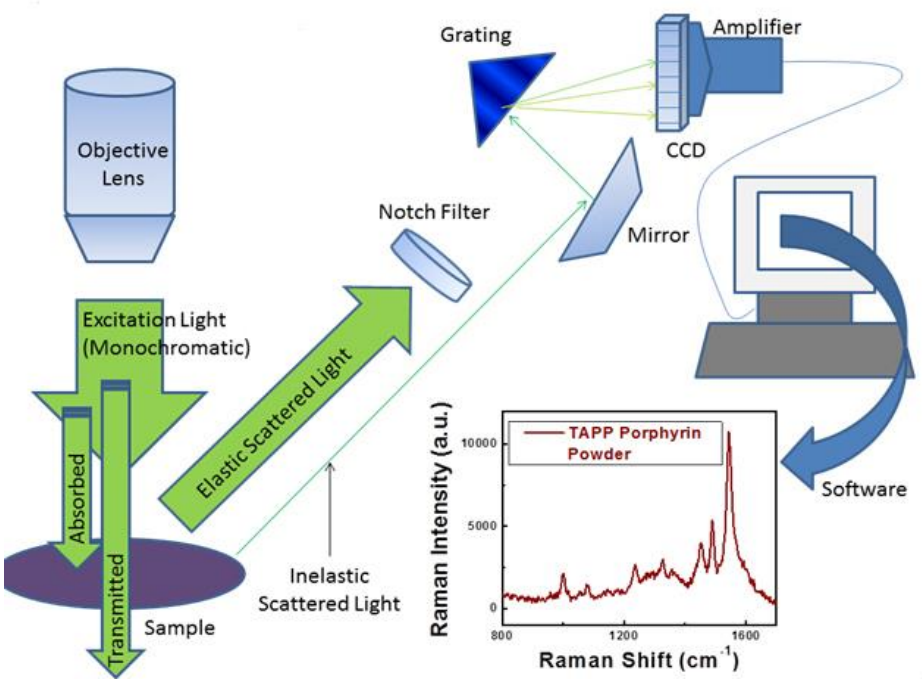

Figure 3.4 Schematic representation of Raman Spectroscopy system (adopted from Ref[70])

In thesis, Horiba-Jobin Yvon i550 Raman system equipped with Peltier CCD camera with 1cm^{-1} resolution was used for Raman spectroscopy measurements of CZTSe thin films. During the measurements, a 532 nm green laser (Nd:YAG) as a monochromatic light excitation source was used at room temperature.

3.3.3 Scanning Electron Microscopy (SEM)

Scanning electron microscope (SEM) is a type of electron microscope that is used for the studying the surface of objects. It utilizes a beam of focused electrons that is highly-energetic. The effect of the electron beam stimulates emission of backscattered highly-energetic electrons and lowly-energetic secondary electrons from the surface of the

material. The signals, occurred by the emission of the electrons, are collected and imaged with a CCD camera at high vacuum conditions. Hence the information about the morphology and the surface topology of the materials could be obtained with these micro-images.

The SEM system is shown in Figure 3.5 and the system is composed of electron gun, sample chamber, and the detectors. Electron gun is the source of the electron beam. The beam is focused and controlled by using electron lenses.

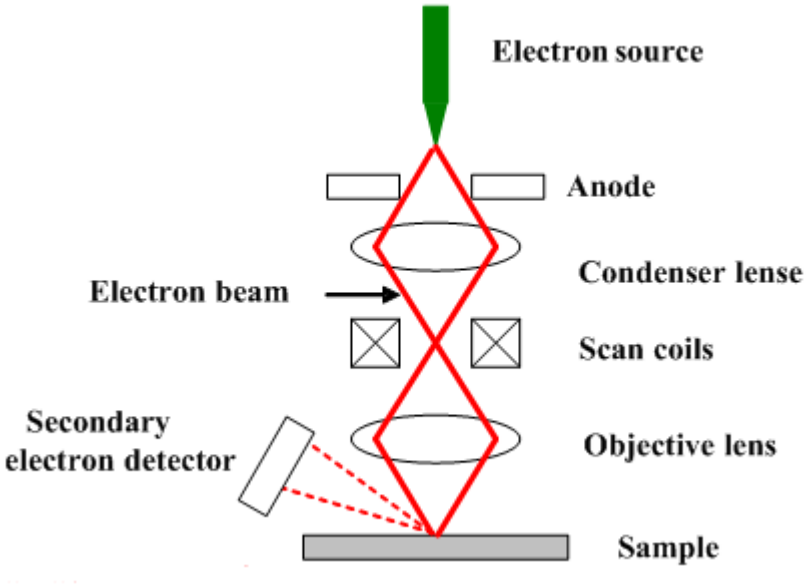

Figure 3.5 Schematic representation for SEM (adopted from Ref [71])

Sample chamber is a region where the material is placed and it supplies the interaction between material and the beam. Detectors serve to detect specific signals coming from the sample [73].

In this thesis, FEI Quanta 400 FEG model Scanning Electron Microscopy System was used to obtain SEM micro-images of CZTSe thin films.

3.3.4 Energy Dispersive X-ray Analysis (EDXA)

Energy Dispersive X-ray Analysis (EDXA) is an effective tool for the chemical analysis of materials which is used in generally conjunction with SEM. In order to analyze the elemental composition, EDXA detects X-rays emitted from the material during bombardment with an electron beam. This technique enable to characterize features or phases as small as 1 μm or less. Once the electron beam bombards the sample, electrons are ejected from the atoms comprising the sample's surface. The resulting electron vacancies are filled by electrons from a higher state, and an X-ray is emitted to balance the energy difference between the two electrons' states. The X-ray energy is characteristic of the element from which it was emitted.

In this thesis, FEI Quanta 400 FEG model SEM with EDXA system is used to analyze the composition of CZTSe thin films.

3.3.5 Atomic Force Microscopy (AFM)

Atomic Force Microcopy (AFM) measurement provides an opportunity to high resolution imaging with the feeling the surface of the material by using a mechanical probing as schematically shown in Figure 3.6. AFM also supplies 3D surface analysis with having any requirement on sample preparation before the measurement. This technique is based on a scanning the surface with a sharp tip while utilizing a small constant force. The motion of scanning is controlled with a piezoelectric tube scanner. Then the interaction between the and the surface of the film is monitored by reflection of laser beam from back side of the cantilever into a split photodiode detector. Finally, the AFM image of the material is got by as a change in the photodetector output voltage.

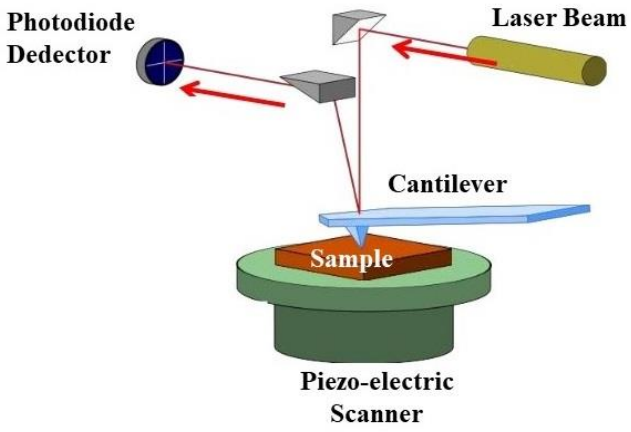

Figure 3.6 Schematic representation of AFM (adopted from Ref[72])

In this study, AFM measurement were carried out with Nanomagnetic ambient AFM system was used. The detailed information about the system could be found in Ref [68].

3.4 Optical Characterization

3.4.1 Transmission Measurements

The optical transmission spectrum shown in Figure 3.7, is a very useful tool to characterization of the optical properties of the materials. The information such as band structure, absorption coefficient, and impurity or trap levels of materials can be obtained by the optical transmission spectrum. In this technique, a monochromator as a light source and detectors to measure transmitted light are used. Incident light is transmitted from the sample and then it is measured as a function of wavelength based on the sample properties such as thickness, refractive index, extinction coefficient and absorption coefficient. Transmittance of the sample can be basically defined as the ratio of the incident and the transmitted light intensities [75].

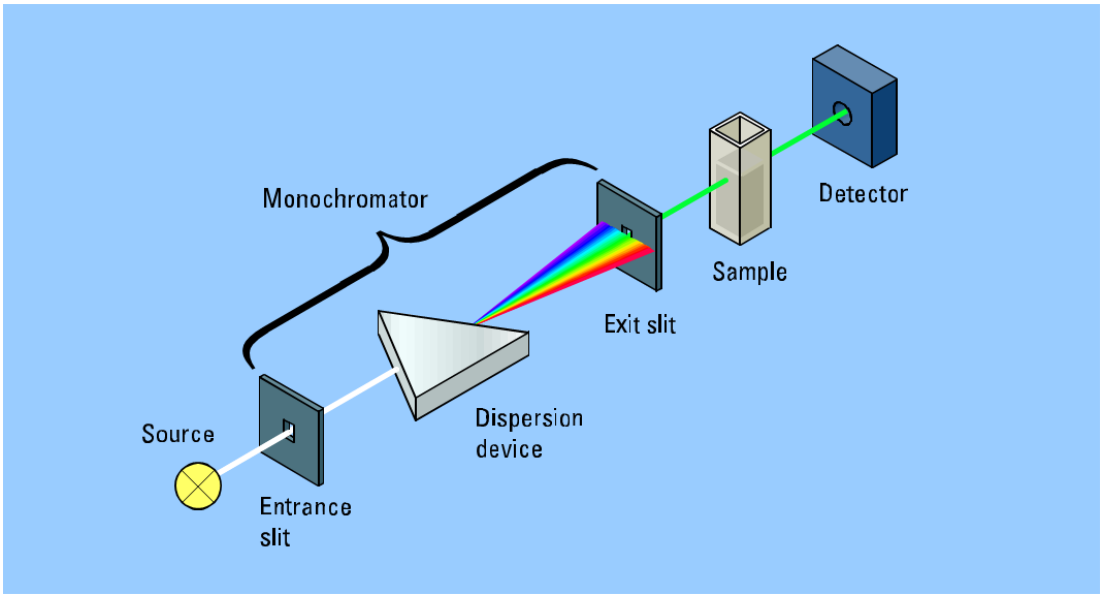

Figure 3.7 Schematic represantation of UV/Vis/NIR spectrophotometer(adopted from Ref[73])

In this study, Perkin-Elmer Lambda 950 UV/Vis/NIR spectrophotometer was used to carry out the optical transmission measurements for CZTSe thin films. By using the spectra obtained with these measurements were used to characterize the optical properties of CZTSe thin films.

3.5 Electrical Characterization

3.5.1 Temperature Dependent Photoconductivity

The temperature dependent photoconductivity of deposited CZTSe thin films was investigated in the temperature range of 100-350 K by using Janis Liquid Nitrogen VPF Series Cryostat. Vacuum was created with Univac Rotary pump and a LakeShore-331 temperature controller were used to controll temperature of the samples inside the cryostat. The temperature of sample was step by step increased from 100 K to 350 K. The halogen lamp (12 Watt) was used to illuminate the samples. The lamp is located at a suitable place just above the sample to provide fixed illumination of the whole surface uniformly. The illumination intensities of the halogen lamp were set in terms

of varrying light intensities by changing with Keithley 220 programmable current source. Additionally, the intensities of halogen lamp illumination intensities were determined by an IL Ford 1700 radiometer. Keithley 2401 multimeter was used to apply bias voltages and measure current. Besides, all devices in measurements were controlled by using LabVIEW software program.

3.5.2. Hall Effect Measurement

Hall Effect measurement is an another key technique to determine the electrical properties of materials. The basic physical principle of the Hall effect is the Lorentz force, which is a combination the electric and the magnetic force.

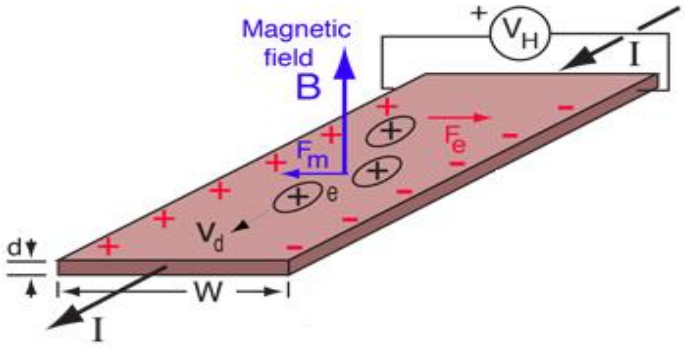

Figure 3.8 Schematic view of Hall effect (adopted fromRef [74])

The schematic representation of Hall effect is shown in Figure 3.8. Once a current carrying material is placed inside a magnetic field which is perpendicular to the direction of current flow, the charges will be deflected due to the Lorentz force. Then, these charges built up an electric field and the electric field results in the accumulated charges at the surface. The builted up electric field is called the Hall field and the type of carriers determine the direction of this field.

In this study, the Hall Effect measurements were carried out at room temperature with tHall Effect set-up and the magnetic field produced by Walker Magnion Model FFD-4D electromagnet which was controlled a with special software program. CZTSe thin film samples were prepared as van der Pauw geometry[68].

3.5.3 Current-Voltage Measurements

In order to state the device characteristics of the fabricated devices, current-voltage (I-V) measurements under both dark and illuminated conditions were carried out. These measurements were performed at the varying temperature range. During the measurements, Keithley 2401 source meter which was controlled by a Labview PC program was used. The measurements under illumination condition were carried out at AM 1.5 condition.

The temperature dependencies of I-V measurements were performed by using The Model 22 CTI Cryogenics closed-cycle helium refrigeration system. In addition, temperature was controlled by LakeShore DRC-91C temperature controller.

3.5.4. Capacitance-Voltage Measurements

The capacitance-voltage (C-V) measurements at room temperature were carried out as an another technique to characterize the device properties. C-V measurements were perfomed with the computer-controlled measurement set-up and Hewlett Packard 4192A LF model impedance analyzer. The voltage interval was selected depending on the electrical properties of the samples, and the built-in frequency can be chosen within the limits of the analyzer which is between 5 Hz and 13 MHz [69]. Moreover, the impedance analyzer can perform with oscillation level from 5 mV to 1.1 Vrms and the oscillation level step for this equipment is 1 mV in 5-100 mV regions and 5 mV in 100 mV-1.1 V region. The range of internal dc bias voltage source is between -35 V to +35 V with 10 mV step precision.

CHAPTER 4

DEPOSITION AND CHARACTERIZATION OF CZTSe THIN FILMS

4.1 Introduction

This part introduces the determination of the physical properties of the CZTSe thin films and optimization procedures. CZTSe quaternary compounds have been deposited by thermal evaporation method and annealing processes have been applied to get desired film properties. Three different set of processes have been carried out (CZTSe-1, CZTSe-2, and CZTSe-3). At first, different deposition processes were introduced in detail. Then the film properties were determined as a result of structural, optical and electrical characterization by means of different experimental methods. CZTSe films were analyzed in terms of their compositional, morphological, structural, optical and electrical properties.

4.2 CZTSe-1 Thin Films

4.2.1 Experimental Details

CZTSe-1 thin films were deposited by thermal evaporation method sequentially from the pure elemental sources onto well cleaned soda lime glasses in a stacked layer form. The schematic diagram for the deposition and annealing processes are given in Figure 4.1.

Deposition was carried out in 12 layers as Zn/Se/Sn/Se/Cu/Se/Zn/Se/Sn/Se/Cu/Se and substrate temperature was kept at about room temperature and the vacuum was controlled at about 10^{-6} Torr. Thickness of each film layer was deposited and measured by Inficon Quartz thickness monitor during deposition as about 30 nm, 50 nm, 30 nm,

and 60 nm for Sn, Se, Cu and Zn layers, respectively. Then, different annealing procedures were applied both in-situ and after the deposition.

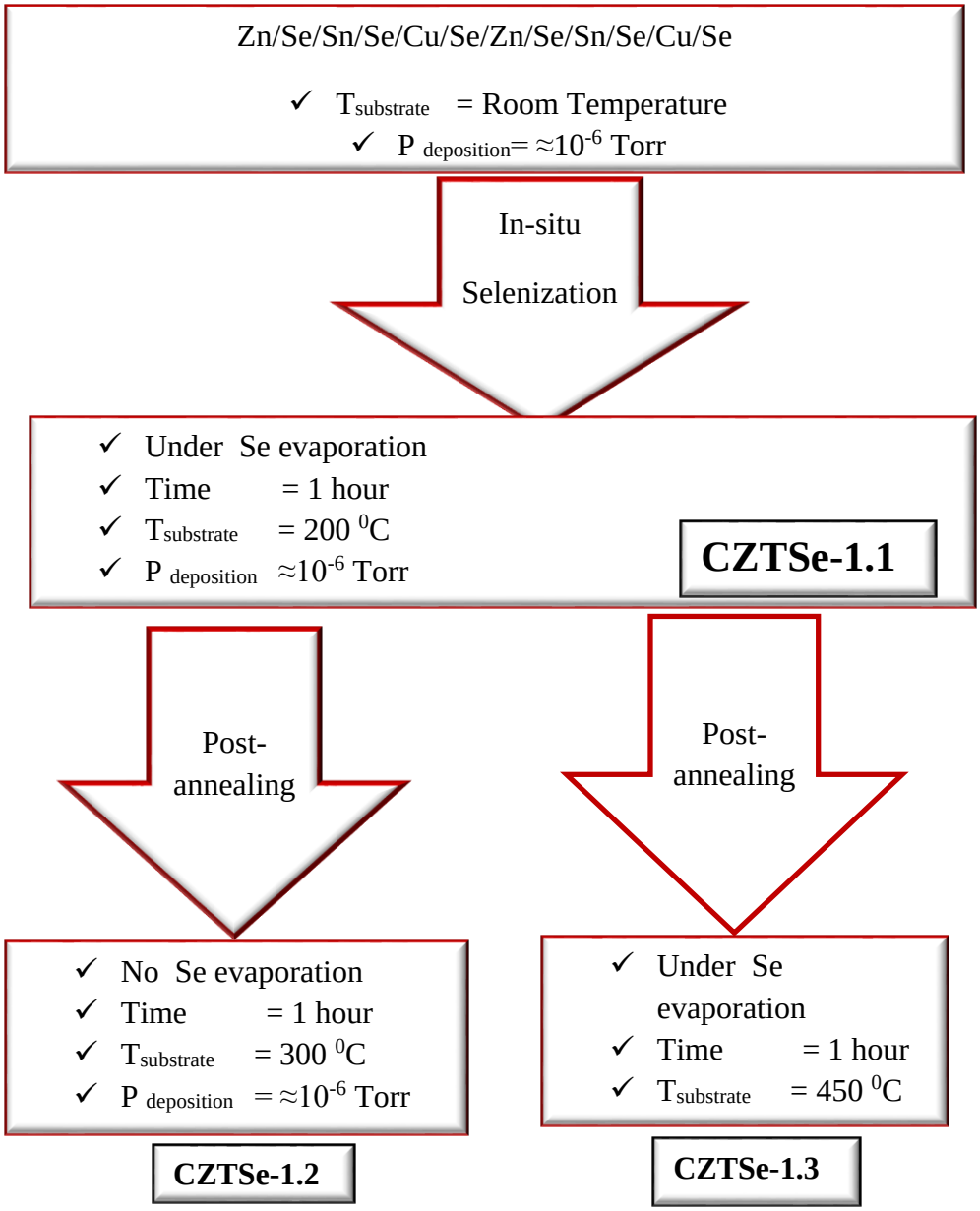

Figure 4.1 Schematic diagram of deposition and annealing processes for CZTSe-1 thin films

Firstly, just after the deposition of stacked layers, the substrate temperature was upgraded to 200 °C under the pressure of 10^{-6} Torr with Se evaporation. Then, CZTSe thin films were annealed for one hour at this condition (CZTSe-1.1). After deposition, three sample sets were prepared; one of them was kept in as-grown form(CZTSe-1.1), another set was annealed for an hour at 300 °C under vacuum condition (CZTSe-1.2) and the other one was annealed for an hour at 450 °C under Se environment (CZTSe-1.3). Thickness of the films was determined by Dektak 6M thickness profilometer as about 600 nm. The structural and the morphological evolution were analysed by means of X-ray diffraction (XRD), Raman spectroscopy, energy dispersive X-ray spectroscopy (EDS) and scanning electron microscopy (SEM). Moreover, transmission measurements were performed to determine the optical characteristics of these samples. In addition, the electrical and photoelectrical properties of the films have been investigated by carrying out temperature dependent conductivity, photoconductivity under different illumination intensities in the temperature range 100–400 K.

4.2.2 Results and Discussions

4.2.2.1 Structural Characterization of CZTSe-1 Thin Films

The EDS results for CZTSe-1.1, CZTSe-1.2, and CZTSe-1.3 are listed in Table 1 As seen from Table-1, all films are Se-rich and Cu –poor nature. Applying different annealing processes affects the composition of the film. Accroding to EDS results given in Table 4.1, it could be inferred that annealing process resulted decrease in Se composition of the CZTSe-1.3 as compared with the values with the CZTSe-1.1. Therefore, the compositions of the annealed films show that there is a considerable decrease in the Se and with annealing possibly due to the high volatility of Se element and an increase in the re-evaporation probability of mobile Se atoms with annealing before making the bond to construct the crystalline structure. It also can be deduced

that, CZTSe-1 thin films are not stoichiometric due to the chemical formula of kesterite structure.

Table 4-1EDS results of CZTSe-1.1, CZTSe-1.2 and CZTSe-1.3 thin films

Sample	Chemical Compositions (at %)				Ratio of Compositions		
	Cu	Zn	Sn	Se	Cu/(Zn+Sn)	Zn/Sn	Se/(Cu+Zn+Sn)
CZTSe-1.1	2	6	9	83	0.2	0.7	4.9
CZTSe-1.2	3	8	8	81	0.2	1.0	4.3
CZTSe-1.3	4	11	17	68	0.1	0.7	2.1

The SEM microphotographs of the CZTSe-1 films are given in Figure 4.2. As seen from the figure, there is a remarkable change in the film morphology by the annealing processes. The re-evaporation Se atoms with annealing could be responsible for the change in the film morphology observed in SEM micrographs.

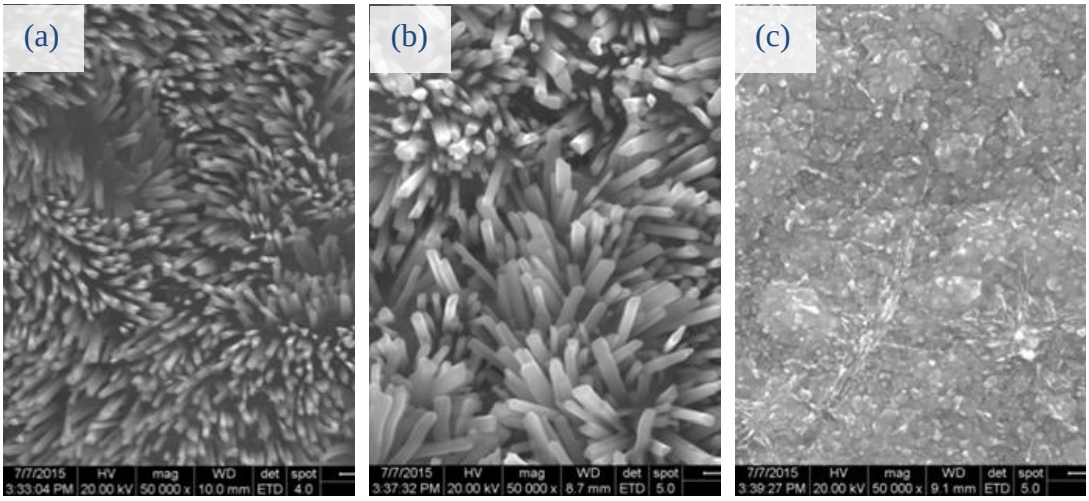

Figure 4.2 SEM image for (a) CZTSe-1.1, (b) CZTSe-1.2 and (c) CZTSe-1.3 thin films.

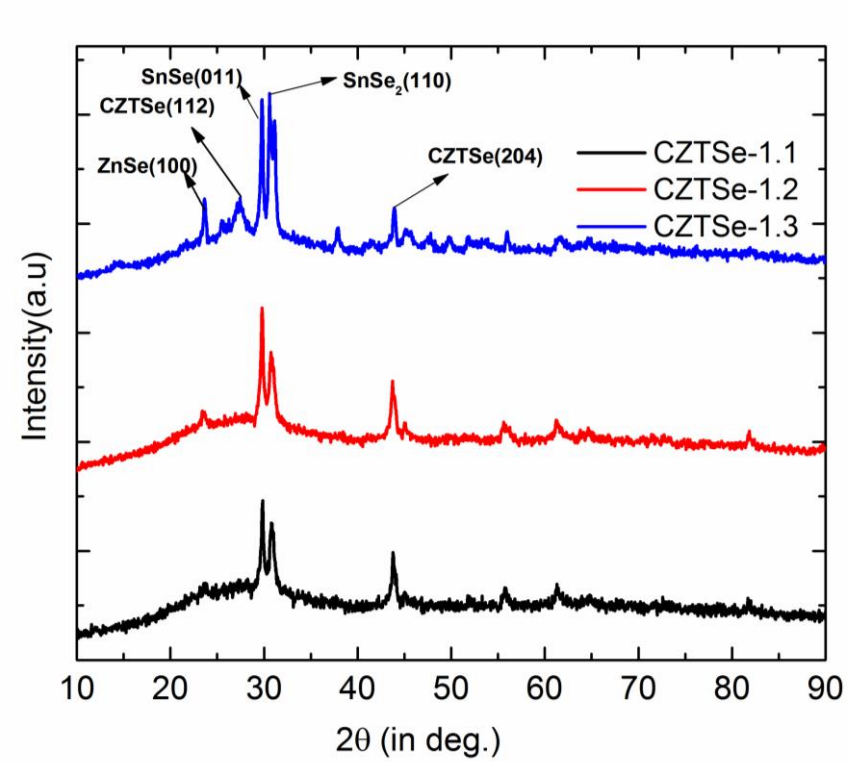

Figure 4.3 XRD patterns for CZTSe-1 thin films

The XRD measurements were carried out to get the information about the structure of CZTSe thin films and they are is given in Figure 4.3. When the XRD patterns were analyzed, the results showed that there is not a significant difference in between CZTSe-1.1 and CZTSe1-2 structures.

As seen from the figure, SnSe(011), $SnSe_2$(110) and CZTSe (204) phases were detected both in CZTSe1.1 and CZTSe1.2 thin films [75]. On the other hand, ZnSe (100) and CZTSe(112) phases were dedected in CZTSe-1.3 thin films structure[76]. XRD results indicate that CZTSe-1 films are not in kesterite structure which must have the preferred direction along (112) plane.

Raman measurements were carried out as a final measurement to verify the secondary phases of CZTSe-1 thin films. It is given in Figure 4.4.

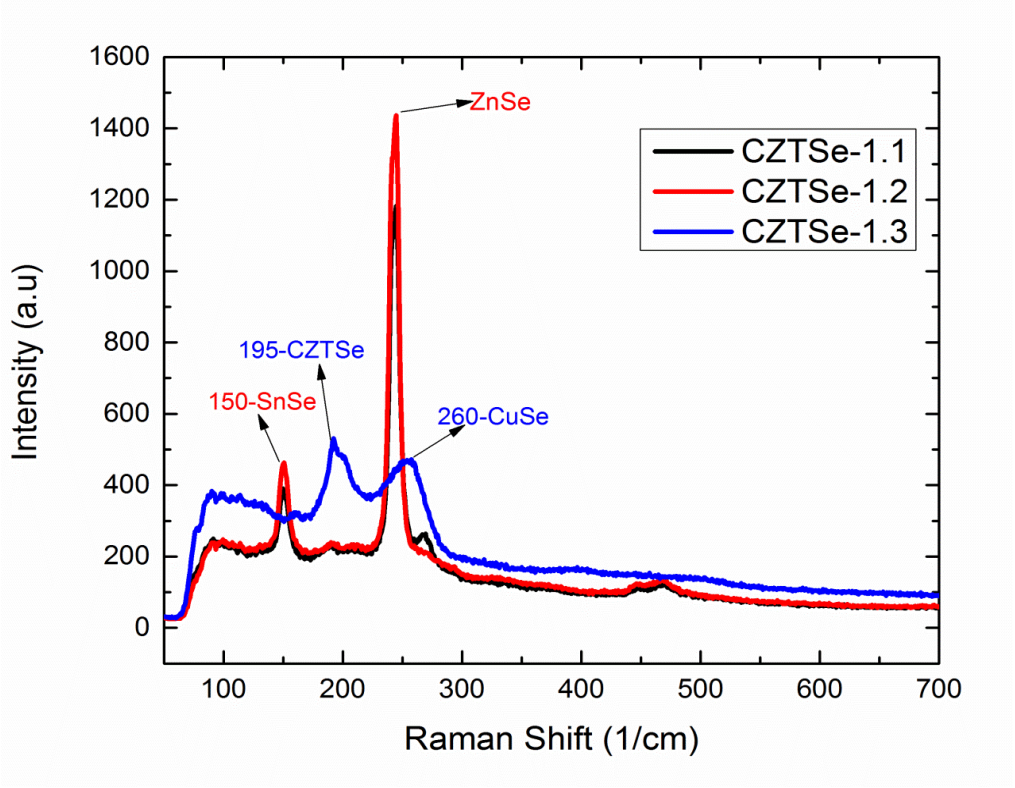

Figure 4.4 Raman Measurements for CZTSe-1 Thin Films

Raman shifts can be used as an identification of the crystalline phases. According to literature, Raman shifts at 150,195, 250 and 260 cm^{-1} belong to SnSe, CZTSe, ZnSe and CuSe respectively [77]–[79]. XRD and Raman measurements showed that CZTSe structure with Raman shift at 195 cm^{-1} was only observed in CZTSe1-3 thin film. Considering both XRD and Raman results, it could be deduced that CZTSe phase started to be observed with the annealing at 400^{o}C under Se evaporation.

4.2.2.2 Optical Characterization of CZTSe-1 Thin Films

In order to determine the optical properties of CZTSe-1 thin films, transmission measurements were carried out in the range of 200-1000 nm. The optical absorption coefficient was calculated from the spectral measurements of transmission and reflection by using the equation [80];

$$T = (1 - R)^2 \, e^{(-\alpha t)} \tag{4.1}$$

where, α is absorption coefficient, t is the thickness of the films. The band gap and the optical transition natures of each film depending on photon energy were evaluated using the expression;

$$(\alpha h\nu) = A(h\nu - Eg)^n \tag{4.2}$$

where A is constant, hν is the incident photon energy, E_g is the optical band gap and n is the power exponent that can take the values of 1/2, 3/2, or 2 due to whether the optical transition is direct-allowed, direct-forbidden or indirect-allowed, respectively. By using direct-allowed optical transitions, optical band gaps for each film were obtained from the extrapolation of the linear region of the plot $(\alpha h\nu)^2$ versus photon energy (hν). The direct band gap was obtained by extrapolating the straight line part of the curves for the plots of $(\alpha h\upsilon)^2$ versus hυ of the films as given in Figure 4.5.

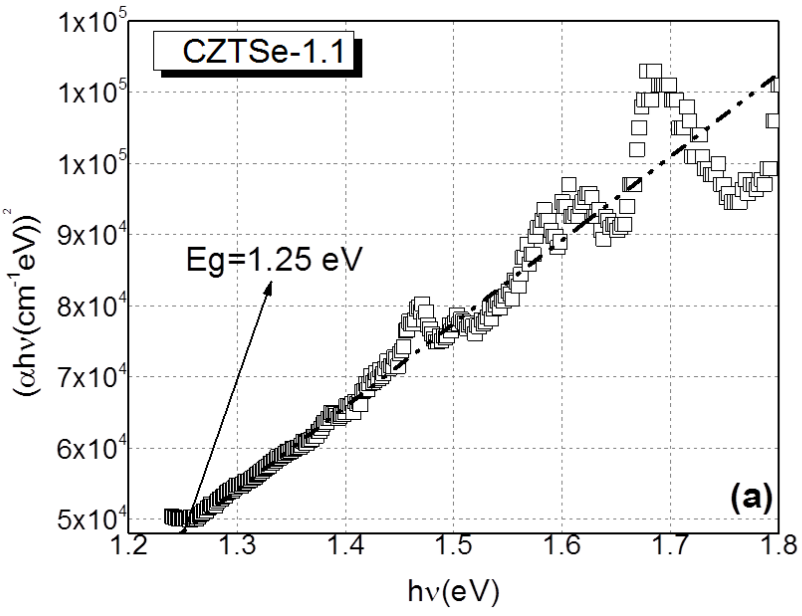

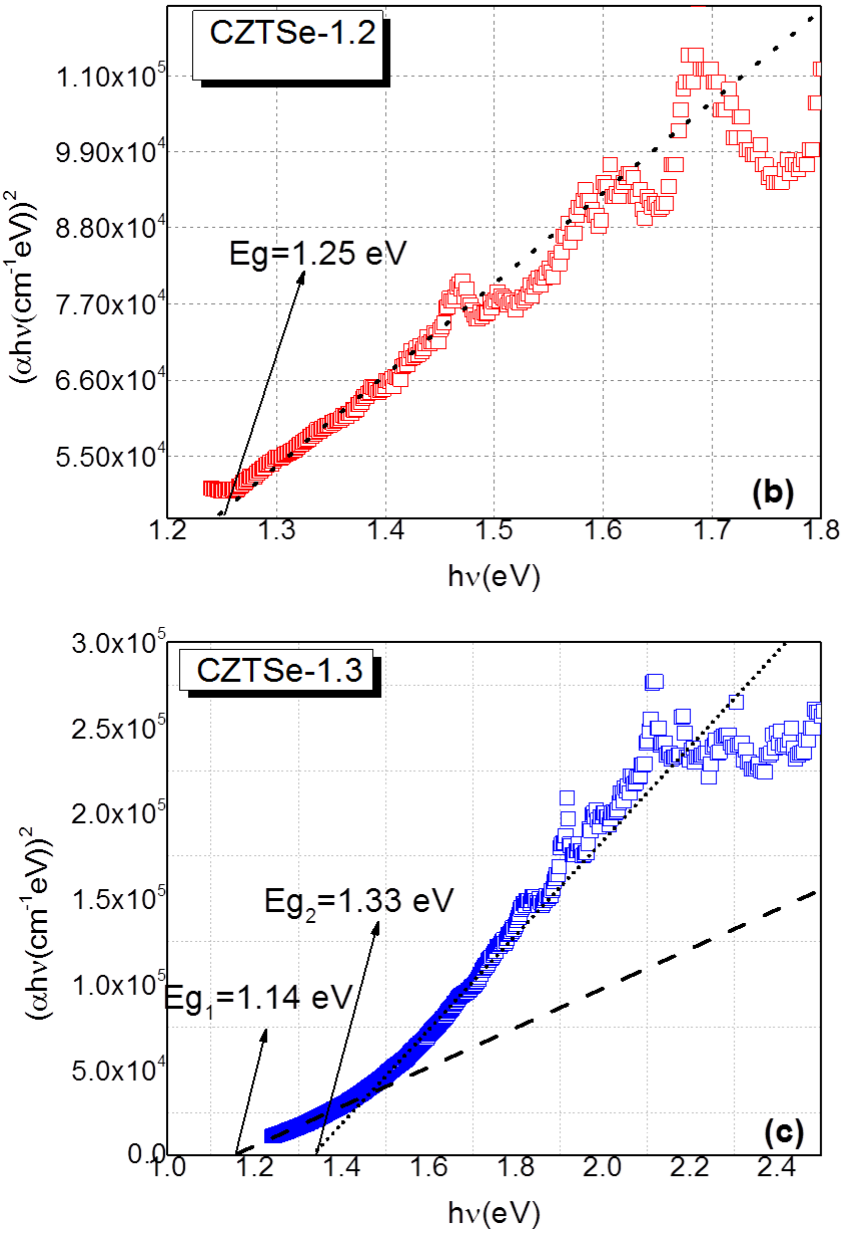

Figure 4.5 $(\alpha h\nu)^2$ vs hν graphs for (a) CZTSe-1.1, (b) CZTSe-1.2 and (c) CZTSe-1.3 thin films

The band gap was found as found 1.25 eV for both CZTSe-1.1 and CZTSe-1.2. On the other hand, there are two distinct band gap values for CZTSe-1.3. The films with higher Cu/(Zn+Sn) ratio are found to have higher optical band gap than the films with lower Cu/(Zn+Sn) ratio. It results from the lattice strain which was caused by the different Cu/(Zn+Sn) ratio of the thin films[79], [80]. As seen from Table 4.1 there is

a decrease in Cu/(Zn+Sn) ratio with annealing temperature(CZTSe-1.3). So this is the reason for the increase in the band gap value.

4.2.2.3 Electrical Characterization of CZTSe-1 Thin Films

Temperature dependent conductivity values for CZTSe thin film deposited in van der Pauw geometry were given in Figure 4.6 and the CZTSe thin film samples showed thermionic emission characteristics as a conductivity behavior in the temperature region of 200-300 K.

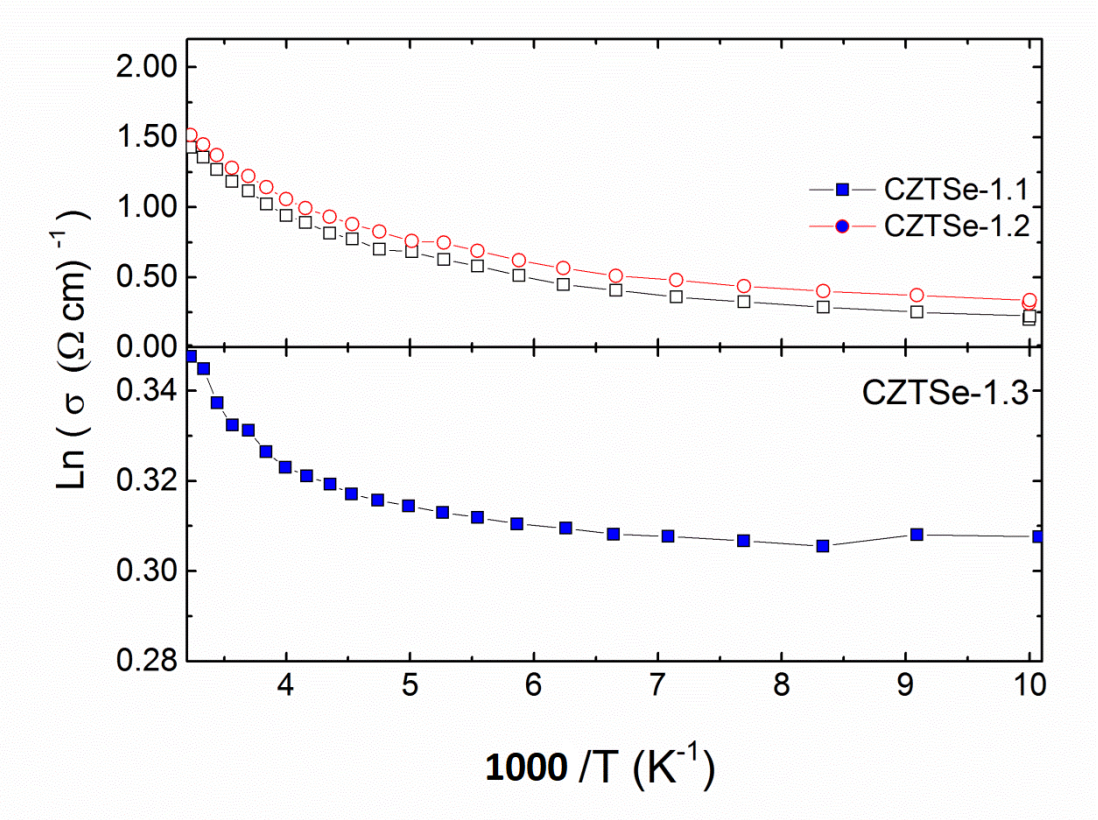

Figure 4.6 Temperature dependent conductivity measurements for CZTSe thin films.

In this temperature range, charge carriers are able to have energy to exceed conduction band and join conduction with the effect of temperature.

Thermionic emission can be analyzed by the equation [81]

$$\sigma_T = \sigma_{0T}\, exp\left[-\left(\frac{E_a}{kT} \right) \right] \tag{4.3}$$

where σ_{0T} is the pre-exponential factor, E_a is the activation energy, k is the Boltzmann constant and T is the absolute temperature. As observed from Figure 4.6, Ln (σ) versus (1000/T) plot shows a linear region in between the temperature range of 240-300 K for the films. The thermal activation energy for CZTSe samples in this temperature region was calculated from the slope of ln(σ_T)-1000/T plot. These values were about 470, 450 and 20 meV for CZTSe-1.1, CZTSe-1.2 and CZTSe-1.3 thin films respectively.

4.3 CZTSe-2 and CZTSe-3 Thin Films

The results of the deposition and the characterization of CZTSe-1 thin films indicated that CZTSe-1 thin films were non-stoichiometric. But then, the structural, optical and the electrical properties of the CZTSe-1 films pointed out that CZTSe phase started to be observed only in CZTSe1.3 thin film. In order to enhance the physical properties of CZTSe thin films, two different deposition processes were improved by considering the post annealing and selenization conditions which was applied to CZTSe1-3 thin film. The films deposited and characterized are labeled as CZTSe-2 and CZTSe-3 in this part.

4.3.1 Experimental Details

Highly pure Cu, Sn, Zn and Se elements kept in the individual thermal sources of the thermal evaporation system (Vaksis Midas) were deposited onto well cleaned soda lime glass substrates using layer by layer stacked layer growth technique. The optimization of the stack layer was analyzed by using different ordering, thicknesses and annealing processes. As a result of critical optimization study, the given stacking layer ordering was used to determine the influence of the layer order on the physical properties of the films, such as the variations of the secondary phases, two different

deposition approaches were carried out by the result of the optimization process. First, the deposition was started with very thin Se precursor layer proceeded as Sn/Se/Cu/Se/Zn/Se/Sn/Se/Cu/Se/Zn/Se (labeled as CZTSe-2). During the deposition, substrate temperature was kept at about room temperature and the pressure was controlled at about 10^{-6} Torr. Just after stacked layers' deposition, the substrate temperature was increased to 400 ^{o}C and in-situ annealing process was used under Se evaporation for an hour. Then, the substrate temperature was cooled down to room temperature slowly (labeled as asg. CZTSe-2). In order to determine the annealing effects on the film properties, annealing process was applied under nitrogen atmosphere at 450^{o}C for half an hour (labeled as anl. CZTSe-2).

For the second deposition cycle, all conditions were kept the same with the first one except the order of the stacked layers. In this case, the order of Sn layers was exchanged with Zn layers so it was in the form of Zn/Se/Cu/Se/Sn/Se/Zn/Se/Cu/Se/Sn/Se (labeled as CZTSe-3). In situ annealing at 400^{o}C under Se evaporation was applied immediately after the deposition of the stacked layers (labeled as asg. CZTSe-3). Then, the annealing procedure at 450^{o}C was carried out under nitrogen atmosphere as it was done in the first deposition cycle (labeled as anl. CZTSe-3).

CZTSe-2 and CZTSe-3 films were analyzed in terms of their compositional, morphological, structural, optical and electrical properties. Thickness of the films was determined by Dektak 6M thickness profilometer as about 700 nm. The compositional and morphological characterizations of the CZTSe samples were performed by means of an a JSM-6400 Scanning Electron Microscope (SEM), equipped with NORAN System 6 X-ray Microanalysis System and Semafore Digitizer detector operated at 25 kV. In order to analyze the structural properties of the CZTSe thin films, XRD measurements were examined by using Rigaku Miniflex XRD system with Cu Kα ($\lambda \approx 1.5459$ Å) radiation source. Raman analyses were carried out at room temperature using a Horiba-Jobin Yvon i550 system equipped with a CCD camera with 1 cm^{-1} resolution and a laser with the wavelength of 532 nm used as an excitation source. Reflection and transmission spectra of the films were measured by using the Lambda

45 UV/VIS/NIR Spectrophotometer in the wavelength of 300-900 nm to get the information about the optical properties of CZTSe thin films. The electrical properties of the films were determined by means of Keithley 2440 source measure unit and 220 current source, and the mobility measurements were carried out at 0.9 Tesla using Nanomagnetic Hall Effect system.

4.3.2 Results and Discussions

4.3.2.1 Structural Characterization of CZTSe-2 and CZTSe-3 Thin Films

In order to investigate the compositions and stoichiometry of as-grown and annealed thin films, EDS measurements were carried out and they are listed in Table 4.2.

Table 4-2 EDS results of CZTSe-2 and CZTSe-3 thin films

	Chemical Compositions (at%)				***Ratio of Compositions***		
Samples	*Cu*	*Zn*	*Sn*	*Se*	*Cu/(Zn+Sn)*	*Zn/Sn*	*Se/(Cu+Zn+Sn)*
asg. CZTSe-2	19	23	14	44	0.51	1.68	0.80
annl.CZTSe-2	15	21	13	51	0.45	1.67	1.02
asg. CZTSe-3	15	15	5	65	0.75	3.00	1.86
annl.CZTSe-3	28	26	9	37	0.80	2.89	0.59

The results show that both as-grown and annealed CZTSe-2 films have Cu poor and Zn rich composition, which is the desired condition to get high efficient solar cells based on CZTSe thin film [82]. On the other hand, it is noticed that there are Cu and Sn deficiencies as well as the small amount of excess Se in the composition of as-grown CZTSe-3 thin film. However, after the post annealing process, there is significant decrease in Se ratio in the composition of annealed CZTSe-3 sample, which can be attributed to the re-evaporation of Se from the film structure due to the high annealing temperature and vapor pressure.

In addition, copper ratio in annealed film reaches the expected ratio with the help of thermal annealing and the film is still in Zn rich condition as inferred from Table 4.2.

The SEM microphotographs of the CZTSe-2 and CZTSe-3 films are given in Figure 4.7. As seen from the figure, there is a remarkable change in the film morphology by the annealing processes.

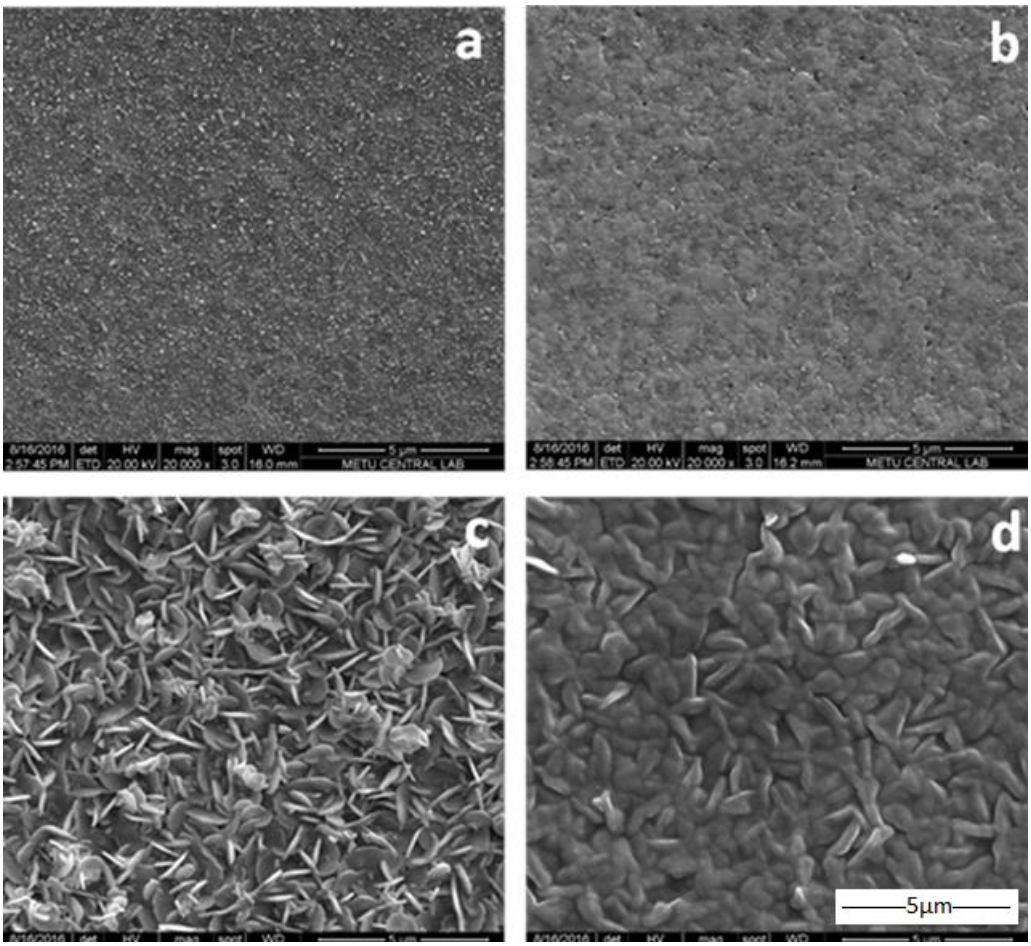

Figure 4.7SEM images of (a) asg.CZTSe-2 (b) annl.CZTSe-2, (c) asg.CZTSe-3, (d) annl.CZTSe-3thin films.

Figure 4.7 (a) shows agglomerated small grains on the surface of the asg. CZTSe-2 film. However, there are some voids on the surface of annl. CZTSe-2 film, which may result of the re-evaporation of some volatile compounds from the surface at the

elevated temperature, as shown in Figure 4.7 (b). On the other hand, the agglomerated grains show the platelet shape in the SEM image of asg. CZTSe-3 film (Figure 4.7 (c)). This might be attributed to the formation of ternary Cu_2SnSe_3 on the as-grown sample as the secondary phase since the similar SEM image of Cu_2SnSe_3 compound was reported in Ref[83].

The topographic properties of the deposited CZTSe films were investigated by using AFM measurements and the observed topographic images are shown in Figure 4.8 The obtained root-mean-square (RMS) surface roughness value was 28.8 and 45.9 nm for as-grown films. Applying annealing process change the surface morphology and as a result the RMS peak to peak values became 20.9 and 42.6 nm for for CZTSe-2 and CZTSe-3 film samples, respectively.

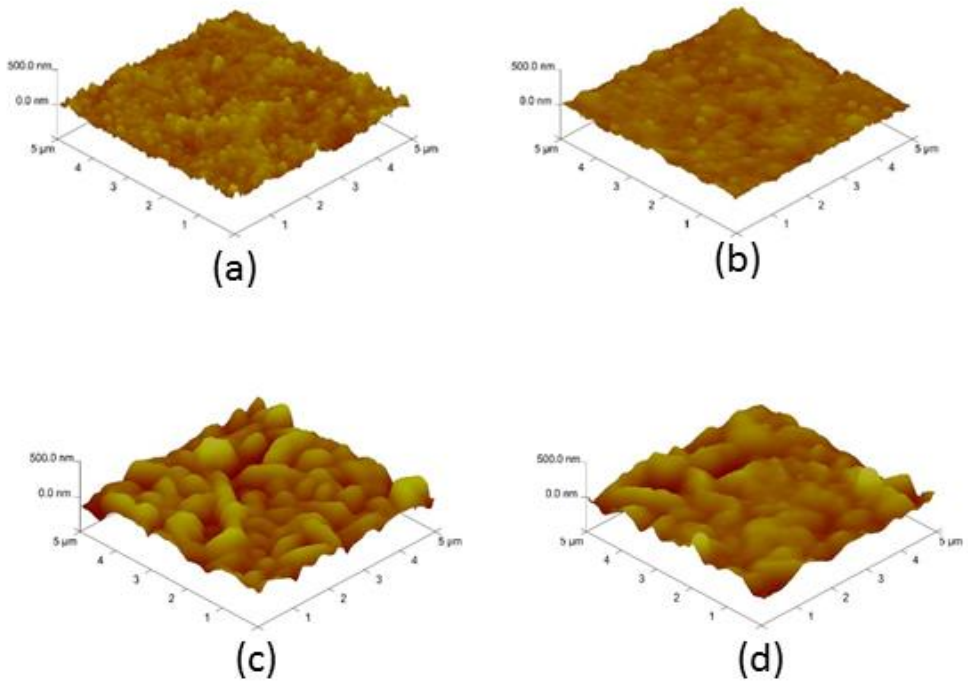

Figure 4.8: AFM images of (a) asgrown CZTSe-2 (b) annealed CZTSe-2, (c) asgrown CZTSe-3, (d) annealed CZTSe-3 thin films

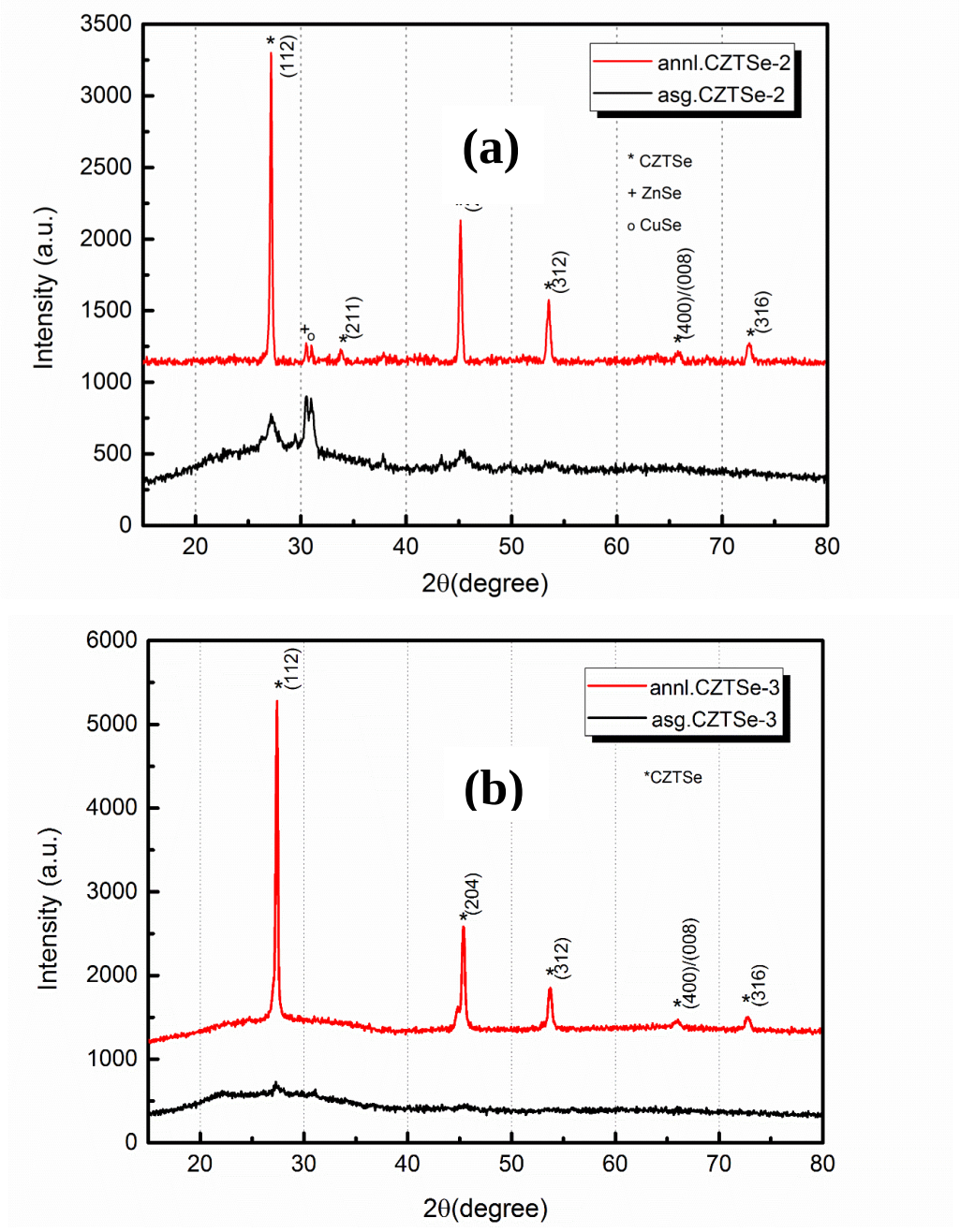

Figure 4.9 XRD patterns for (a) CZTSe-2 and (b) CZTSe-3 Thin Films

X-ray diffraction (XRD) patterns of all samples are shown in Figure 4.9. It is observed that XRD patterns of the grown samples with different precursor order are far from the expected diffraction peaks of CZTSe structure. However, the diffraction peaks for both annealed samples are corresponding to Kesterite CZTSe structure with respect to International Center for Diffraction Data (ICDD) (card no: 04-010-6295)[84]. The

main orientation labeled as (112) plane of the annealed samples was fitted with the Gaussian and Lorentzian functions to find the full width at half maximum (FWHM) value, clearly. Then, crystallite size was calculated using Scherrer's formula [85]

$$d = \frac{0.9\lambda}{\beta \cos\theta} \tag{4.4}$$

where β is the full width half maximum (FWHM) value, θ is the Bragg angle and λ is the wavelength of the X-ray radiation source. FWHM of annealed CZTSe-2 film is smaller than that of annealed CZTSe-3 film and grain sizes were calculated as 39.6 and 36.6 nm, respectively, presented in Table 4.3 These values are comparable to each other and there is no significant difference.

Table 4-3 XRD analysis results of CZTSe-2 and CZTSe-3 thin films

	annl. CZTSe-2	***annl. CZTSe-3***
FWHM (degree)	0.212	0.226
Peak Position (in degree)	27.16	27.37
Crystallite size (nm)	39.6	36.6

From the XRD analysis, the lattice constants of CZTSe film were calculated as a=5.700Å and c=11.390Å. These values are consistent with the reported values of a=5.683Å and c= 11.335Å [86]

Figure 4.9 (a) also shows the presence of secondary phase in the XRD pattern of annealed CZTSe-2 thin film. These peaks can be attributed to ZnSe and CuSe, as reported in Ref.[87]. On the other hand, any peaks indicating the existence of secondary phases for annealed CZTSe_2 thin film were not detected. However, it is difficult to identify the secondary phases of CZTSe using only XRD measurement [82].

In order to be sure about the secondary phases, Raman measurements were also carried out with the excitation wavelength of 532 nm. In Figure 4.10, the Raman spectrum of the asgrown CZTSe-2 has two broad peaks centered at 240 and 260cm^{-1}, which are the characteristic modes of elementary selenium and Cu_2Se [87]–[89] , respectively. Presence of elementary Se peak in the Raman spectra may be explained by the selenium aggregation at the surface of the film. This requires the substrate temperature during selenization process to be higher than 400^oC or post-annealing process should be implemented to obtain uniform CZTSe thin film. As shown in Figure 4.10, after the post annealing under nitrogen, three peaks centered at 173, 196 and 233cm^{-1} are the specific CZTSe phases as observed by Fairbrother et. al. [7]. Moreover, the weak peak at 250cm^{-1} is attributed to ZnSe as the secondary phase [7]. After annealing, the disappearance of elementary selenium peak in the Raman spectrum may be explained by Se diffusion into the bulk region as a result of thermal energy provided by annealing. EDS results justify this explanation since there is an increase in Se ratio in the composition of annealed CZTSe-2 samples. Therefore, the results of EDS measurement and Raman spectroscopy are consistent with each other. On the other hand, the weak peak at 180 cm^{-1} was detected in the Raman spectra of the as-grown CZTSe-3 thin films sample. It can be attributed to Cu_2SnSe_3 phase [90]. After the post annealing, the peaks observed at 173, 196 and 233 cm^{-1} in the Raman spectra are implying that CZTSe phase become dominant in the structure together with the weak peak centered at 250cm^{-1}. The most intense peak in the Raman spectra of CZTSe thin film results from the vibration of Se atoms and it is called as A_1 mode [84], [91].

In order to perform more detailed Raman analysis, the most intense Raman peaks of both annealed samples were fitted with Lorentzian and Gaussian functions. Thus, the FWHM value of CZTSe-2 sample's main Raman peak was found as 4.64 cm^{-1}, while that of CZTSe-3 sample was around 3.89 cm^{-1}. This result could be taken as the indication of the improved crystalline quality of the CZTSe-3 film. Raman measurements also confirm the SEM result, which indicates the peak of Cu_2SnSe_3 in the Raman spectra for as-grown sample of CZTSe-3 film.

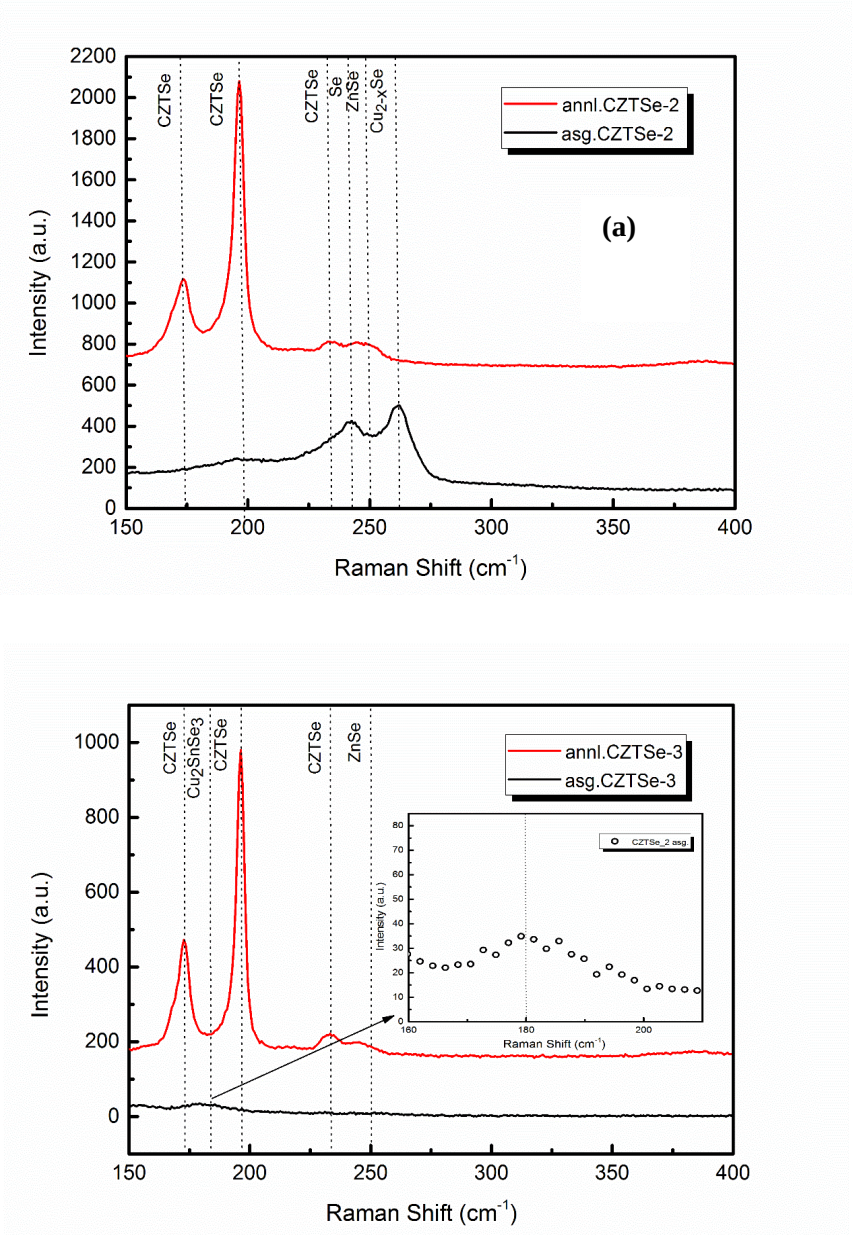

Figure 4.10 Raman Measurements for (a) CZTSe-2 and (b) CZTSe-3 Thin Films

4.3.2.2 Optical Characterization of CZTSe-2 and CZTSe-3 Thin Films

Transmission measurements for CZTSe-2 and CZTSe-3 thin films are given in Fig.4.11. As seen from the figure, there is a significant increase in the transmission value after post-annealing. This might be due to re-evaporation of some binary

compounds or elementary selenium from the surface with increasing annealing temperature.

As a result of this change, the thickness of films decreased about 70nm measured under the same conditions by Dektak 6M thickness profilometer after annealing process. By using the Equation 4.1, the optical absorption coefficient was calculated from the spectral measurements of transmission and reflection. Then the optical band gap and the optical transition natures of each film depending on photon energy were determined by using the Equation 4.2.

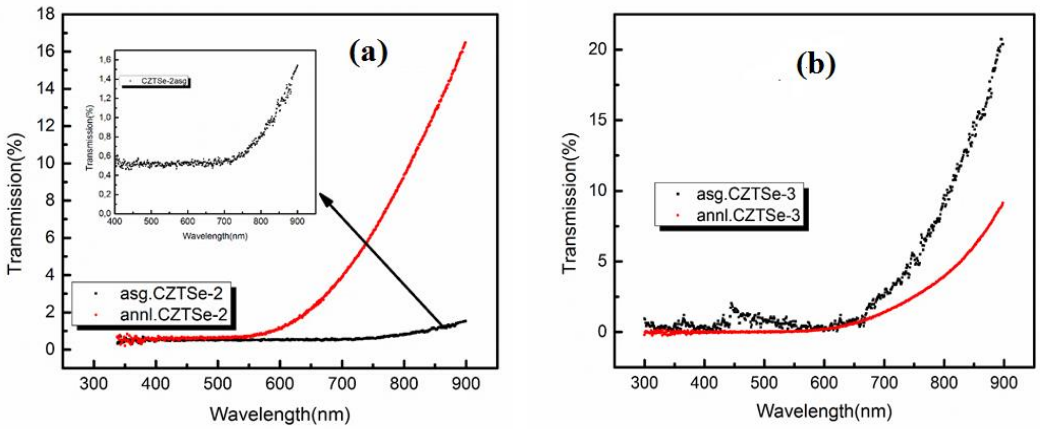

Figure 4.11 Transmission Measurements for (a) CZTSe-2 and (b) CZTSe-3 Thin Films

Figure 4.11 shows $(\alpha h\nu)^2$ versus photon energy ($h\nu$) plots corresponding to two different linear regions for as-grown and annealed CZTSe-2 and CZTSe-3 thin films.

As seen from Table 4.4, the direct optical band gaps have been determined as $E_{g1} \approx 1.10$ eV and $E_{g2} \approx 1.40$ eV.

The optical band gaps 1.10 eV is close to the reported values around 1.0 eV for CZTSe thin films in the literature [17],[18]. The band gap value around 1.0 eV is generally determined for Cu-poor condition [26], [94]. EDS results showed that all samples were Cu-poor, so this could be the reason for that E_{g1} values lying around 1.0 eV. Moreover

it was reported that the band gap of Kesterite and Stannite CZTSe phases were 1.05 eV and 0.89 eV, respectively[95]. Therefore, E_{g2} value around 1.40 eV most probably related to secondary phases[96], [97] . This band gap may be the indication of other binary phases like ZnSe and CuSe [19] but XRD results showed that the secondary phases disappeared following to the annealing. Furthermore it was reported that XRD measurements may not resolve the peak positions among CZTSe and other Se incorporated phases. On the other hand, some studies indicated that $E_g \approx 1.4$ eV belongs to CZTSe phase [95], [98].

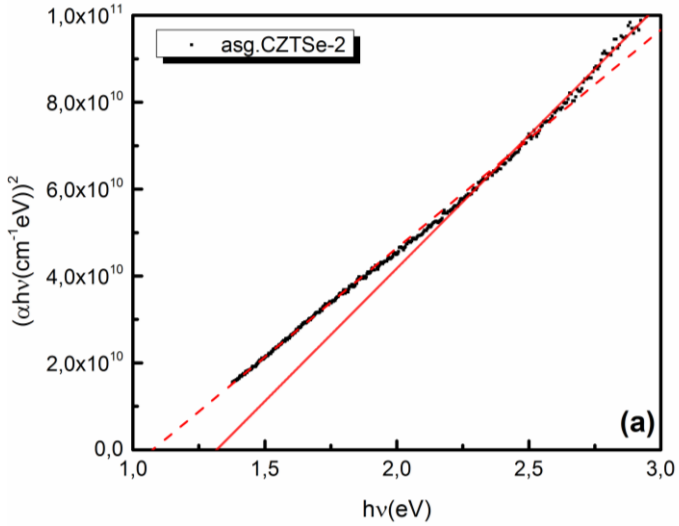

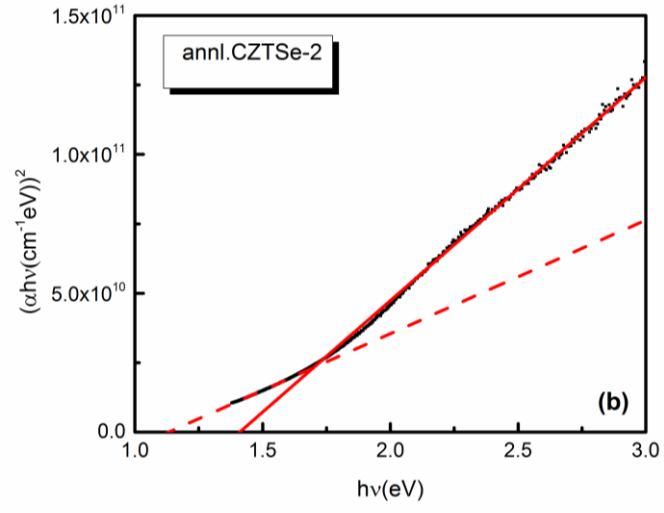

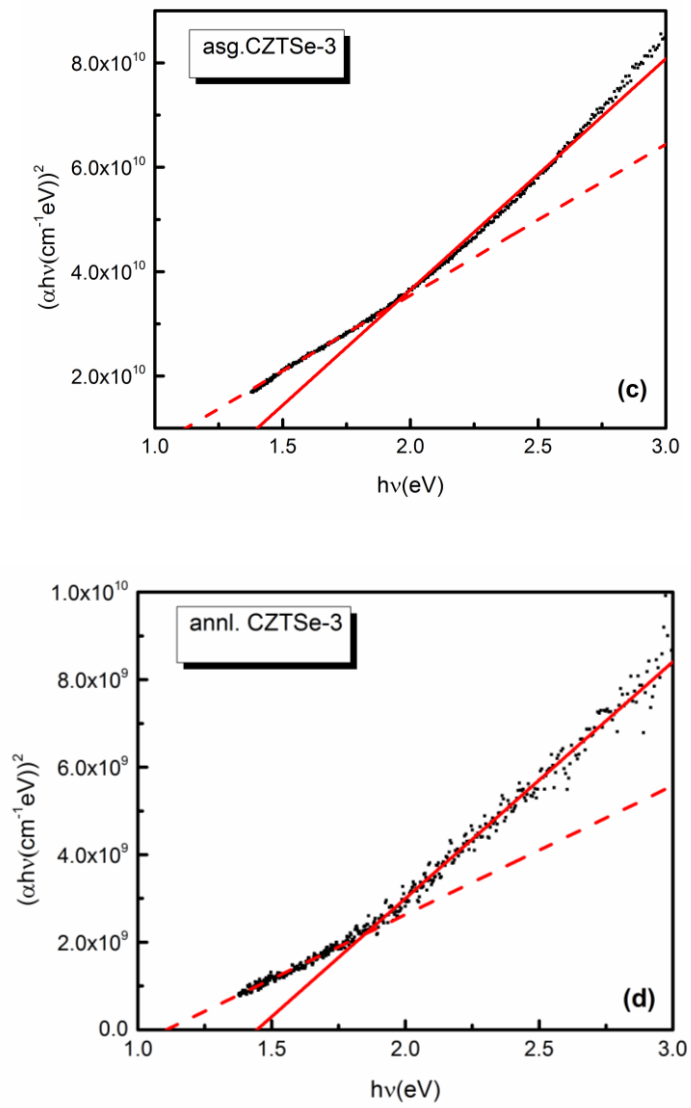

Figure 4.12 (αhν)2 vs hν plots for (a) asg.CZTSe-2, (b) annl. CZTSe-2, (c) asg. CZTSe-3, (d) annl. CZTSe-3 thin films.

Table 4-4 Band gap values for CZTSe-2 and CZTSe-3 thin films

Sample	***E_{g1} (eV)***	***E_{g2} (eV)***
asg.CZTSe-2	1.09	1.32
annl.CZTSe-2	1.13	1.40
asg.CZTSe-3	1.11	1.41
annl.CZTSe-3	1.12	1.45

4.3.2.3 Electrical Characterization of CZTSe-2 and CZTSe-3 Thin Films

Electrical properties of CZTSe thin films were determined by van der Pauw geometry resistivity and Hall effect measurements under the magnetic field strength of 2000 Gauss. Table 4.5 shows resistivity, Hall mobility, and carrier density of the CZTSe thin films deposited by changing the precursor orders and annealed at 450^0C. It was observed that all films have p-type behavior. As seen from the table, the value of resistivity increases with annealing. Moreover, the resistivity values of asgrown films are approximately close to the resistivity of CuSe films[99]–[101]. This result is parallel to the XRD and Raman results of asgrown films, which indicates the existence of CuSe secondary phase in CZTSe films. The increases in the value of resistivity lead to decrease in the value of carrier density. These variations are not only factors that affects the changes in the values of Hall mobility. Scattering mechanism has also effect on Hall mobility [100].

Table 4-5 The results of electrical measurements for CZTSe-2 and CZTSe-3 thin films

Sample	*ρ (Ω.cm)*	*n(cm^{-3})*	*μ(cm^2/V.s)*
asg.CZTSe-2	$2.01x10^{-3}$	$30.9x10^{19}$	0.62
annl.CZTSe-2	$1.53x10^{-1}$	$4.82x10^{19}$	0.75
asg.CZTSe-3	$4.03x10^{-3}$	$20.6x10^{19}$	0.51
annl.CZTSe-3	$1.32x10^{-1}$	$8.05x10^{19}$	0.61

The photo-conductivity characteristics of CZTSe-2 thin films were analyzed with the temperature dependent conductivity measurements under different illumination. Figure 4.12 illustrates the variation of conductivity with temperature and illumination for annl. CZTSe-2 thin film in the temperature region of 100-380 K.

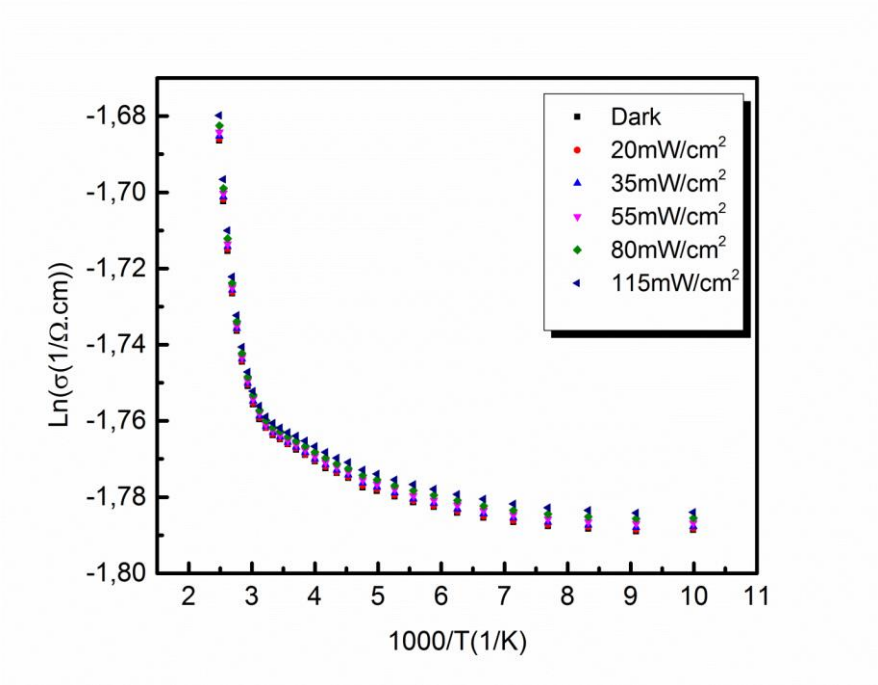

Figure 4.13 The variation of the conductivity with temperature and illumination intensity for annl.CZTSe-2 thin film

CZTSe-2 thin film sample showed thermionic emission characteristics as a conductivity behavior in the temperature region of 100-380 K. In Figure 4.13, there are seen wo distinct linear region which are high temperature (300-380K) and low temperature (200-280K). By using Equation 4.3, the activation energies were calculated for the dark condition. For the high temperature range, the activation energy Ea_1 was found as 109 meV and the activation energy for the low temperature region Ea_2 was found as 82 meV. Since the deposited films are not deliberately doped, the calculated activation energies are possibly due to the intrinsic defects stimulated as a consequence of deviation from the stoichiometry during the deposition.

CHAPTER 5

DEVICE APPLICATIONS OF CZTSe THIN FILMS

According to the results of Chapter-4, it is deduced that CZTSe-2 thin films have better physical properties than that of CZTSe-1 and CZTSe-3 thin films. Hence, during the device application of CZTSe thin films, the deposition process that was applied to CZTSe-2 thin films were used.

5.1 Fabrication and Device Characterization of Ag/n-Si/p-CZTSe/In Heterostructure

5.1.1. Introduction

In device applications, the use of heterostructures is a considerable research field for determining and manipulating the electronic and optoelectronic properties of semiconductor devices [102]. Under these circumstances, constructing Si-based diode structure has been commonly point of interest in order to find the fundamental of diode characteristics of the synthesized thin film layer [103]. In electronic research field, Si-wafer is a popular material of choice due to well-known and established material with abundant and non-toxic characteristic [104], [105].

The device behavior of CZTSe thin film layers from the junction fabricated with the Si-wafer is detailed in this chapter. Firstly, the fabrication Ag/n-Si/p-CZTSe/In heterostructure is introduced in the section of experimental details. Then the device characteristics of p-CZTSe/n-Si heterojunction are detailed. In order to characterize the heterojunction, room temperature and temperature dependent current-voltage (I-V) and capacitance-voltage (C-V) measurements are analyzed under dark and illuminated conditions. Moreover, the illumination effects on the device behavior of p-CZTSe/n-Si heterojunction are investigated.

5.1.2 Experimental Details

CZTSe thin films were deposited by thermal evaporation method onto one side polished 600 μm thick n-type Si (100) wafers with the resistivity value of 1–10 Ω-cm. in a stacked layer formation. Deposition was carried out sequentially from pure elemental (Cu,Sn.Zn,Se(Alfa Aesar, USA)) evaporation sources and during the deposition, substrate temperature was kept at room temperature and the vacuum was controlled at about 10^{-6} Torr. Following to the deposition of the stacked layers, the substrate temperature in-situ was increased slowly to 400 ^{o}C. The films were annealed at this temperature for an hour under Se evaporation. The thickness of the films was close to 700 nm after the deposition and selenization process. Furthermore, annealing process was applied under nitrogen atmosphere at 450 ^{0}C (annealed) to get the secondary and elemental phases free structural properties.

In order to study the device behavior of Ag/n-Si/p-CZTSe/In heterojunction structure, Ag back block ohmic contact annealed at 450 C before the evaporation of p-CZTSe films was deposited and following to the polished surface cleaning of n-Si wafer, Indium(In) dot ohmic contacts in 1mm diameter using copper masks were coated by thermal metallic evaporation after thin film growth. To deduce the device characteristics of the fabricated Ag/n-Si/p-CZTSe/In heterojunction structure, it was analyzed by using current–voltage (I-V) and the room temperature capacitance-voltage (C-V) measurements for frequencies of 10 kHz and 1000 kHz under dark and illumination conditions. During these analyses, the computer-controlled measurement setup with a 2401 source measure unit, the Model 22 CTI Cryogenics closed-cycle helium cryostat and DRC-91C temperature controller were used. By the same way, the frequency dependent C-V measurements were carried out by using HP 4192A LF Impedance Analyzer.

5.1.3. Results and Discussions

The schematic diagram and cross sectional SEM micrographs for Ag/n-Si/p-CZTSe/In heterostructure were given in Fig. 5.1.

As seen from figure, SEM micrograph of the annealed film shows uniform surface morphology with thickness of ~670nm that is almost the same average value measured by Dektak profilometer.

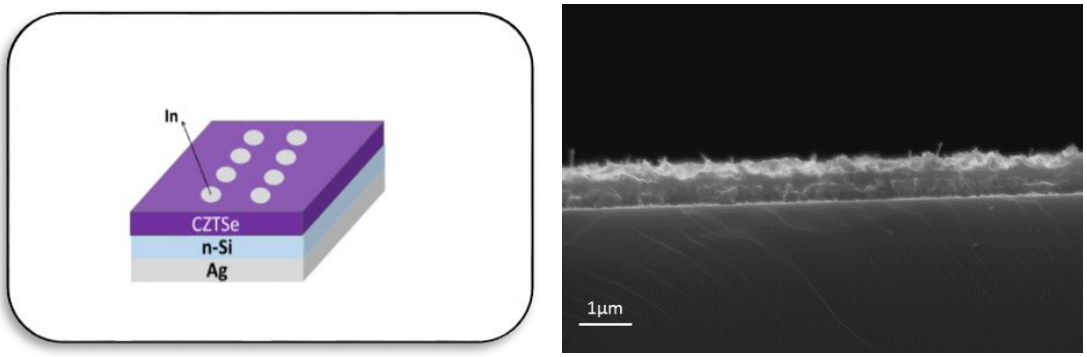

(a) **(b)**

Figure 5.1(a) The schematic diagram of Ag/n-Si/p-CZTSe/In heterostructure and (b) the cross sectional SEM micrograph

5.1.3.1. Room Temperature Current-Voltage (I-V) Characterization

I-V characteristics for Ag/n-Si/p-CZTSe/In heterostructure were measured under dark and illuminated conditions at room temperature as given in Figure 5.2. The behavior was analyzed by using standard diode expression;

$$I = I_0 \left[\exp\left(\frac{q(V - IR_s)}{nkT} \right) - 1 \right] \tag{5.1}$$

where, I_0 is the reverse saturation current, V is the bias voltage, R_s is the series resistance, n is the ideality factor and k is the Boltzmann constant [106].

The reverse saturation current is given by the following relation;

$$I_0 = AA^*T^2 exp\left(-\frac{q\Phi_b}{kT}\right) \quad (5.2)$$

In this equation, ϕ_b is the potential barrier, A is the device area, A^* is Richardson constant for n-type Si,[107]. By using Equation-5.1, the diode ideality factor "n" can be deduced as;

$$\frac{1}{n} = \frac{kT}{q}\frac{d(\ln(I))}{dV} \quad (5.3)$$

For the ideal contact, value of n should be equal to one where the pure thermionic emission mechanism is the dominant transport mechanism. However, for this structure it is greater than one, the contribution of the other transport mechanisms such as tunneling and recombination should be taken into account[15], [108], [109].

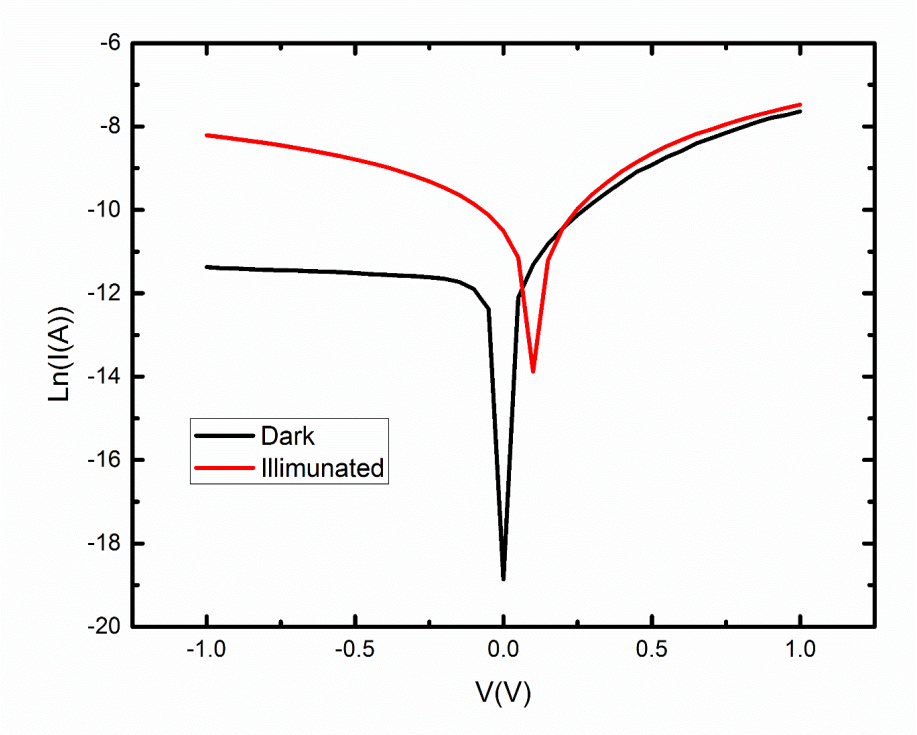

Figure 5.2 ln(I) vs. V graph for Ag/n-Si/p-CZTSe/In heterostructure under dark and illuminated conditions

Figure 5.2 points out ln(I) vs V plot for the heterostructure. By using this plot, experimental ϕ_b and *n* values were calculated from the current axis intercept and the slope of the linear region of the forward-bias region for both dark and illuminated conditions. While the barrier height ϕ_b and *n* values were calculated as 0.84 eV and 2.69 for the dark condition, 0.53 eV and 2.40 for illuminated condition, respectively According to the studies given in the literature on the similar Si-based heterostructure, the calculated room temperature n values are consistent with the reported values [98], [102], [110]. When the complete diode structure was considered, they were different from each other depending on Se and/or S contribution in the film structure and the calculated ϕ_b values were greater than the reported values[103], [110]On the other hand, Fig. 6 shows that the reverse current of the heterostructure increases with illumination. This increase was consistent with the generated carriers due to the light absorption and their contribution to the photocurrent [111].

As seen from I-V characteristics, they deviate from linearity both in forward and reverse bias voltages for each condition. At the high forward bias values, the junction resistance reaches to a constant value, which equals to R_s value. The same behavior occurs also in the reverse bias voltages leading to the determination R_{sh} value. The series resistance R_s is the resistance of the bulks and metallic contacts, on the other hand, the shunt resistance R_{sh} is responsible for the loss of the current at the edge of the device and the surface inhomogeneity[112], [113]. R_s and R_{sh} are the parasitic resistances of the device structure and they were calculated by using the expression, R_i=dV/dI [114], [115].

In general, R_s in the diode has pronounced effect on the fill factor, and it could be the reason of low short-circuits current values. On the contrary, low R_{sh} value in the diode can provide an alternative conduction path for the light-generated current and therefore, it can pave the way for power losses in diodes. For dark and illuminated conditions, R_s values were obtained as 610 Ω and 379 Ω respectively. This reduction in the value of R_s with the illumination could also be the determination of the increase in the conductivity with the generated photocurrents [115]. Furthermore, R_{sh} values for the dark and the illuminated conditions were obtained as 2.8 MΩ and 3.8 MΩ

respectively. The augmentation of the R_{sh} values with the illumination may be the indication of local inhomogeneities. They could lead to non- uniform flow of current across the heterojunction[116], [117]. Shunt resistance is generally related with the localized defect regions and these regions become electrically active with the traps having larger concentrations. In fact, these traps could behave as cavity for majority carriers or light-generated minority carriers and they capture carriers from neighborhood regions [116], [118]. When the heterojunction is illuminated with the light source, the trap starts getting filled and this reduces the shunt current, that leads to increase in the shunt resistance of the diode [119], [120].

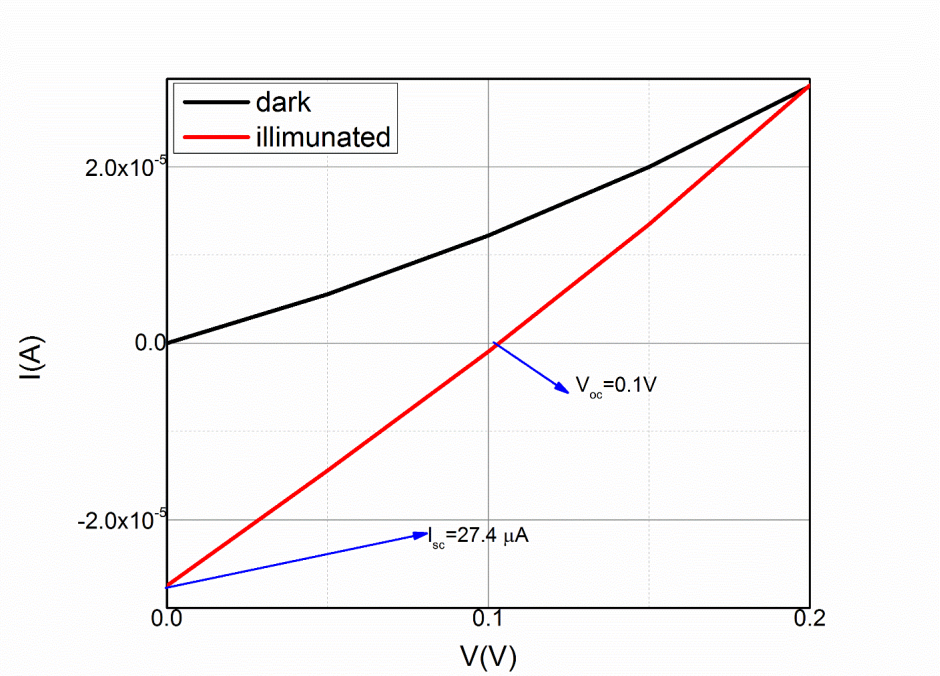

Figure 5.3 I-V plot in the voltage range of 0 - 0.2 V for dark and illuminated conditions

Figure 5.3 shows I-V plot in the voltage range of 0 and 0.2 V for both dark and illuminated conditions. These plots indicate that, Ag/n-Si/p-CZTSe/In heterostructure responses to illumination having the open circuit voltage (V_{oc}) value of 100 mV and the short circuit current I_{sc} value of 27.4 µA. Therefore, these values can be taken as the primary works in this fabrication of simple p-n junctions of kesterite thin films by n-Si substrate [103], [121]. When the solar cell parameters obtained in this work were

compared with the other studies, this device structure exhibits a good electronic behavior under solar illumination.

5.1.3.2. Temperature-Dependent I-V Characterization

The fabricated heterostructure was characterized by temperature dependent current-voltage (I-V) measurements. According to this analysis, diode parameters were calculated as a function of sample temperature and possible conduction mechanisms were analyzed. The experimental semi-logarithmic forward bias I-V curve of the In/CZTSe/Si/Ag sandwich structure is given in Figure 5.3 in the temperature range of 220-360 K. As seen from the figure, the deposited structure shows a rectifying behavior in the studied voltage range.

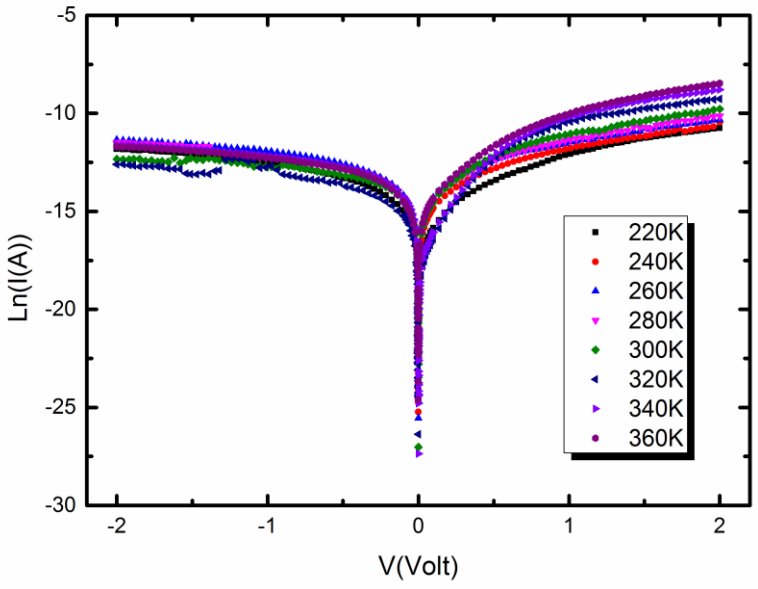

Figure 5.4. Temperature dependent I-V characteristics for In/CZTSe/Si/Ag Heterostructure

The I-V curve was analyzed due to thermionic emission model as discussed in the previous part. The obtained results are tabulated in the Table 5-1. As given in the table, both Φ_b and n values were found in strongly temperature dependent. Φ_b values have

an increasing characteristic with increase in temperature as different than the expected I-V behavior. When temperature increases, carriers gain sufficient energy to overcome the potential barrier and contribute to the total current. On the other hand, at low temperature condition, barrier inhomogenities with lower barrier patches affect the current flow, and the charge carriers can pass over the patches with lower barrier heights in the barrier formation in the diode [122], [123]. The obtained n values are in the range of 1.8-5.1 and they show a decreasing behavior with increase in temperature as listed in Table 5-1. In addition to the fact that the current transport mechanism in the diode structure is contrary to TE and the additional mechanism can be required to explain the current flow through the junction, the high value of n can be attributed to the native insulator layer formation at the junction interface and particular distribution of interface states localized in this region[124].

Table 5-1 Results of the Temperature Dependent I-V Analysis of In/CZTSe/Si/Ag Heterostructure

T (K)	n	Φ_b (eV)
220 K	5.11	0.537
240 K	4.19	0.572
260 K	2.93	0.616
280 K	2.77	0.671
300 K	2.44	0.708
320 K	2.24	0.835
340 K	2.01	0.883
360 K	1.81	0.881

The obtained ideality (n) and barrier height Φ_b values are found in a linear correlation between each other and this behavior was shown in Figure 5.5. According to the Tung's approach, the observed linear behavior can be attributed to the lateral inhomogeneity of the barrier heights [12, 15] and it was analyzed by linear fitting

process. The extrapolation of the Φ_b values to $n = 1$ in this plot gave the value of 0.916 eV which is different from the band gap value of n-Si and this result indicates that TE model cannot be the only predominant current transport mechanism in the device structure.

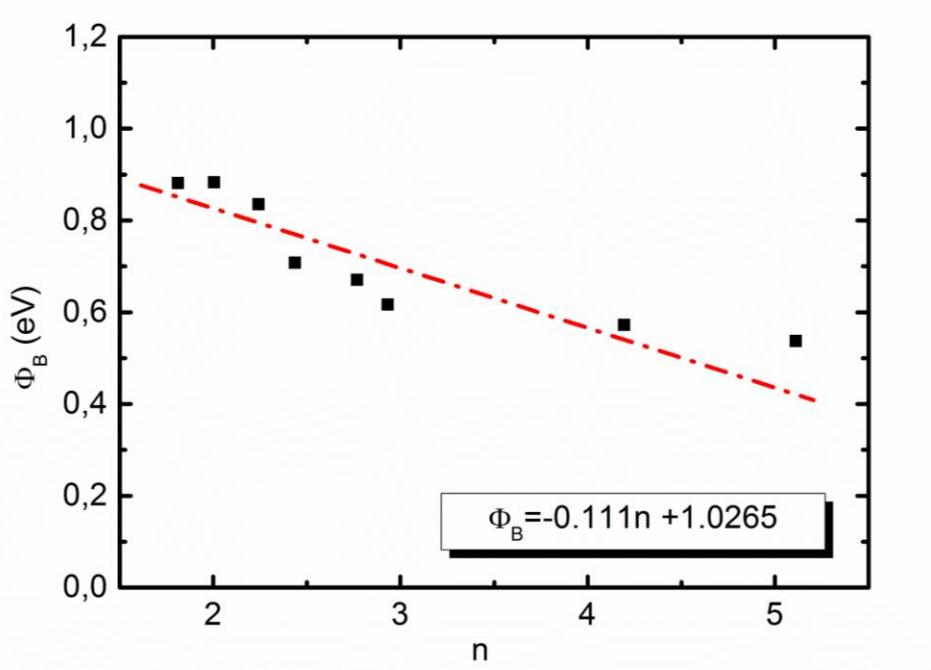

Figure 5.5. Φ_b vs n plot for In/CZTSe/Si/Ag heterostructure

Based on the characteristics of the diode with calculated main diode parameters as a function of temperature, abnormal deviation from classical TE theory can be modelled by Gaussian distribution (GD) of the barrier height at the junction interface [123-124]. This model is applied under the assumption of barrier inhomogeneity with localized low barrier patches at the interface.

In this case, current transport theories for homogeneous barrier height is extended to cover the effect of inhomogeneous barrier formation and the distribution of the inhomogeneity in the barrier height is explained with standard statistical distribution. The standard deviation σ_o of this distribution roughly estimates the level of barrier inhomogeneities with respect to the mean value of barrier height $\bar{\Phi}_b$ [123]. Therefore,

with modification in barrier height, total current I(V) through a barrier at forward bias region can be expressed as [122], [124];

$$I = AA^{*}T^{2}exp\left[\left(-\frac{qV}{kT}\right)\left(\bar{\Phi}_{B0} - \frac{q\sigma_0^2}{2kT}\right)\right] \quad (5.4)$$

$$exp\left(\frac{qV}{n_{ap}kT}\right)\left[1 - exp\left(-\frac{qV}{kT}\right)\right]$$

with modified reverse saturation current expression as,

$$I_0 = AA^{*}T^{2}exp\left(-\frac{q\Phi_{ap}}{kT}\right) \quad (5.5)$$

where Φ_{ap} and n_{ap} are the apparent barrier height and ideality factor, respectively. In this expression, σ_0 gives the standard deviation in temperature dependence of barrier height and it is used to measure the deviation from the homogeneity of barrier height in the junction.

From Eq.5.4, the temperature variation of zero bias barrier height distribution can be represented in terms of GD as [124,125],

$$\Phi_{ap} = \bar{\Phi}_b - \frac{q\sigma_0^2}{2kT} \quad (5.6)$$

As in the case of Eq.5.6 there should be a linear relation between Φ_b and q/2kT (see Figure 5.6) and from the straight line intercept and slope, $\bar{\Phi}_b$ and σ_0 were calculated. Thus, σ_0 was obtained as 0.191 eV which is about 13% of the mean value of barrier height, 1.46 eV. This result indicates the interfacial inhomogeneities with a GD of barrier heights at the interface [124]. The single straight line observed in Figure 5.6 also verifies a presence of a single Gaussian distribution of barrier height.

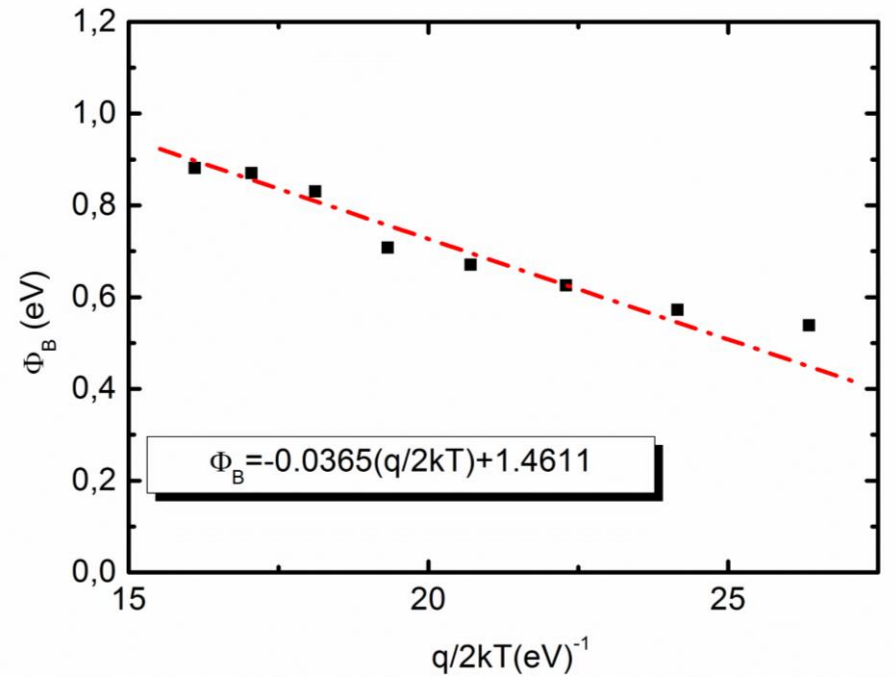

Figure 5.6. Φ_b vs q/kT plot for In/CZTSe/Si/Ag heterostructure

In this model, the variation of n_{ap} with T is given by [124,125];

$$\left(\frac{1}{n_{ap}} - 1\right) = -\rho_2 + \frac{q\rho_3}{2kT} \tag{5.7}$$

where ρ_2 and ρ_3 are the parameters related to voltage deformation of the barrier height distribution. In this case, σ_0 and $\bar{\Phi}_b$ are linearly bias dependent with ρ_2 and ρ_3, respectively. As shown in Fig.5(b), linear behavior of the plot of $(n^{-1} - 1)$ vs $q/2kT$ confirms voltage deformation of the Gaussian distribution of the barrier height in terms of calculated *n* values [cjp9, 10] and by applying linear fitting process to the straight line in this plot, the voltage coefficients were calculated from the slope and intercept as, ρ_2=0.0396 V and ρ_3=0.0323, respectively.

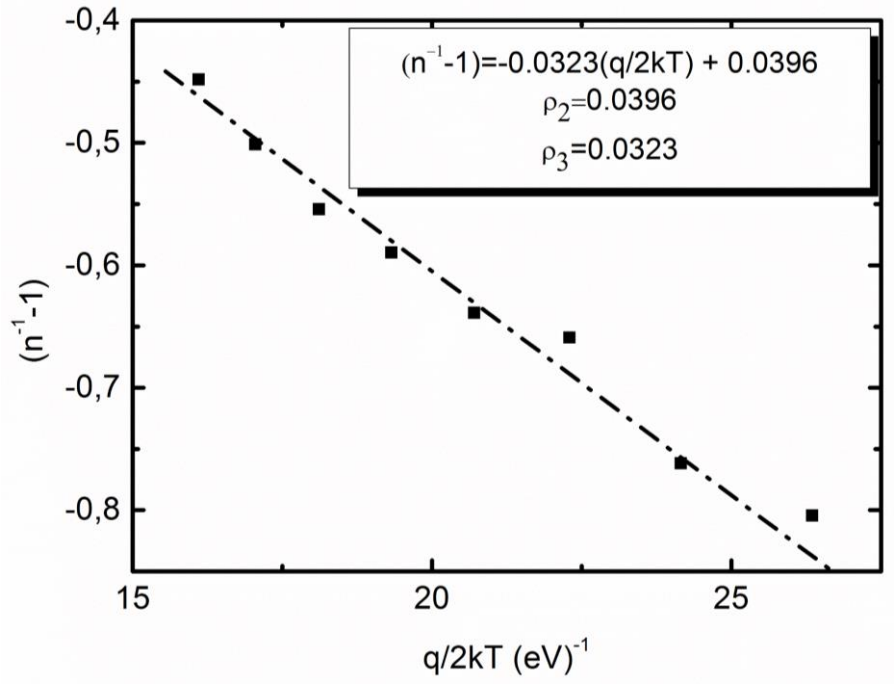

Figure 5.7 (n^{-1}-1) vs q/2kT plot for In/CZTSe/Si/Ag Heterostructure

with the observation of barrier inhomogeneity, according to GD of the barrier heights, the modified Richardson equation can be expressed as [124];

$$\left(\frac{I_0}{T^2}\right) - \left(\frac{q^2\sigma_0^2}{2k^2T^2}\right) = \ln(AA^*) - \frac{q\bar{\Phi}_b}{kT} \tag{5.8}$$

From this relation, the Richardson plot $\ln(I_0/T^2)$ vs $1/T$ was modified as $\ln(I_0/T^2) - (q^2\sigma_0^2)/(2k^2T^2)$ vs q/kT given in Figure 5.7 Using the experimental I_0 values, $\bar{\Phi}_b$ and modified Richardson constant A^* were obtained with the slope and the intercept of the straight line as 1.463eV and 130.387Acm^{-2}K^{-2}, respectively.

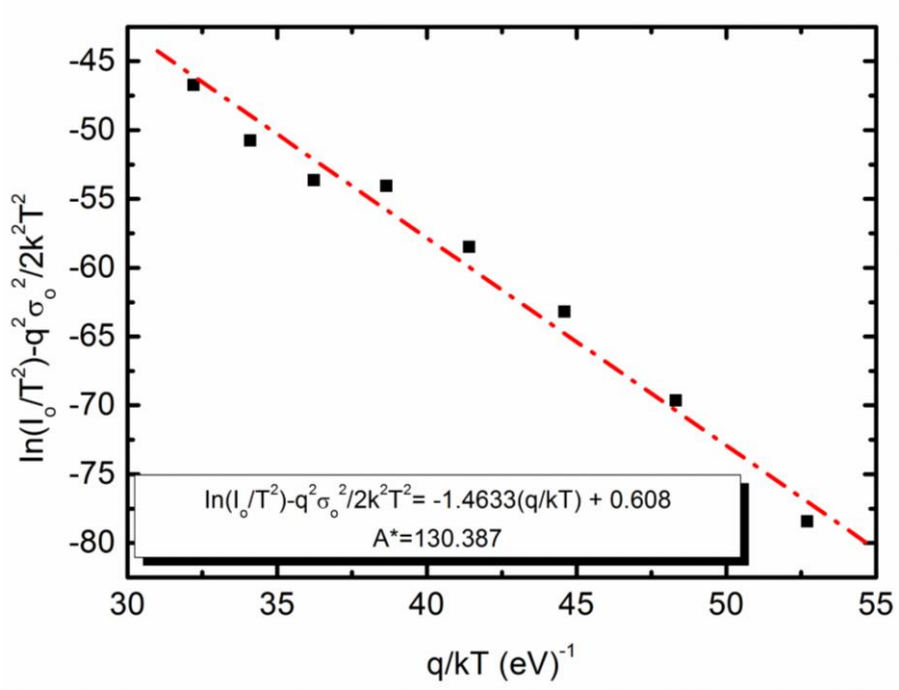

Figure 5.8. Plot of $\ln(I_0/T^2) - (q^2\sigma_0^2)/(2k^2T^2)$ vs q/kT for In/CZTSe/Si/Ag Heterostructure

5.1.3.3. Capacitance-Voltage (C-V) Characterization

C-V measurements give information about built-in potential, carrier concentration, series resistance, surface states, etc. of the heterostructure. In order to get the information about these values, C-V measurements were carried out under both dark and illuminated conditions. Moreover, these measurements were done for different frequencies at 10 kHz and 1000 kHz for both conditions. Figure 5.4 indicates that, in the higher frequency case, there is no a significant effect of the illumination on the C-V characteristics. However, for lower frequency under dark condition; the plot has a peak due to the presence of interface states. By the illumination, these states disappearing. Moreover, capacitance values decreased with the illumination. When the sample is illuminated, some of the carriers generated due to the illumination could be trapped, or the illumination may result in the release of the trapped electrons. These trapping and releasing processes can be considered as charging and discharging respectively. Moreover, they are random processes in the n-Si with the illumination

and they may occur at the same time. When the charging process is dominant, capacitance decreases [125], [126]. Moreover, the anomalous peak at zero bias, in the dark condition case, disappeared with the illumination. This disappearance may be consisted with the thermal effect due to the illumination [127].

C–V characteristics were analyzed by using the following expression;

$$\frac{1}{C^2} = \frac{2}{qN_d\varepsilon_o\varepsilon_s A^2}(V_{bi} - V) \tag{5.4}$$

$$N_d = \frac{2}{q\varepsilon_O\varepsilon_S A^2\left[\frac{d}{dV}\left(\frac{1}{C^2}\right)\right]} \tag{5.5}$$

where V_{bi} is the built-in potential, N_d is the donor concentration. ε_o is the permittivity of free space, ε_s is the dielectric constant of Si (11.7) and A is the diode area.

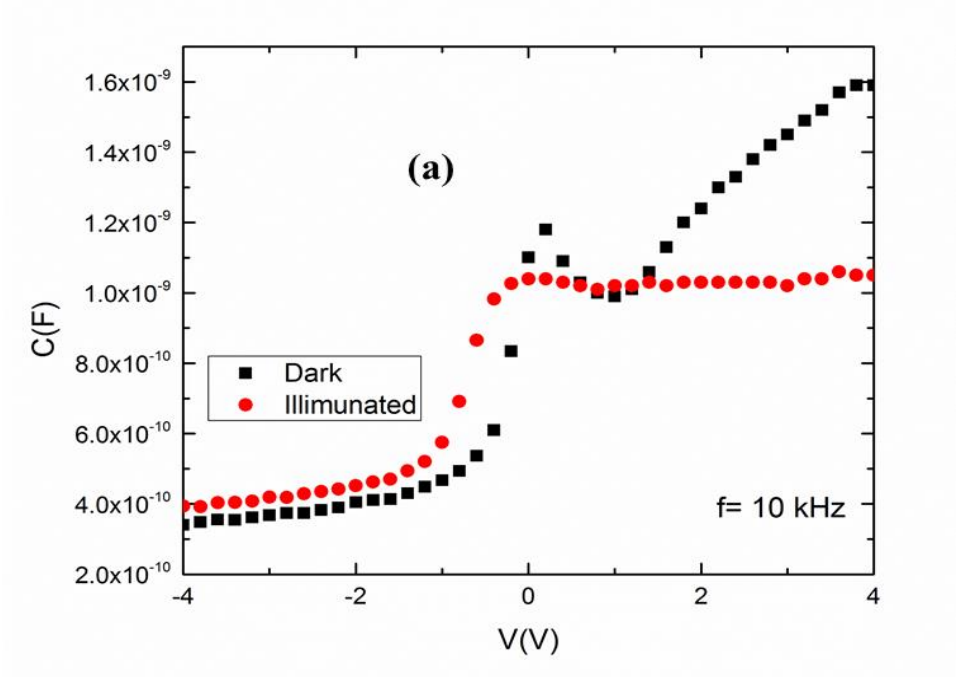

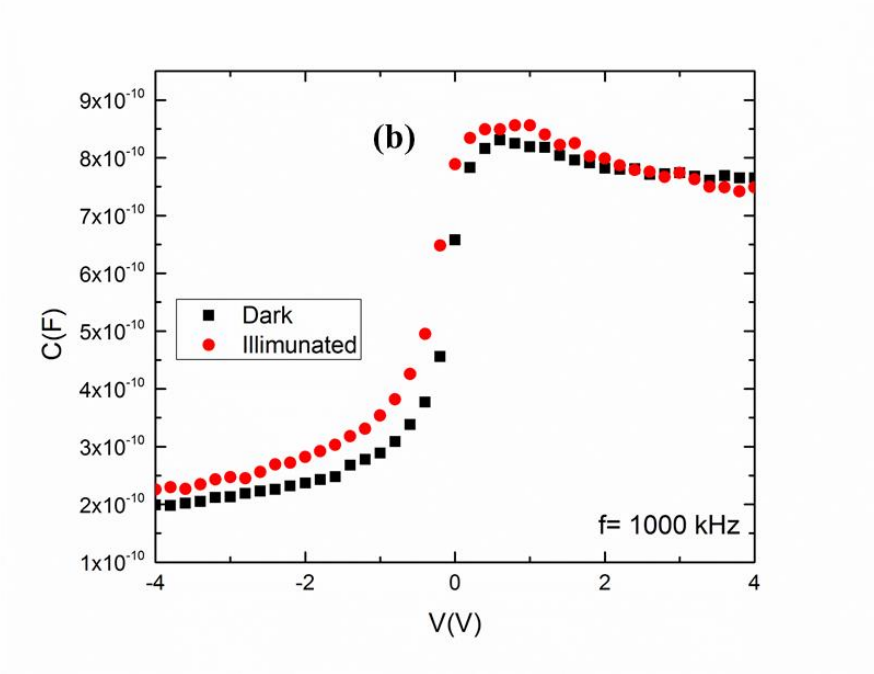

Figure 5.9 Capacitance-Voltage (C-V) plots for the frequency of (a) 10 kHz (b) 1000 kHz under dark and illuminated conditions.

C^{-2} vs V plots for different frequencies are shown in Figure 5.5. Their variations are linear with the intercept on voltage axis which gives the built-in potential and from the slope of this plot; carrier concentration (N_d) can be calculated by using equation-5.5. Moreover, the barrier heights (Φ_b) of the heterojunction diode can be calculated from the equation;

$$\Phi_b = V_{bi} + \frac{kT}{q}\ln\left(\frac{N_C}{N_d}\right) \tag{5.6}$$

where N_c is the effective density of state in the conduction band (N_c=2.8x10^{19}cm^{-3}). All results for all conditions are tabulated in Table-5.1.

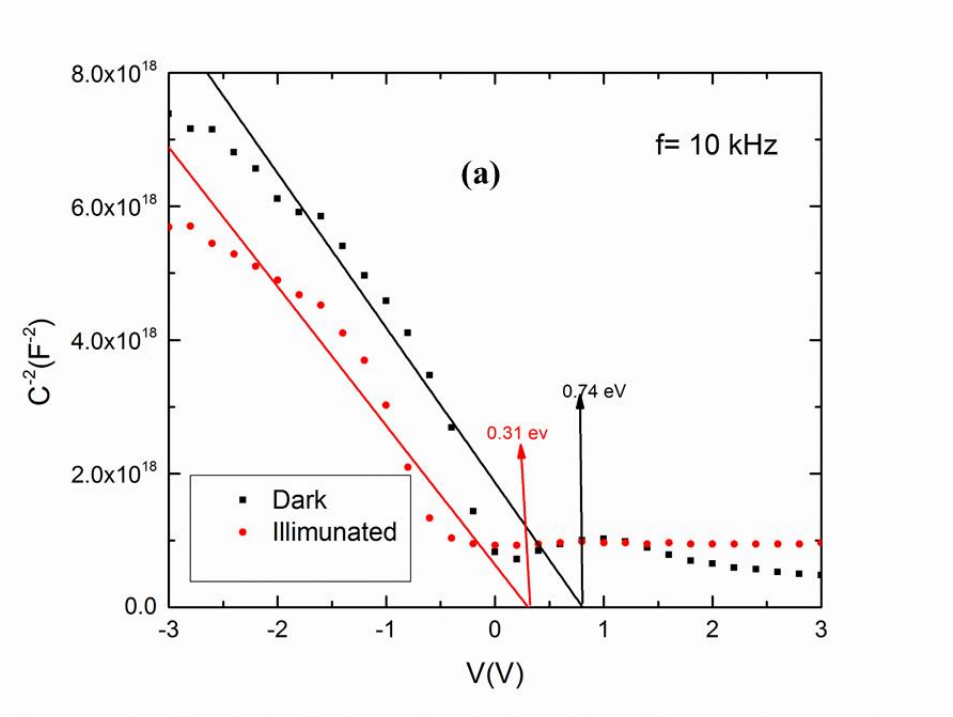

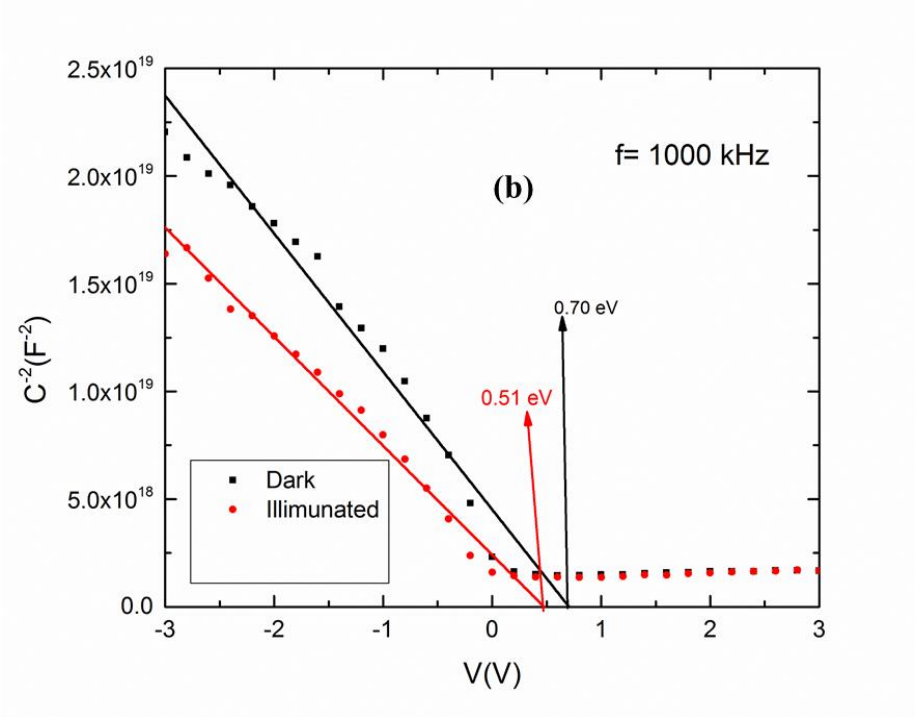

Figure 5.10 C^{-2} vs V plot for the frequency of (a) 10 kHz and (b) 1000 kHz under dark and illuminated conditions

Table 5-2The calculated device parameters from the slope and intercept values of C^{-2} vs V graph

Condition	**V_{bi} (eV)**	**Nd (cm^{-3}) x 10^{16}**	**Φ(eV)**
10 kHz (dark)	0.70	3.35	0.87
10 kHz (illum.)	0.51	4.21	0.67
1000 kHz (dark)	0.74	9.29	0.88
1000 kHz (illum.)	0.34	10.3	0.49

As seen from Table-5.1, illumination led to increase in N_d values and decrease in V_{bi} and Φ_b values due to photo-generated carriers. Moreover, the barrier height values in dark condition obtained from I-V measurements were comparable with the values obtained from C-V analysis.

5.2. CZTSe/CdS Heterojunction

5.2.1 Introduction

Characterization of CZTSe thin films and device analyses of this layer with the Si-wafer have been investigated to fabricate the absorber layer with the desired properties for solar cell applications. Within the acquired experience, p-CZTSe/n-CdS heterojunction has been fabricated and the photovoltaic behavior of this junction has been studied. This part gives an information about the fabrication and the device behavior of CZTSe/CdS heterojunction under the illumination.

5.2.2. Fabrication and formation of CZTSe/CdS Heterojunction

CZTSe absorber layer was deposited onto Indium Tin Oxide (ITO) coated glass substrate by thermal evaporation method as optimized with the previous study. Then,

CdS window layer was deposited onto CZTSe layer with chemical bath deposition method (CBD). Finally, Indium(In) dot ohmic contacts in 1mm diameter using copper masks were coated by thermal metallic evaporation after thin film growth. The schematic illustration of CZTSe/CdS heterojunction has been shown Figure 5.11 and Figure 5.12.

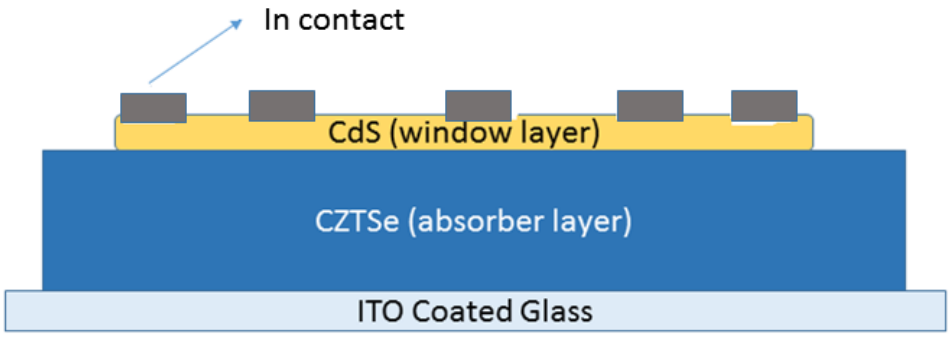

Figure 5.11 The schematic illustration of CZTSe/CdS solar cell

In order to understand the charge transport mechanism, the band diagram for CZTSe and CdS before the formation of heterojunction and the band alignment diagrom for CZTSe/CdS heterojunctioninterface has been illisturated in Figure 5.12. To figüre out the diagrams, the electron affinities of CZTSe (χ_{CZTSe}) and CdS (χ_{CdS}) thin films were considered as 4.10 and 3.60 eV, respectively [128], [129]. The band gap value of CdS (Eg_{CdS}) were taken as 2.42 eV [128], [129] . Additionally, the band gap value of CZTSe thin film (Eg_{CZTSe}) were taken as 1.40 eV which was the value of annealed CZTSe-2 thin film.

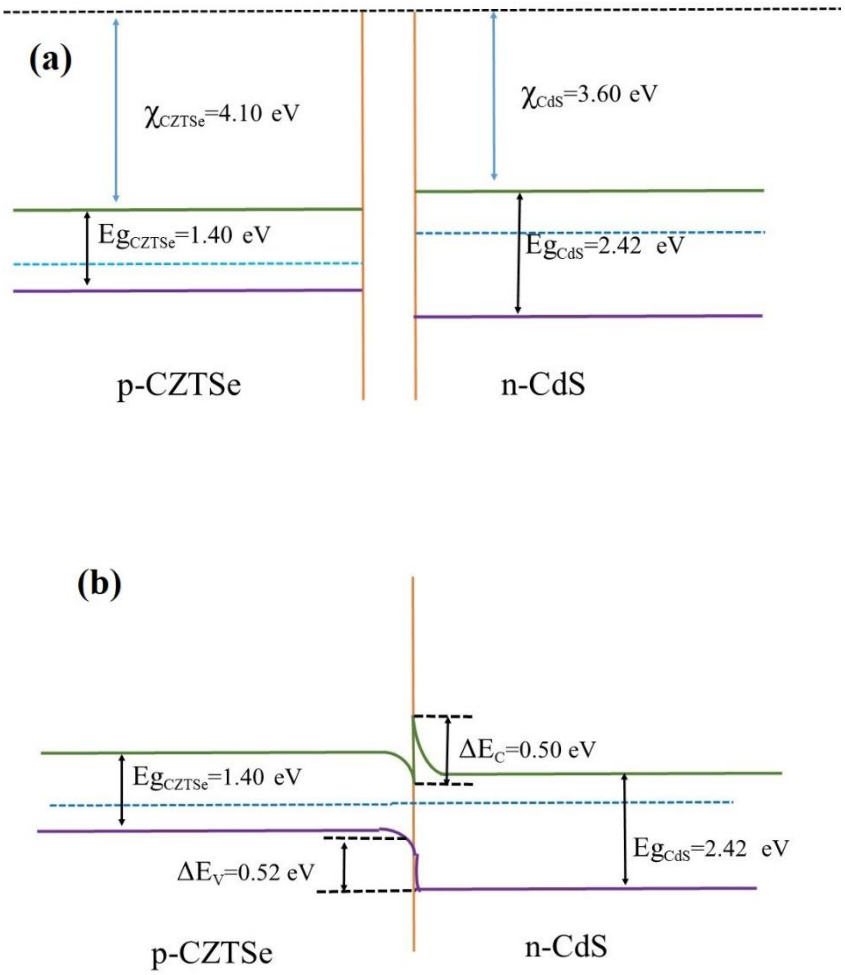

Figure 5.12 The band diagram of CZTSe and CdS before (a) and after (b)the formation of heterojunction

As shown in Figure 5.12, there are differences in the electron affinity and band gap values of CdS and CZTSe structures. Hence, the valence band edge of CdS is lower when compared to the valance band edge of CZTSe. Also, The conduction band edge of CdS is lower than that of CZTSe. These differences lead to formation of the the valace band offse (ΔE_v) and conduction band and valence band offset (ΔE_c) . Both ΔE_v and ΔE_c values were calculated as 0.50 eV. The ΔE_c value of 0.50 eV is the evidence of spike like conduction band offset that is the type-I heterojunction. In this type of junction, the conduction band electrons of p layer need to pass this barrier before being injected into the conduction band of n layer[130]. Therefore, the larger interface band

gap can decrease the carrier recombination from conduction band of n layer to valance band of p layer. It could be concluded that, the ΔE_c value of 0.50 eV is appropriate fort he fabrication of solar cell.

5.2.3. Photovoltaic Behavior of CZTSe/CdS Heterojunction

I-V measurement was carried to get the information about the response of this structure under the effect of the illumination. Solar simulator AM 1.5 condition was used during this measurement. The photovoltaic behavior was analyzed in terms of short circuit current I_{sc}, open circuit voltage $V_{oc,}$, fill factor FF and the conversion efficiency η. These parameters and the I-V curve has been given in Figure 5. 13.

The parameters have been found as 0.039mA, 0.36 V, 27 and 0.74% for I_{sc}, $V_{oc,}$ FF and η, respectively. Figure 5.13 illustrates that there is observed a high series resistance effect. This effect could be arisen from the bulk layer or the contact resistance. The high values of series resistance cause an increase in the photo-generated carriers recombination process which can results in reduction of the carrier collection by the contacts and also affect the solar cell efficiency and fill factor negatively [69].

The secondary phases in thin film also leads to the impurity scattering electrons that will reduce the degree of freedom of the electron and seriously affect the performance of device. Moreover, the grain size also affects the performance of films. The smaller the grain is, the more the grains per unit area are, and the more the grain boundaries are. However, the grain boundaries are the recombination centers, which will reduce the minority carrier lifetime and drift length[131]. As discussed in the previous part of the study, CZTSe thin films have both secondary phases and the small grain boundaries. This could be the reason for low efficiency.

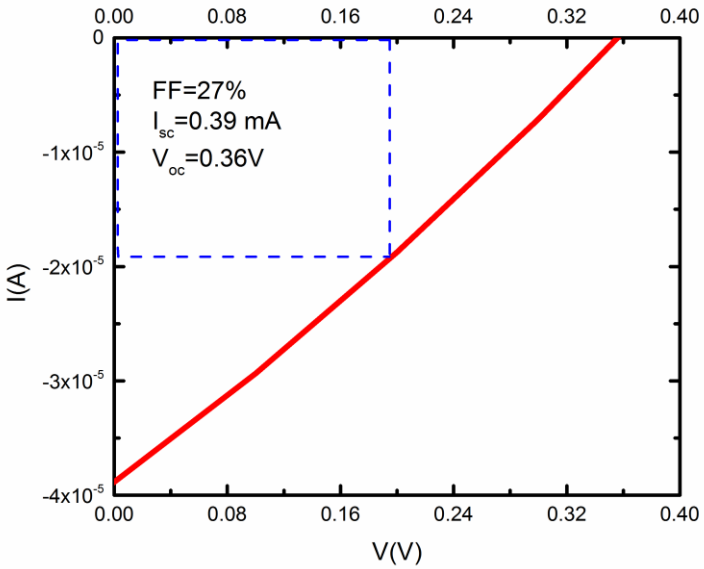

Figure 5.13 I-V characteristics of CZTSe/CdS Heterojunction under AM 1.5 condition

On the other hand, Transparent Conducting Oxide (TCO) layers play an important role on the device performance. TCO films require several characteristics, such as carrier transportation, light in-coupling, and light trapping. In addition, TCO (generally Al-doped ZnO called as AZO) films influence the electrical properties of solar cells [132]. In addition, intirinsic ZnO (i-ZnO) is used together with CdS or ZnS buffer layer. i-ZnO plays a role like shunting path covering layer between CdS and AZO and this makes improved V_{oc} for CZTSe solar cell.

The efficiency of the CZTSe/CdS solar cell could be improved by eliminating secondary phases and depositing both i-ZnO and AZO layers onto CdS layer.

CHAPTER 6

CONCLUSION

The main focus of this study was to fabricate CZTSe thin films by using single step PVD technique and utilizing in-situ selenization process. Also, determination of the material properties of CZTSe thin films under the effect of varying annealing processes and the device behavior of CZTSe thin film with the junction of Si-wafer and CdS layer are the another key points of the study.

CZTSe thin films were deposited by thermal evaporation technique by layer by layer method using elemental sources. The results of the deposition and the characterization of CZTSe-1 thin films indicated that CZTSe-1 thin films were non-stoichiometric. The structural, optical and the electrical properties of the films were not suitable to get efficient absorber layer. By using the experience of deposition and characterization of CZTSe-1 thin films, the deposition process was improved to fabricate the CZTSe thin films with desired properties. Moreover, the impact of precursor sequence during the growth of CZTSe thin films and also the influence of post-annealing process on material properties of deposited films were investigated (CZTSe-2 and CZTSe-3 thin films). It was observed that substrate temperature during the selenization was not adequate to form crystalline CZTSe structure since the agglomeration on the surface of the films were detected by SEM analysis. However, after the post-annealing process, XRD and Raman scattering measurements confirmed the presence of polycrystalline CZTSe structure. With these observations, it could be deduced that substrate temperature should be kept higher than 400°C during selenization or post-annealing to obtain homogenous structure. As a result of the comparative work based on different precursor layer order, XRD and Raman spectroscopy results indicated that the preferred growth process should be started with Sn layer which is labeled as CZTSe-2 thin films. From the optical characterization step, two distinct band gap

values were found around 1.10 and 1.40 eV. Moreover, post annealing led to increase in the transmission values, which might be the result of the decrease in thickness values caused by heat treatment. Electrical characteristics were found to be affected from secondary phase formation in the structure.

Device characterization of p-CZTSe/n-Si heterojunction were investigated in terms of room temperature I-V measurements both under dark and illuminated conditions, temperature dependent I-V measurements and also C-V measurements. I-V analysis of Ag/n-Si/p-CZTSe/In heterostructure showed that, Rs value reduced under illumination. This could be also the determination of the increase in the conductivity with the contribution of photo generated carriers. C-V analysis indicated that the heterojunction device parameters were completely related with the trap and interface states, so that the illumination may initiate the release of the trapped charges depending on the characteristics of trap levels and/or impurity states. This can be considered as the charging and discharging effect. Ag/n-Si/p-CZTSe/In heterostructure has a photodiode behavior having the Voc value of 100 mV and Isc value of 27.4 μA. This study can bring light to the studies which aim to develop a tandem structure based on well- developed high efficiency monocrystalline Si solar cells in long term. From the dark current–voltage characteristics in wide temperature range, main diode parameters were calculated by thermionic emission model and the results revealed the increasing barrier height and the decreasing ideality factor behavior with decreasing temperature, which could be the results of the barrier height inhomogeneity at the interface. Thus, the inhomogeneity at the interface was explained by Gaussian distribution of barrier heights. Under this approximation, mean barrier height (Φ_b) and standard deviation (σ_0) at zero bias were found to be 1.46 eV and 0.191V, respectively. By means of modified Richardson plot, Richardson constant was calculated as 130.387 $A.cm^{-2}K^{-2}$ which was close to theoretical value known for n-Si.

CZTSe/CdS heterojunction was fabricated and the junction showed a photovoltaic behavior under AM 1.5 conditions. The parameters have been found as 0.039mA, 0.36 V, 27 and 0.74% for I_{sc}, $V_{oc,}$ FF and η, respectively.

REFERENCES

[1] International Energy Agency IEA, “Solar Photovoltaic Energy,” *Technol. Roadmap*, p. 60, 2014.

[2] S. Energy, “Introduction Preliminary Remarks,” no. November, 2016.

[3] M. A. Green, “Silicon photovoltaic modules: A brief history of the first 50 years,” *Prog. Photovoltaics Res. Appl.*, vol. 13, no. 5, pp. 447–455, 2005.

[4] D. B. Mitzi, O. Gunawan, T. K. Todorov, K. Wang, and S. Guha, “The path towards a high-performance solution-processed kesterite solar cell,” *Sol. Energy Mater. Sol. Cells*, vol. 95, no. 6, pp. 1421–1436, 2011.

[5] G. Stechmann *et al.*, “3-Dimensional microstructural characterization of CdTe absorber layers from CdTe/CdS thin film solar cells,” *Sol. Energy Mater. Sol. Cells*, vol. 151, pp. 66–80, 2016.

[6] J. Ringman, “Press Release,” vol. 255070, no. June, pp. 80–81, 2016.

[7] “First Solar CdTe cell hits 22.1% efficiency.” .

[8] X. Liu *et al.*, “The current status and future prospects of kesterite solar cells: a brief review,” *Prog. Photovoltaics Res. Appl.*, vol. 24, no. 6, pp. 879–898, Jun. 2016.

[9] Y. Li, T. Yuan, L. Jiang, F. Liu, Y. Liu, and Y. Lai, “Cu2ZnSnS4 thin film solar cell fabricated by co-electrodeposited metallic precursor,” *J. Mater. Sci. Mater. Electron.*, vol. 26, no. 1, pp. 204–210, Jan. 2015.

[10] Z. Shi, D. Attygalle, and A. H. Jayatissa, “Kesterite-based next generation high performance thin film solar cell: current progress and future prospects,” *J. Mater. Sci. Mater. Electron.*, vol. 28, no. 2, pp. 2290–2306, Jan. 2017.

[11] “National Center for Photovoltaics | Photovoltaic Research | NREL.” .

[12] S. W. Shin *et al.*, “Studies on Cu_2ZnSnS_4 (CZTS) absorber layer using different stacking orders in precursor thin films,” *Sol. Energy Mater. Sol. Cells*, vol. 95, no. 12, pp. 3202–3206, Dec. 2011.

[13] N. Sakai, H. Hiroi, and H. Sugimoto, “Development of Cd-free buffer layer for Cu_2ZnSnS_4 thin-film solar cells,” in *2011 37th IEEE Photovoltaic Specialists Conference*, 2011, pp. 003654–003657.

[14] X. Wu, W. Liu, S. Cheng, Y. Lai, and H. Jia, “Photoelectric properties of Cu_2ZnSnS_4 thin films deposited by thermal evaporation,” *J. Semicond.*, vol. 33, no. 2, p. 22002, Feb. 2012.

[15] K. Jimbo *et al.*, “Cu2ZnSnS4-type thin film solar cells using abundant materials,” *Thin Solid Films*, vol. 515, no. 15, pp. 5997–5999, May 2007.

[16] A. Redinger, D. M. Berg, P. J. Dale, and S. Siebentritt, “The Consequences of Kesterite Equilibria for Efficient Solar Cells,” *J. Am. Chem. Soc.*, vol. 133, no. 10, pp. 3320–3323, Mar. 2011.

[17] V. Chawla and B. Clemens, “Effect of composition on high efficiency CZTSSe devices fabricated using co-sputtering of compound targets,” in *2012 38th IEEE Photovoltaic Specialists Conference*, 2012, pp. 002990–002992.

[18] W. Wang *et al.*, “Device Characteristics of CZTSSe Thin-Film Solar Cells with 12.6% Efficiency,” *Adv. Energy Mater.*, vol. 4, no. 7, p. 1301465, May 2014.

[19] H. Xin and H. W. Hillhouse, “8.3% Efficient copper zinc tin sulfoselenide solar cells processed from environmentally benign solvent,” in *2013 IEEE 39th Photovoltaic Specialists Conference (PVSC)*, 2013, pp. 0441–0443.

[20] H. Katagiri, N. Sasaguchi, S. Hando, S. Hoshino, J. Ohashi, and T. Yokota, “Preparation and evaluation of Cu2ZnSnS4 thin films by sulfurization of E?B evaporated precursors,” *Sol. Energy Mater. Sol. Cells*, vol. 49, no. 1–4, pp. 407–414, Dec. 1997.

[21] H. Katagiri *et al.*, “Development of CZTS-based thin film solar cells,” *Thin Solid Films*, vol. 517, no. 7, pp. 2455–2460, 2009.

[22] K. Wang *et al.*, “Thermally evaporated Cu2ZnSnS4 solar cells,” *Appl. Phys. Lett.*, vol. 97, no. 14, p. 143508, Oct. 2010.

[23] G. Altamura, “Development of CZTSSe thin films based solar cells ” Developpement de cellules solaires base de films minces $Cu_2ZnSn(S,Se)_4$,” 2014.

[24] G. Brammertz *et al.*, “Characterization of defects in 9.7% efficient $Cu_2ZnSnSe_4$-CdS-ZnO solar cells,” *Appl. Phys. Lett.*, vol. 103, no. 16, 2013.

[25] T. M. Friedlmeier, T. Wieser, T. Walter, H. Dittrich, and H.-D. Schock, “Heterojunctions based on Cu_2ZnSnS_4 and $Cu_2ZnSnSe_4$ thin films,” *Proc. 14th Eur. Photovolt. Sol. Energy Conf.*, pp. 1242–1245, 1997.

[26] G. Zoppi, I. Forbes, R. W. Miles, P. J. Dale, J. J. Scragg, and L. M. Peter, “$Cu_2ZnSnSe_4$ thin film solar cells produced by selenisation of magnetron sputtered precursors,” *Prog. Photovoltaics Res. Appl.*, vol. 17, no. 5, pp. 315–319, Aug. 2009.

[27] I. Repins *et al.*, “Co-evaporated $Cu_2ZnSnSe_4$ films and devices,” *Sol. Energy Mater. Sol. Cells*, vol. 101, pp. 154–159, Jun. 2012.

[28] S. Adachi, *Earth-abundant materials for solar cells : Cu_2-II-IV-VI_4 semiconductors*. .

[29] L. I. (Lev I. Berger, *Semiconductor materials*. CRC Press, 1997.

[30] S. Adachi, *Properties of semiconductor alloys : group-IV, III-V and II-VI semiconductors*. Wiley, 2009.

[31] S. Adachi, *Earth-Abundant Materials for Solar Cells*. Chichester, UK: John Wiley & Sons, Ltd, 2015.

[32] E. Parthé, K. Yvon, R. H. Deitch, and IUCr, “The crystal structure of Cu_2CdGeS_4 and other quaternary normal tetrahedral structure compounds,” *Acta Crystallogr. Sect. B Struct. Crystallogr. Cryst. Chem.*, vol. 25, no. 6, pp. 1164–1174, Jun. 1969.

[33] S. Chen, A. Walsh, Y. Luo, J.-H. Yang, X. G. Gong, and S.-H. Wei, “Wurtzite-derived polytypes of kesterite and stannite quaternary chalcogenide semiconductors,” *Phys. Rev. B*, vol. 82, no. 19, p. 195203, Nov. 2010.

[34] S. Schorr and G. Gonzalez-Aviles, “In-situ investigation of the structural phase transition in kesterite,” *Phys. status solidi*, vol. 206, no. 5, pp. 1054–1058, May 2009.

[35] W. G. Zeier *et al.*, “Bond strength dependent superionic phase transformation in the solid solution series $Cu_2ZnGeSe_{4-x}S_x$,” *J. Mater. Chem. A*, vol. 2, no. 6, pp. 1790–1794, Jan. 2014.

[36] Z.-Y. Xiao *et al.*, “Bandgap engineering of $Cu_2Cd_xZn_{1-x}SnS_4$ alloy for photovoltaic applications: A complementary experimental and first-principles study,” *J. Appl. Phys.*, vol. 114, no. 18, p. 183506, Nov. 2013.

[37] I. V Dudchak and L. V Piskach, “P hase equilibria in the Cu_2SnSe_3 –$SnSe_2$ – ZnSe system,” *J. Alloys Compd.*, vol. 351, pp. 145–150, 2003.

[38] A. Nagoya, R. Asahi, R. Wahl, and G. Kresse, “Defect formation and phase stability of Cu_2ZnSnS_4photovoltaic material,” *Phys. Rev. B*, vol. 81, no. 11, p. 113202, Mar. 2010.

[39] P. J. Dale, K. Hoenes, J. Scragg, and S. Siebentritt, “A review of the challenges facing kesterite based thin film solar cells,” in *2009 34th IEEE Photovoltaic Specialists Conference (PVSC)*, 2009, pp. 002080–002085.

[40] C. Persson, Y.-J. Zhao, S. Lany, and A. Zunger, “n -type doping of $CuInSe_2$ and $CuGaSe_2$,” *Phys. Rev. B*, vol. 72, no. 3, p. 35211, Jul. 2005.

[41] M. Bär *et al.*, “Impact of KCN etching on the chemical and electronic surface structure of Cu_2ZnSnS_4 thin-film solar cell absorbers,” *Appl. Phys. Lett.*, vol. 99, no. 15, p. 152111, Oct. 2011.

[42] A. Redinger *et al.*, “Route Toward High-Efficiency Single-Phase $Cu_2ZnSnSe_4$ Thin-Film Solar Cells: Model Experiments and Literature Review,” *IEEE J. Photovoltaics*, vol. 1, no. 2, pp. 200–206, Oct. 2011.

[43] A. Redinger *et al.*, “Detection of a ZnSe secondary phase in coevaporated $Cu_2ZnSnSe_4$ thin films,” *Appl. Phys. Lett.*, vol. 98, no. 10, p. 101907, Mar. 2011.

[44] S. Siebentritt and S. Schorr, “Kesterites-a challenging material for solar cells,” *Prog. Photovoltaics Res. Appl.*, vol. 20, no. 5, pp. 512–519, Aug. 2012.

[45] S. Chen *et al.*, “Compositional dependence of structural and electronic properties of C $Cu_2ZnSn(S,Se)_4$” *Phys. Rev. B*, vol. 83, no. 12, p. 125201, 2011.

[46] S. Chen, X. G. Gong, A. Walsh, and S.-H. Wei, “Electronic structure and stability of quaternary chalcogenide semiconductors derived from cation cross-substitution of II-VI and I-III-VI_2compounds,” *Phys. Rev. B*, vol. 79, no. 16, p. 165211, Apr. 2009.

[47] G. S. Babu, Y. B. K. Kumar, P. U. Bhaskar, and V. S. Raja, “Effect of post-deposition annealing on the growth of $Cu_2ZnSnSe_4$ thin films for a solar cell absorber layer,” *Semicond. Sci. Technol.*, vol. 23, no. 8, p. 85023, Aug. 2008.

[48] Y.-H. Li *et al.*, “Revised ab initio natural band offsets of all group IV, II-VI, and III-V semiconductors,” *Appl. Phys. Lett.*, vol. 94, no. 21, p. 212109, May 2009.

[49] S. Chen, L.-W. Wang, A. Walsh, X. G. Gong, and S.-H. Wei, “Abundance of $Cu_{Zn} + Sn_{Zn}$ and $2Cu_{Zn} + Sn_{Zn}$ defect clusters in kesterite solar cells,” *Appl. Phys. Lett.*, vol. 101, no. 22, p. 223901, Nov. 2012.

[50] A. (Antonio) Luque and S. Hegedus, *Handbook of photovoltaic science and*

engineering. Wiley, 2011.

[51] M. Kumar, A. Dubey, N. Adhikari, S. Venkatesan, and Q. Qiao, "Strategic review of secondary phases, defects and defect-complexes in kesterite CZTS–Se solar cells," *Energy Environ. Sci.*, vol. 8, no. 11, pp. 3134–3159, 2015.

[52] H. Katagiri, K. Saitoh, T. Washio, H. Shinohara, T. Kurumadani, and S. Miyajima, "Development of thin film solar cell based on Cu_2ZnSnS_4 thin films," *Sol. Energy Mater. Sol. Cells*, vol. 65, no. 1–4, pp. 141–148, Jan. 2001.

[53] T. Tanaka *et al.*, "Preparation of Cu_2ZnSnS_4 thin films by hybrid sputtering," *J. Phys. Chem. Solids*, vol. 66, no. 11, pp. 1978–1981, Nov. 2005.

[54] K. Biswas, S. Lany, and A. Zunger, "The electronic consequences of multivalent elements in inorganic solar absorbers: Multivalency of Sn in Cu_2ZnSnS_4," *Appl. Phys. Lett.*, vol. 96, no. 20, p. 201902, May 2010.

[55] S. Chen, A. Walsh, X.-G. Gong, and S.-H. Wei, "Classification of Lattice Defects in the Kesterite Cu_2ZnSnS_4 and $Cu_2ZnSnSe_4$ Earth-Abundant Solar Cell Absorbers," *Adv. Mater.*, vol. 25, no. 11, pp. 1522–1539, Mar. 2013.

[56] K. Tanaka, M. Oonuki, N. Moritake, and H. Uchiki, "Cu_2ZnSnS_4 thin film solar cells prepared by non-vacuum processing," 2009.

[57] P. Y. Yu and M. Cardona, *Fundamentals of Semiconductors*. Berlin, Heidelberg: Springer Berlin Heidelberg, 1996.

[58] W. Shockley, "The Theory of p-n Junctions in Semiconductors and p-n Junction Transistors," *Bell Syst. Tech. J.*, pp. 435–489, 1948.

[59] S. M. Sze and K. K. Ng, *Physics of Semiconductor Devices*, 3rd ed. Cham: Springer International Publishing, 2014.

[60] B. L. Sharma and R. K. Purohit, *Semiconductor heterojunctions,*. Pergamon Press, 1974.

[61] R. L. Anderson, “Experiments on Ge-GaAs heterojunctions,” *Solid. State. Electron.*, vol. 5, no. 5, pp. 341–351, Sep. 1962.

[62] K. Yilmaz, “INVESTIGATION OF InSe THIN FILM BASED DEVICES A THESIS SUBMITTED TO THE GRADUATE SCHOOL OF NATURAL AND APPLIED SCIENCE OF MIDDLE EAST TECHNICAL UNIVERSITY IN PARTIAL FULFILMENT OF THE REQUIREMENTS FOR THE DEGREE OF DOCTOR OF PHILOSOPHY IN PHYSICS,” 2004.

[63] “2. Principle of Solar Cell Operation & Physics - TU Delft OCW.” .

[64] A. L. Patterson, “The Scherrer Formula for X-Ray Particle Size Determination,” *Phys. Rev.*, vol. 56, no. 10, pp. 978–982, Nov. 1939.

[65] B. D. Cullity, *Elements of DIFFRACTION*. 1978.

[66] “Wide Angle X-ray Diffraction Studies of Liquid Crystals.” .

[67] L. L. Kazmerski, *Polycrystalline and amorphous thin films and devices*. Academic Press, 1980.

[68] H. H. Gullu, “MATERIAL AND DEVICE CHARACTERIZATION OF $ZnInSe_2$ AND $Cu_{0.5}Ag_{0.5}InSe_2$ THIN FILMS FOR PHOTOVOLTAIC APPLICATIONS,” Middle East Technical University, 2016.

[69] G. Turrell and J. Corset, *Raman Microscopy: Developments and Applications*. San Diego, California: Elsevier Academic Press, 1996.

[70] “Spectroscopy Facilities || The Prashant Kamat lab at the University of Notre Dame.” .

[71] “Scanning Electron Microscope [SubsTech].” .

[72] U. Maver, T. Velnar, M. Gaberščček, O. Planinšek, and M. Finšgar, “Recent progressive use of atomic force microscopy in biomedical applications,” *TrAC Trends Anal. Chem.*, vol. 80, pp. 96–111, Jun. 2016.

[73] M. G. Mellon, “Analytical experiments in spectrophotometry,” *J. Chem. Educ.*, vol. 19, no. 9, p. 415, Sep. 1942.

[74] “Hall Effect.” http://hyperphysics.phy-astr.gsu.edu/hbase/magnetic/Hall.html, .

[75] P. M. P. Salomé, P. A. Fernandes, J. P. Leitão, M. G. Sousa, J. P. Teixeira, and A. F. da Cunha, “Secondary crystalline phases identification in $Cu_2ZnSnSe_4$ thin films: contributions from Raman scattering and photoluminescence,” *J. Mater. Sci.*, vol. 49, no. 21, pp. 7425–7436, Nov. 2014.

[76] Ö. Bayraklı, M. Terlemezoglu, H. H. Güllü, and M. Parlak, “Investigation of precursor sequence and post-annealing effects on the properties of $Cu_2SnZnSe_4$ thin films deposited by the elemental thermal evaporation,” *Mater. Res. Express*, vol. 4, no. 8, p. 86411, Aug. 2017.

[77] M. Meng, L. Wan, P. Zou, S. Miao, and J. Xu, “Cu2ZnSnSe4 thin films prepared by selenization of one-step electrochemically deposited Cu–Zn–Sn–Se precursors,” *Appl. Surf. Sci.*, vol. 273, pp. 613–616, May 2013.

[78] P. A. Fernandes, P. M. P. Salomé, and A. F. da Cunha, “Growth and Raman scattering characterization of Cu2ZnSnS4 thin films,” *Thin Solid Films*, vol. 517, no. 7, pp. 2519–2523, Feb. 2009.

[79] K. R. Murali and M. Balasubramanian, “Properties of pulse plated ZnSe films,” vol. 431, no. 6, pp. 118–122, 2006.

[80] A. Slav, “OPTICAL CHARACTERIZATION OF TiO 2 -Ge NANOCOMPOSITE FILMS OBTAINED BY REACTIVE MAGNETRON SPUTTERING,” *J. Nanomater. Biostructures.*, vol. 6, no. 3, pp. 915–920, 2011.

[81] D. K. Schroder, *Semiconductor material and device characterization*. IEEE Press, 2006.

[82] A. Fairbrother *et al.*, “Secondary phase formation in Zn-rich $Cu_2ZnSnSe_4$ -based solar cells annealed in low pressure and temperature conditions,” *Prog.*

Photovoltaics Res. Appl., vol. 22, no. 4, pp. 479–487, Apr. 2014.

[83] P. Kevin, S. N. Malik, M. A. Malik, and P. O'Brien, "The aerosol assisted chemical vapour deposition of SnSe and Cu 2 SnSe 3 thin films from molecular precursors," *Chem. Commun.*, vol. 50, no. 92, pp. 14328–14330, 2014.

[84] S. Ranjbar, M. R. Rajesh Menon, P. A. Fernandes, and A. F. da Cunha, "Effect of selenization conditions on the growth and properties of $Cu_2ZnSn(S,Se)_4$ thin films," *Thin Solid Films*, vol. 582, pp. 188–192, May 2015.

[85] C. S. (Charles S. Barrett and T. B. Massalski, *Structure of metals : crystallographic methods, principles and data*. Pergamon, 1980.

[86] T. Tanaka *et al.*, "Existence and removal of Cu 2 Se second phase in coevaporated Cu 2 ZnSnSe 4 thin films," *J. Appl. Phys.*, vol. 111, no. 5, p. 53522, Mar. 2012.

[87] R. A. Wibowo, W. S. Kim, E. S. Lee, B. Munir, and K. H. Kim, "Single step preparation of quaternary thin films by RF magnetron sputtering from binary chalcogenide targets," *J. Phys. Chem. Solids*, vol. 68, no. 10, pp. 1908–1913, Oct. 2007.

[88] M. Li, M. Zheng, T. Zhou, C. Li, L. Ma, and W. Shen, "Fabrication and centeracterization of ordered $CuIn_{(1-x)}GaxSe_2$ nanopore films via template-based electrodeposition," *Nanoscale Res. Lett.*, vol. 7, no. 1, p. 675, 2012.

[89] T. Tanaka *et al.*, "Existence and removal of Cu_2Se second phase in coevaporated $Cu_2ZnSnSe_4$ thin films," *J. Appl. Phys.*, vol. 111, no. 5, p. 53522, Mar. 2012.

[90] D. Park *et al.*, "Optical characterization of $Cu_2ZnSnSe_4$ grown by thermal co-evaporation," *Thin Solid Films*, vol. 519, no. 21, pp. 7386–7389, Aug. 2011.

[91] M. Grossberg, J. Krustok, J. Raudoja, K. Timmo, M. Altosaar, and T. Raadik, "Photoluminescence and Raman study of $Cu_2ZnSn(Se_xS_{1-x})_4$ monograins for

photovoltaic applications," *Thin Solid Films*, vol. 519, no. 21, pp. 7403–7406, Aug. 2011.

[92] M. Altosaar *et al.*, "$Cu_2Zn_{1-x}Cd_xSn(Se_{1-y}S_y)_4$ solid solutions as absorber materials for solar cells," *Phys. status solidi*, vol. 205, no. 1, pp. 167–170, Jan. 2008.

[93] T. K. Todorov, K. B. Reuter, and D. B. Mitzi, "High-Efficiency Solar Cell with Earth-Abundant Liquid-Processed Absorber," *Adv. Mater.*, vol. 22, no. 20, pp. E156–E159, May 2010.

[94] S. Ahn *et al.*, "Determination of band gap energy (Eg) of $Cu_2ZnSnSe_4$ thin films: On the discrepancies of reported band gap values," *Appl. Phys. Lett.*, vol. 97, no. 2, p. 21905, Jul. 2010.

[95] G. Suresh Babu, Y. B. Kishore Kumar, P. Uday Bhaskar, and S. Raja Vanjari, "Effect of Cu/(Zn+Sn) ratio on the properties of co-evaporated $Cu_2ZnSnSe_4$ thin films," *Sol. Energy Mater. Sol. Cells*, vol. 94, no. 2, pp. 221–226, Feb. 2010.

[96] C. Persson, "Electronic and optical properties of Cu_2ZnSnS_4 and $Cu_2ZnSnSe_4$," *J. Appl. Phys.*, vol. 107, no. 5, p. 53710, Mar. 2010.

[97] S. Chen, X. G. Gong, A. Walsh, and S.-H. Wei, "Crystal and electronic band structure of Cu_2ZnSnX_4 (X=S and Se) photovoltaic absorbers: First-principles insights," *Appl. Phys. Lett.*, vol. 94, no. 4, p. 41903, Jan. 2009.

[98] H. Matsushita, T. Maeda, A. Katsui, and T. Takizawa, "Thermal analysis and synthesis from the melts of Cu-based quaternary compounds Cu–III–IV–VI_4 and Cu_2–II–IV–VI_4 (II=Zn,Cd; III=Ga,In; IV=Ge,Sn; VI=Se)," *J. Cryst. Growth*, vol. 208, no. 1–4, pp. 416–422, Jan. 2000.

[99] H. . Pathan, J. . Desai, and C. . Lokhande, "Modified chemical deposition and physico-chemical properties of copper sulphide (Cu_2S) thin films," *Appl. Surf. Sci.*, vol. 202, no. 1–2, pp. 47–56, Dec. 2002.

[100] Y. Z. Li, X. D. Gao, C. Yang, and F. Q. Huang, “The effects of sputtering power on optical and electrical properties of copper selenide thin films deposited by magnetron sputtering,” *J. Alloys Compd.*, vol. 505, no. 2, pp. 623–627, Sep. 2010.

[101] H. Morikawa, “Planar Defects of Cu_3Se_2 Crystals Produced by Solid-State Reaction,” *Jpn. J. Appl. Phys.*, vol. 11, no. 4, pp. 431–436, Apr. 1972.

[102] Y.-J. Lin, C.-H. Ruan, Y.-J. Chu, C.-J. Liu, and F.-H. Lin, “Correlation between interface modification and rectifying behavior of p-type Cu_2ZnSnS_4/n-type Si diodes,” *Appl. Phys. A*, vol. 121, no. 1, pp. 103–108, Oct. 2015.

[103] C.-H. Ruan, Y.-J. Lin, Y.-H. Chen, and H.-C. Chang, “Rectifying performance of p-type tin(II) sulfide contacts on n-type silicon: Effect of silicon nanowire sulfidation on electronic transport of heterojunction diodes,” *Mater. Sci. Semicond. Process.*, vol. 32, pp. 62–67, Apr. 2015.

[104] R. Jansen and J. S. Moodera, “Electrical and photoelectrical properties of Si/In–Te heterojunctions,” *Appl. Phys. Lett.*, vol. 75, no. 14, pp. 2100–2102, Oct. 1999.

[105] F. A. Akgul, G. Akgul, H. H. Gullu, H. E. Unalan, and R. Turan, “Enhanced diode performance in cadmium telluride–silicon nanowire heterostructures,” *J. Alloys Compd.*, vol. 644, pp. 131–139, Sep. 2015.

[106] B. Shin, O. Gunawan, Y. Zhu, N. A. Bojarczuk, S. J. Chey, and S. Guha, “Thin film solar cell with 8.4% power conversion efficiency using an earth-abundant Cu_2ZnSnS_4 absorber,” *Prog. Photovoltaics Res. Appl.*, vol. 21, no. 1, pp. 72–76, Jan. 2013.

[107] V. K. Jain and A. Verma, Eds., *Physics of Semiconductor Devices*. Cham: Springer International Publishing, 2014.

[108] K. Tanaka, M. Oonuki, N. Moritake, and H. Uchiki, “Cu_2ZnSnS_4 thin film solar cells prepared by non-vacuum processing,” *Sol. Energy Mater. Sol. Cells*, vol.

93, no. 5, pp. 583–587, May 2009.

[109] B.-A. Schubert *et al.*, "Cu_2ZnSnS_4 hin film solar cells by fast coevaporation," *Prog. Photovoltaics Res. Appl.*, vol. 19, no. 1, pp. 93–96, Jan. 2011.

[110] I. D. Olekseyuk, L. D. Gulay, I. V. Dydchak, L. V. Piskach, O. V. Parasyuk, and O. V. Marchuk, "Single crystal preparation and crystal structure of the Cu2Zn/Cd,Hg/SnSe4 compounds," *J. Alloys Compd.*, vol. 340, no. 1–2, pp. 141–145, Jun. 2002.

[111] S. M. Lee and Y. S. Cho, "Characteristics of $Cu_2ZnSnSe_4$ and $Cu_2ZnSn(Se,S)_4$ absorber thin films prepared by post selenization and sequential sulfurization of co-evaporated Cu–Zn–Sn precursors," *J. Alloys Compd.*, vol. 579, pp. 279–283, Dec. 2013.

[112] F. Yakuphanoglu, "Nanostructure Cu_2ZnSnS_4 thin film prepared by sol–gel for optoelectronic applications," *Sol. Energy*, vol. 85, no. 10, pp. 2518–2523, Oct. 2011.

[113] A. Ennaoui *et al.*, "Cu_2ZnSnS_4 thin film solar cells from electroplated precursors: Novel low-cost perspective," *Thin Solid Films*, vol. 517, no. 7, pp. 2511–2514, Feb. 2009.

[114] J. Y. Kim *et al.*, "Efficient Tandem Polymer Solar Cells Fabricated by All-Solution Processing," *Science (80-.).*, vol. 317, no. 5835, pp. 222–225, Jul. 2007.

[115] A. V. Moholkar *et al.*, "Studies of compositional dependent CZTS thin film solar cells by pulsed laser deposition technique: An attempt to improve the efficiency," *J. Alloys Compd.*, vol. 544, pp. 145–151, Dec. 2012.

[116] F. Khan, S. N. Singh, and M. Husain, "Effect of illumination intensity on cell parameters of a silicon solar cell," *Sol. Energy Mater. Sol. Cells*, vol. 94, no. 9, pp. 1473–1476, Sep. 2010.

[117] B. C. Chakravarty, N. K. Arora, S. N. Singh, and B. K. Das, “Solar cell performance with an inhomogenous grain size distribution,” *IEEE Trans. Electron Devices*, vol. 33, no. 1, pp. 158–160, Jan. 1986.

[118] D. V. Lang, “Deep-level transient spectroscopy: A new method to characterize traps in semiconductors,” *J. Appl. Phys.*, vol. 45, no. 7, pp. 3023–3032, Jul. 1974.

[119] E. Cuce, P. M. Cuce, and T. Bali, “An experimental analysis of illumination intensity and temperature dependency of photovoltaic cell parameters,” *Appl. Energy*, vol. 111, pp. 374–382, Nov. 2013.

[120] S. N. Singh and D. Kumar, “Phenomenological model of anomalously high photovoltages generated in obliquely deposited semiconductor films,” *J. Appl. Phys.*, vol. 103, no. 2, p. 23713, Jan. 2008.

[121] N. Song *et al.*, “Epitaxial Cu_2ZnSnS_4 thin film on Si (111) 4° substrate,” *Appl. Phys. Lett.*, vol. 106, no. 25, p. 252102, Jun. 2015.

[122] E. Veena, bullet Kasturi, V. Bangera, and bullet G K Shivakumar, “Effect of annealing on the properties of spray-pyrolysed lead sulphide thin films for solar cell application,” *Appl. Phys. A*, vol. 123.

[123] M. Terlemezoglu, Ö. Bayraklı, H. H. Güllü, T. Çolakoğlu, D. E. Yildiz, and M. Parlak, “Analysis of current conduction mechanism in CZTSSe/n-Si structure,” *J. Mater. Sci. Mater. Electron.*, 2018.

[124] X. Zhang *et al.*, “ZnSe nanowire/Si p–n heterojunctions: device construction and optoelectronic applications,” *Nanotechnology*, vol. 24, no. 39, p. 395201, Oct. 2013.

[125] K. Sumino, *Defect Control in Semiconductors*. Elsevier, 1990.

[126] M. Yang, T. P. Chen, L. Ding, Y. Liu, F. R. Zhu, and S. Fung, “Capacitance switching in SiO_2 thin film embedded with Ge nanocrystals caused by

ultraviolet illumination," *Appl. Phys. Lett.*, vol. 95, no. 9, p. 91111, Aug. 2009.

[127] S. A. Arzhannikova *et al.*, "Photoinduced Variation of Capacitance Characteristics of MDS Structures with Three-Layer SiNx Dielectrics," *Solid State Phenom.*, vol. 131–133, pp. 461–466, 2008.

[128] S. Rondiya *et al.*, "CZTS/CdS: interface properties and band alignment study towards photovoltaic applications," *J. Mater. Sci. Mater. Electron.*, vol. 0, no. 0, pp. 1–10, 2017.

[129] D. Ho Yeon, B. Chandra Mohanty, S. M. Lee, and Y. Soo Cho, "Effect of band-aligned double absorber layers on photovoltaic characteristics of chemical bath deposited PbS/CdS thin film solar cells," *Sci. Rep.*, vol. 5, no. 1, p. 14353, Nov. 2015.

[130] M. E. Erkan, V. Chawla, and M. A. Scarpulla, "Reduced defect density at the CZTSSe/CdS interface by atomic layer deposition of Al_2O_3," *J. Appl. Phys.*, vol. 119, no. 19, p. 194504, May 2016.

[131] X. Song, X. Ji, M. Li, W. Lin, X. Luo, and H. Zhang, "A review on development prospect of CZTS based thin film solar cells," *Int. J. Photoenergy*, vol. 2014, 2014.

[132] H. Sai *et al.*, "Effect of Front TCO Layer on Properties of Substrate-Type Thin-Film Microcrystalline Silicon Solar Cells," *IEEE J. Photovoltaics*, vol. 5, no. 6, pp. 1528–1533, 2015.

CURRICULUM VITAE

PERSONAL INFORMATION

Surname, Name: Bayraklı, Özge
Nationality: Turkish (TC)
Date and Place of Birth: 12 August 1986, Ankara
Marital Status: Single
Phone: +90 312 210 7647
Fax: +90 312 210 5099
e-mail: bayrakli@metu.edu.tr

EDUCATION

Degree	Institution	Year of Degree
BS	Gazi University, Physics Education	2009 (with first rank)
High School	Mustafa Kemal Super High School	2004 (with first rank)

WORK EXPERIENCE

Year	Place	Enrollment
2010-Present	METU,Physics Department	Research Assistant
2009-2010	Ahi Evran University, Physics Department	Research Assistant

FOREIGN LANGUAGES

Advanced English

PUBLICATIONS

A. ARTICLES

A1. Güllü H H, Terlemezoğlu M., **Bayrakli Ö**, Yildiz D. E., Parlak M., "Investigation of Carrier Transport Mechanisms in the Cu-Zn-Se based Heterostructure Grown by Sputtering Technique" Canadian Journal of Physics, (in proof), 2018.
Doi: 10.1139/cjp-2017-0777

A2. Yiğiterol F.; Güllü H. H.; **Bayraklı Ö.**, Yildiz D. E., "Temperature Dependent Electrical Characteristics of Au/Si3N4/4H n-SiC MIS Diode", Journal of Electronic Materials, (accepted),2018.

A3. Terlemezoğlu M., **Bayrakli Ö.**, Güllü H H, Çolakoğlu T, Yildiz D. E., Parlak M., "Analysis of current conduction mechanism in CZTSSe/n-Si structure" Journal of Materials Science: Materials in Electronics, accepted, 2018.
Doi: 10.1007/s10854-017-8490-1

A4. Güllü H H, **Bayrakli Ö.**, Yildiz D. E., Parlak M., "Study on the electrical properties of ZnSe/Si heterojunction diode." Journal of Materials Science: Materials in Electronics, 28(23), 17806-17815., 2017.
Doi: 10.1007/s10854-017-7721-9

A5. Sürücü G., Güllü H. H., **Bayrakli Ö.**, Parlak M., "Enhancement in Photovoltaic Characteristics of CdS/CdTe Heterojunction." Journal of Polytechnic, 20, 801-805, 2017.
Doi: 10.2339/politeknik.368993

A6. Güllü H. H., **Bayrakli Ö.**, Parlak M., "Optical and electrical characteristics of thermally evaporated $Cu_{0.5}Ag_{0.5}InSe_2$ thin films.", Thin Solid Films, 639, 29-35, 2017.
Doi: 10.1016/j.tsf.2017.08.024

A7. Bayrakli Ö., Güllü H. H., Parlak M., "Investigation on Device Characteristics of n-Cds/p-Ag(Ga-In)Te Heterojunction Diode.", Surface Review and Letters, 25, 1850107, 2017.
Doi: 10.1142/S0218625X1850107X

A8. Bayrakli Ö., Terlemezoğlu M., Güllü H. H., Parlak M., "Investigation of precursor sequence and post-annealing effects on the properties of $Cu_2SnZnSe_4$ thin films deposited by the elemental thermal evaporation." Materials Research Express, 4(8), 86411, 2017.
Doi: 10.1088/2053-1591/aa852d

A9. Bayrakli Ö., Terlemezoğlu M., Güllü H. H., Parlak M., "Deposition of CZTSe thin films and illumination effects on the device properties of Ag/n-Si/p-CZTSe/In heterostructure.", Journal of Alloys and Compounds, 709, 337-343, 2017.
Doi: 10.1016/j.jallcom.2017.03.163

A10. Kiliç B., Türkdoğan S., Ozer O. C., Asgin M., **Bayrakli Ö.**, Sürücü G., Astam A., Ekinci D., "Produce of graphene iron pyrite FeS_2 thin films counter electrode for dye sensitized solar cell." Materials Letters, 185, 584-587, 2016.
Doi: 10.1016/j.matlet.2016.06.069

A11. Coşkun E., Güllü H. H., Candan İ., **Bayrakli Ö.**, Parlak M., Erçelebi A. Ç., "Device behavior of an In/p-$AgGaInTe_2$/n-Si/Ag heterojunction diode.", Materials Science in Semiconductor Processing, 34, 138-145, 2015.
Doi: 10.1016/j.mssp.2015.02.043

A12. Güllü H. H., **Bayrakli Ö.**, Candan İ., Coşkun E., Parlak M., "Structural and optical properties of Zn-In-Te thin films deposited by thermal evaporation technique.", Journal of Alloys and Compounds, 566, 83-89, 2013.
Doi: 10.1016/j.jallcom.2013.03.030

B. ORAL PRESENTATIONS

B1. Güllü H. H., Terlemezoğlu M., **Bayrakli Ö.**, Yildiz D. E., Parlak M., "Investigation of carrier transport mechanisms in the $CuZnSe_2$-based heterostructure grown by sputtering technique.", Turkish Physical Society 33rd International Physics Congress, 2017.

B2. Yildiz D. E., Güllü H. H., **Bayrakli Ö.**, Parlak M., "Dielectric properties of electron beam evaporated ZnSe/Si heterostructures in the wide frequency range.", International Symposium on Multidisciplinary Studies, 2017.

B3. Yildiz D. E., Güllü H. H., **Bayrakli Ö.**, "Frequency and voltage dependent electrical properties of structure Au-Cu/ZnO/p-Si (MOS) structures.", International Symposium on Multidisciplinary Studies, 2017.

B4. Sürücü G., **Bayrakli Ö.**, Güllü H. H., Terlemezoğlu M., Parlak M., "Device Behavior of CZTSe/Si Nanowire Heterojunction.", Photovoltaic Technical Conference, 2017.

B5. Bayrakli Ö., Güllü H. H., Terlemezoğlu M., Parlak M., "Optimization of the Fabrication Process for Al-doped ZnO Thin Films on Soda Lime Glass Substrates by Thermal Heating.", 2017 ICG Annual Meeting and 32nd Şişecam Glass Symposium, 2017.

B6. Terlemezoğlu M., **Bayrakli Ö.**, Güllü H. H., Yildiz D. E., Parlak M., "The electrical properties of p-CZTSSe/n-Si heterostructure.", International Conference on Condensed Matter and Materials Science, 2017.

B7. Bayrakli Ö., Terlemezoğlu M., Güllü H. H., Yildiz D. E., Sürücü G., Parlak M., "Deposition of CZTSe thin films and investigation of their devices properties.", International Conference on Condensed Matter and Materials Science, 2017.

B8. Bayrakli Ö., Güllü H. H., Parlak M., "Investigation of the device properties of CZTSe thin films for Solar Cells.", 2nd International Congress on the World of Technology and Advanced Materials, 2016.

B9. Sürücü G., **Bayrakli Ö.**, Özen Y., Kinaci B., "Deposition of Boron Doped Graphene for CdTe Solar Cell Applications.", 2nd International Congress on the World of Technology and Advanced Materials, 2016.

B10. Hosseini A., Güllü H. H., **Bayrakli Ö.**, Parlak M., Turan R., Erçelebi A. Ç., "Fabrication and Investigation of Extremely Thin CdTe Absorber Layer Solar Cells.", 2nd International Congress on the World of Technology and Advanced Materials, 2016.

B11. Bayrakli Ö., Güllü H. H., Parlak M., "Device Measurement and Analysis of Ag Ga In Te Based Thin Film Heterojunction Diode.", Solar TR-3, 2015.

B12. Bayrakli Ö., Güllü H. H., Coşkun E., Candan İ., Parlak M., "Characterization of Ag Ga In Te Thin Films for Solar Cell.", Science and Applications of Thin Films Conference and Exhibition (SATF2014) , 2014.

C. POSTER PRESENTATIONS

C1. Bayrakli Ö., Terlemezoğlu M., Güllü H. H., Yildiz D. E., Çolakoğlu T., Coşkun E., Parlak M., "Determination of the Interface Properties of p-CZTSe/n-Si Nanowire Heterojunction Diode." Materials Research Society (MRS) 2017 Fall Meeting, 2017.

C2. Güllü H. H., **Bayrakli Ö.,** Yildiz D. E., Parlak M., "Influence of the Heat Treatment on the Material Properties of Self-Aligned Planar Cu-Ag-In-Sn Nanowires.", International Conference on Condensed Matter and Materials Science, 2017.

C3. Coşkun E., Güllü H. H., **Bayrakli Ö.**, Terlemezoğlu M., Parlak M., "Synthesis and Structural Characterization on the (Cu,Ag)GaTe2 Thin Films Deposited on Si Nanowires.", European Materials Research Society-Spring Meeting 2017, 2017.

C4. Bayrakli Ö., Güllü H. H., Sürücü G., Terlemezoğlu M., Parlak M., "Theoretical and Experimental Invesitgation of Nano-mechanical Characteristics of SnTe Thin Films.", European Materials Research Society-Spring Meeting 2017, 2017.

C5. Güllü H. H., Terlemezoğlu M., **Bayrakli Ö.,** Parlak M., "The Effects of Substrate and Annealing Temperatures on Surface Morphology of Sputtered SnSe Thin Films.", European Materials Research Society-Spring Meeting 2017, 2017.

C6. Terlemezoğlu M., **Bayrakli Ö.,** Güllü H. H., Çolakoğlu T., Parlak M., "Physical properties and device application of CZTSSe thin films deposited by thermal evaporation method.", European Materials Research Society-Spring Meeting 2017, 2017.

C7. Güllü H. H., **Bayrakli Ö.,** Emir C., Terlemezoğlu M., Parlak M., "Influence of Chemical Post-deposition Treatment on the Structural Properties of ZnSnTe2 Thin Films.", European Materials Research Society-Spring Meeting 2017, 2017.

C8. Doğru Ç., **Bayrakli Ö.,** Terlemezoğlu M., Parlak M., "The Effect of CdCl2 Treatment on CdZnTe Thin Films.", European Materials Research Society-Spring Meeting 2017, 2017.

C9. Bayrakli Ö., Terlemezoğlu M., Güllü H. H., Sürücü G., Parlak M., "Deposition and characterization of ZTSeS thin films for photovoltaic applications.", Photovoltaic Technical Conference, 2017.

C10. Güllü H. H., Bayrakli Ö., Parlak M., "Electrical Characterization of Cu0 5Ag0 5InSe2 Thin Films.", 2nd International Congress on the World of Technology and Advanced Materials, 2016.

C11. Bayrakli Ö., Emir C., Güllü H. H., Parlak M., "Effects of Substrate Temperature on Material Characteristics of Sputtered Aluminum doped ZnO Thin Films.", SATF 2016, 2016.

C12. Güllü H. H., Coşkun E., Bayrakli Ö., Parlak M., "Design and Device Application of Si Based Cu Ag Ga Te Thin Film Heterojunction.", SATF 2016, 2016.

C13. Terlemezoğlu M., Güllü H. H., Bayrakli Ö., Parlak M., "Effect of Zn Doping on CdS Thin Film Deposited by RF Magnetron Sputtering.", EU PVSEC 2016, 2016.

C14. Güllü H. H., Bayrakli Ö., Coşkun E., Parlak M., "Fabrication and Characterization of p CuInSe2 n Si Heterojunction Diodes.", EU PVSEC 2016, 2016.

C15. Bayrakli Ö., Güllü H. H., Terlemezoğlu M., Parlak M., "Characterization of CZTSe Thin Films for Solar Cell.", EU PVSEC 2016, 2016.

C16. Güllü H. H., Coşkun E., Bayrakli Ö., Parlak M., "Optical Behavior of Sequential Thermal Evaporated ZnInSe2 Thin Films.", E-MRS 2016 Spring Meeting, 2016.

C17. Bayrakli Ö., Güllü H. H., Parlak M., "The effect of different annealing procedures on CZTSe thin film properties.", E-MRS 2016 Spring Meeting, 2016

C18. Güllü H. H., Bayrakli Ö., Coşkun E., Parlak M., "Studies on Device Properties of n ZnSe p Si Heterojunction Diode.", E-MRS 2016 Spring Meeting, 2016.

C19. Bayrakli Ö., Güllü H. H., Coşkun E., Parlak M., "Device Characterization of Zn Sn Se ZTSe Thin Films for Solar Cells.", E-MRS 2016 Spring Meeting, 2016

C20. Coşkun E., Çolakoğlu T., Güllü H. H., Bayrakli Ö., Parlak M., "Effect of nanowire length on device performance of n In2Se3 p Si nanowire heterojunctions.", E-MRS 2016 Spring Meeting, 2016.

C21. Güllü H. H., Bayrakli Ö., Candan İ., Parlak M., "Formation of ZnSnSe2 Thin Films Deposited by Using Sintered Stoichometric Powder.", MRS 2016 Spring Meeting and Exhibit, 2016.

C22. Güllü H. H., Bayrakli Ö., Parlak M., "Synthesis and characterization of CuZnSe2 thin film structures.", 17th International Conference on II-VI Compounds and Related Materials, 2015.

C23. Güllü H. H., Coşkun E., Bayrakli Ö., Parlak M., Erçelebi A. Ç., "Investigation of Electrical Properties of Cu Ag In Se Thin Films Deposited by Thermal Evaporation Method.", EU PVSEC 2015, 2015.

C24. Güllü H. H., Bayrakli Ö., Parlak M., "Structural Characterization and Optical Properties of AgInSe2 Thin Films.", 11th Nanoscience and Nanotechnology Conference, 2015.

C25. Güllü H. H., Bayrakli Ö., Parlak M., Erçelebi A. Ç., "Preparation and Characterization of CuZnSe2 Thin Films Deposited by Physically Vapor Deposition Technique.", Solar Tr3, 2015.

C26. Bayrakli Ö., Güllü H. H., Parlak M., "p AgGaxIn 1 x Te2 n ZnInSe2 Heterojunction for Solar Cell Applications.", MRS Spring Meeting 2015 & Exhibit, 2015.

C27. Güllü H. H., Coşkun E., Bayrakli Ö., Parlak M., "Material and Device Characterization of Cu0 5Ag0 5InSe2 and ZnInSe2 Thin Films for Photovoltaic Applications.", 2015 MRS Spring Meeting & Exhibit, 2015.

C28. Güllü H. H., Coşkun E., Bayrakli Ö., Candan İ., Parlak M., "Characterization of Sputtered Cu Zn Sn Te Thin Films for Device Applications.", E-MRS Spring Meeting 2014, 2014.

C29. Candan İ., Güllü H. H., Bayrakli Ö., Parlak M., Erçelebi A. Ç., "Growth and optimization of ZIT thin films for photovoltaic applications.", 9th Nanoscience and Nanotechnology Conference, (2013).

C30. Güllü H. H., Candan İ., Bayrakli Ö., Erçelebi A. Ç., Parlak M., "Investigation of the physical properties of CuInZnSe Thin Films Deposited by Sputtering.", E-MRS Spring Meeting 2013, 2013.

C33. Candan İ., Güllü H. H., Bayrakli Ö., Parlak M., Erçelebi A. Ç., "Growth and characterization of Ga rich $CuIn_{1-x}Ga_xSe_2$ CIGS thin films by sputtering technique for photovoltaic application.", E-MRS Spring Meeting 2013, 2013.

C31. Candan İ., Güllü H. H., Bayrakli Ö., Parlak M., Erçelebi A. Ç., "Effect of In Ga Ratio on The Properties of Semiconductor $CuIn_{1-x}Ga_xSe_2$ CIGS Thin Films.", SolarTR-2, 2012.

C32. Terlemezoğlu M., Bayrakli Ö., Güllü H. H., Yildiz D. E., Parlak M., "Fiziksel Buharlaştırma Tekniği ile Üretilen $Cu_2ZnSn(S,Se)_4$ İnce Filmlerinin Karakterizasyonu ve Aygıt Özelliklerinin İncelenmesi.", "23. Yoğun Madde Fiziği Ankara Toplantısı, 2017.

C33. Bayrakli Ö., Güllü H. H., Parlak M., "$AgGa_xIn_{1-x}Te_2$ İnce Filmlerin Üretilmesi ve Aygıt Özelliklerinin Belirlenmesi.", YMF21, 2015.

C34. Güllü H. H., Bayrakli Ö., Parlak M., "Saçtırma Yöntemiyle Üretilen Ag Zengin $AgInSe_2$ İnce Filmlerinin Özellikleri.", YMF21, 2015.

C35. Emir C., Güllü H. H., Bayrakli Ö., Parlak M., "Saçtırma Yöntemi ile Üretilen ITO İnce Filmlerinin Farklı Alttaş ve Tavlama Sıcaklıklarına göre İncelenmesi.", YMF21, 2015.

C36. Güllü H. H., Bayrakli Ö., Coşkun E., Parlak M., Erçelebi A. Ç., "$CuZnSe_2$ İnce FilmlerininSaçtırmalı Kaplama Tekniğiyle Üretilmesi ve Özelliklerinin Belirlenmesi.", Yoğun Madde Fiziği20, 2014.

C37. Güllü H. H., Candan İ., Bayrakli Ö., Parlak M., "Cu-Zn-Sn-Te İnce Filmlerin Yapısal ve OptikÖzelliklerinin İncelenmesi.", Yoğun Madde Fiziği 19, 2013.

C38. Bayrakli Ö., Demirtaş M., Güllü H. H., Candan İ., Parlak M., "Elektron Demeti Tekniğiyle Büyütülen $AgGa_xIn_{1-x}Te_2$ İnce Filmlerin Yapısal Optik ve Elektriksel Karakterizasyonu." Yoğun Madde Fiziği 18, 2011.

D. PROJECT WORK

D1. "$Cu_2ZnSn(S,Se)_4$ İnce Filmlerinin Fiziksel Buharlaştırma Tekniği ile Üretilmesi ve Özelliklerinin Belirlenmesi"BAP, Researcher, 01/01/2017 - 31/12/2017, (National).

D2. "$Cu_2ZnSnSe_4$ İnce Filmlerinin Fiziksel Buharlaştırma Tekniği ile Üretilmesi ve Özelliklerinin Belirlenmesi", BAP, Researcher, 01/01/2016 - 31/12/2016 (National).

D3. "$ZnSnS_2$ ince filmlerinin Isısal buharlaştırma tekniği ile üretilmesi ve özelliklerinin belirlenmesi", BAP, Researcher, 01/01/2015 - 31/12/2015 (National)**.**

D4. "CuSn(SSe yada Te_2) ve $CuZn(SeS)_2$ ince filmlerinin Isıl buharlaştırma ve saçtırmalı kaplama teknigiyle üretilmesi ve özelliklerinin belirlenmesi", BAP, Researcher, 01/01/2014 - 31/12/2014 (National).

D5. "$CuZnSnTe_2$ ince filmlerinin manyetik saçtırmalı kaplama tekniğiyle üretilmesi ve özelliklerinin belirlenmesi", BAP, Researcher, 01/01/2013 - 31/12/2013 (National).

D6. "$Zn_x ln_{1-X} Te_2$ İnce Filmlerinin Üretilmesi Ve Aygıt Özelliklerinin Belirlenmesi", BAP, Researcher, 01/01/2012 - 31/12/2012 (National).